NASA
Technical
Paper
2932

August 1989

15

Steady-State and Transitional Aerodynamic Characteristics of a Wing in Simulated Heavy Rain

Bryan A. Campbell
and Gaudy M. Bezos

NASA

NASA Technical Paper 2932

1989

Steady-State and Transitional Aerodynamic Characteristics of a Wing in Simulated Heavy Rain

Bryan A. Campbell
and Gaudy M. Bezos
Langley Research Center
Hampton, Virginia

National Aeronautics and Space Administration
Office of Management
Scientific and Technical Information Division

Summary

An investigation was conducted to determine the steady-state and transitional effects of simulated heavy rain on the subsonic aerodynamic characteristics of a wing model with a 1.29-ft chord, a 6.10 aspect ratio, and an NACA 23015 airfoil section. The wing was attached to a simple fuselage without an empennage section. Data were obtained at dynamic pressures of 10, 30, and 50 psf (i.e., at Reynolds numbers of 0.76×10^6, 1.31×10^6, and 1.69×10^6) in the Langley 14- by 22-Foot Subsonic Tunnel. Test variables including liquid water content, tunnel dynamic pressure, angle of attack, and trailing-edge flap angle were parametrically varied to study the aerodynamic trends associated with flying in a simulated rain environment.

In general, reductions in lift and increases in drag were observed in the simulated rain environment. The largest performance loss observed in this study was a 27-percent loss in lift and a 39-percent increase in drag on a high-lift configuration operating near maximum lift. The impact of heavy rain was greatest at the highest values of liquid water content, at angles of attack near maximum lift, and at the largest flap deflection. Under heavy rain conditions, the angle of attack at maximum lift was lower than that observed for the dry wing. The transient aerodynamic performance of this wing during transition from dry to wet steady-state conditions varied between a linear and a nonlinear transition.

Introduction

Much attention has been given in recent years to experiments aimed at understanding low-altitude wind shears and their effects on the takeoff and landing performance of airplanes (refs. 1 and 2). These investigations have resulted in the development of early warning devices and have led to operating procedures for avoiding an encounter with wind shears. Since wind shear may be accompanied by intense, heavy rains, additional investigative efforts have focused on the potential influences of rain-induced performance degradation. Reference 2 suggests that the aerodynamic performance penalties caused by wind shear coupled with those of heavy rain may have been a factor in several wind shear accidents. Analytical and experimental studies to determine the influence of heavy rain on airplane aerodynamic performance are presently underway at the Langley Research Center.

The analytical work of Haines and Luers (ref. 3) was an early attempt to estimate the performance penalties associated with heavy rain. Their studies utilized the experimentally known results of a surface artificially roughened by sand grains to simulate the unknown characteristics of surface irregularities caused by water-air boundary-layer interaction and water droplet impacts. The analysis indicated that significant lift and drag penalties may occur. Experimental results depicting the characteristics of the surface water film are presented by Hastings and Manuel in reference 4. Wind tunnel results for wings having an NACA 64-210 airfoil section are presented in references 5 and 6. General overviews of the research on heavy rain effects, including wind tunnel results for an NACA 0012 airfoil, are presented in references 7 and 8. In addition to the above-mentioned airfoils, reference 9 reports on the influence of heavy rain on the Wortmann FX67-K170 airfoil. The small-scale experimental tests of references 4 to 9 confirm the predicted performance degradation associated with simulated rain in the wind tunnel environment. The results predominantly show considerable reductions in maximum lift and stall angle accompanied by increases in overall drag. Tests are currently underway at the Langley Aircraft Landing Dynamics Facility (ALDF) to evaluate the influence of heavy rain on large-scale wing sections (refs. 10 and 11).

The present investigation was conducted in the Langley 14- by 22-Foot Subsonic Tunnel to study the steady-state and transitional aerodynamics of a wing entering heavy rain. A wing with an aspect ratio of 6.10, an NACA 23015 airfoil, and a plain, full-span flap was used to study the influence of liquid water content, angle of attack, Reynolds number, and flap angle on the wing aerodynamics. This investigation differed from previous related tests (refs. 4 to 9) in several respects. Since the effects of rain on the aerodynamic performance of wings do not scale linearly, establishing a data base of the small-scale steady-state trends is essential for developing the appropriate scaling relationships. Therefore, this study sought to identify a parametric data set on a wing with a plain flap which would eliminate the complex water-slot interactions which may be associated with a sophisticated slat–slotted-flap high-lift system. Additionally, this study sought to define the transitional (i.e., dry-wing to wet-wing) aerodynamic performance trends as the wing entered the simulated heavy-rain environment in the wind tunnel. These trends are helpful in understanding the performance dynamics and the corresponding time needed to achieve a wet steady-state condition. Presentation of the transitional aerodynamic results concentrates on the rain entry condition, although some limited observations were made of the drying dynamics for the wing after exiting the rain.

Symbols

All measurements were made in the body-axis system; however, results are presented in both the body- and wind-axis systems. (See fig. 1 for axes designation.) All data have been reduced to coefficient form as noted in the symbols list. Symbols used in table BII are given in parentheses.

A		wing aspect ratio, 6.10, b^2/S
b		wing span, 7.88 ft
C_A	(CA)	axial-force coefficient, Axial force/qS
C_D	(CD)	drag coefficient, Drag/qS
C_L	(CL)	lift coefficient, Lift/qS
$C_{L,\max}$		maximum lift coefficient
C_N	(CN)	normal-force coefficient, Normal force/qS
$\bar{c}$		mean aerodynamic chord, 1.29 ft
H		height of water droplet spray region, ft
K		conversion factor for liquid water content units
LWC		liquid water content, g/m^3 (see eq. (1))
M		Mach number
Q		volumetric flow rate, gal/min
q		dynamic pressure, psf
R		Reynolds number, $\rho V_\infty \bar{c}/\mu$
S		wing reference area, 10.17 ft^2
V_∞		free-stream wind velocity, ft/sec
W		width of water droplet spray region, ft
α	(ALPHA)	angle of attack, deg
δ		flap deflection angle (positive for trailing edge down), deg
μ		viscosity, slug/ft-sec
ρ		density, slug/ft^3

Model Description

The model used in this investigation (fig. 2) consisted of a rectangular wing mounted to a fuselage sized to accommodate an internal six-component strain-gauge balance. Note from figure 2 that the wing was not mounted on the fuselage centerline. This type of wing mounting can result in fuselage-induced wing cross flow which may affect the angle of attack for zero lift. A piezoelectric device was installed on the nose of the fuselage to signal the onset of the rain spray and therefore define the beginning of rain influence on the wing aerodynamics. The wing had an NACA 23015 airfoil section (fig. 3) and had no taper, sweep, or twist. The airfoil chord and wing span were 1.29 and 7.88 ft, respectively. The corresponding wing aspect ratio was 6.10. The plain flap was tested at 0°, 10°, and 20°. A photograph of the model mounted for testing in the Langley 14- by 22-Foot Subsonic Tunnel is shown in figure 4.

Test Description

The investigation was conducted in the Langley 14- by 22-Foot Subsonic Tunnel. This is a closed-circuit, single-return, atmospheric wind tunnel consisting of a test section 14.50 ft high by 21.75 ft wide by 50.00 ft long (ref. 12). The wind tunnel tests were conducted at nominal free-stream dynamic pressures of 10, 30, and 50 psf. Corresponding Reynolds numbers based on the mean aerodynamic chord of 1.29 ft and Mach numbers are shown in the following table:

Dynamic pressure, q, psf	Reynolds number, R	Mach number, M
10	0.76×10^6	0.08
30	1.31	.14
50	1.69	.18

The angle of attack ranged from −4° to 20° for the dry-wing baseline configurations and from 8° to 20° for the wet-wing configurations, all of which were tested at zero sideslip. Through use of the method of reference 13, a 1/8-in. spanwise strip of no. 60 transition grit was applied at a streamwise location 1.0 in. aft of the leading edge of the wing to trip the boundary layer to ensure turbulent flow.

A six-component strain-gauge balance was mounted internal to the fuselage (see fig. 2) to measure the forces and moments. The accuracy of the internal strain-gauge balance is presented in appendix A. An electronic inclinometer, mounted within the fuselage, provided angle-of-attack measurements. Changes in aerodynamic performance parameters are presented uncorrected for fuselage base and chamber pressures. The test parameters were recorded dynamically on an FM recording system and data were digitized at a rate of 50 samples per second. Analog dynamic data were plotted in real time with an oscillographic galvanometer recorder.

Rain Simulation

Generally, the parameters used to characterize rain intensity are the rainfall rate and the liquid water content (LWC). At ground level the rainfall rate is used to characterize a rain event. For airborne measurements, the relevant parameter is the LWC, which is the mass of liquid water per unit volume of air and is usually expressed in grams of water per cubic meter of air. The relationship between LWC and rainfall rate is uniquely dependent on the type and intensity level of the storm (ref. 8). Simulating a natural rain environment in a wind tunnel poses a technical difficulty in that the small-scale spray characteristics usually do not simulate the full-scale droplet characteristics for the same rain intensity (refs. 10 and 11). Since simultaneous simulation of each of the theoretical scaling relationships (ref. 14) was not possible in the present study, the parameter felt to be most important, liquid water content (LWC), was chosen as a primary test variable. The calculation of this rain parameter is addressed in detail subsequently. The wind tunnel rain system simulates thunderstorm-type rain, which is defined as being a high-intensity, short-duration rainfall. Such a rainfall, with a liquid water content value of 43 g/m^3, was measured by Schumacher and Wilk (ref. 15) in naturally occurring thunderstorms at altitude.

Rain Simulation System

An illustration of the rain simulation system is shown in figure 5. The system consisted of a 20-gal water accumulator tank, a spray manifold, and nozzles. A remotely controlled air pressure valve regulated the water supply to the tank, which was connected to the spray manifold. The air supply pressure was varied to control the water mass flow through the manifold.

A photograph of the spray manifold mounted within the wind tunnel is presented in figure 6. The manifold was fabricated from streamlined steel tubing having a chord of 3.5 in. and was positioned approximately 25 ft upstream of the model. This location was chosen to coincide with the positioning of the manifold during the nozzle calibration discussed in reference 16. This position allowed adequate time for the stabilization of the accelerating water droplets and the development of the spray region. This position also provided an adequate distance to minimize any manifold-induced wake disturbances on the wing. The manifold was positioned 6 in. above the model chord plane to account for gravity effects on the water droplets. Drop injection influences on free-stream wind velocities were calculated and found to be insignificant in relation to the scope of this study. As shown in figure 7, the manifold incorporated six nozzles, each spaced 1 ft apart along the trailing edge. The combined conical expansion patterns of the droplets from each nozzle effectively maintained model spray coverage during angle-of-attack variations of the model with little or no adjustments to the model height relative to the impinging rain. The heights of both the manifold and the model were chosen to keep both near the centerline of the tunnel, thereby minimizing wall interference effects.

Two types of nozzles were used in this investigation and are shown in figure 8. The first type of nozzle (B1N5 and B1N7, figs. 8(a) and 8(b)) was a multi-injector type which consisted of a series of 0.063-in.-diameter tubes oriented circumferentially around a plenum in either a five-tube or a seven-tube configuration. This nozzle type provided the flexibility to independently vary the nozzle mass flow while control over the drop size and drop distribution was retained by variation of the number of tubes. The second type of nozzle (1570, fig. 8(c)) was a commercially available fan jet nozzle with an elliptical cross-section orifice. This type was chosen for its high mass-flow-rate capability. A detailed study of each nozzle and its relative spray characteristics is presented in reference 16.

The dynamic response of the wing model entering a heavy-rain environment was an integral part of this investigation; therefore, the spray system had to provide instantaneous water-on and water-off capability. This feature was provided by incorporating a solenoid valve on each water nozzle (see fig. 7) and simultaneously operating them by means of a remotely controlled operations panel.

Calculation of Liquid Water Content

In the wind tunnel environment, liquid water content (LWC), defined as the mass of liquid water per unit volume of air, is calculated with the following relationship:

$$\mathrm{LWC} = \frac{KQ}{V_\infty HW} \quad (1)$$

where Q is the volumetric flow rate of water through the spray manifold, V_∞ is the free-stream wind tunnel air velocity, H and W are the height and width of the water droplet spray region at the leading edge of the wing model, and K is the units conversion factor ($K = 2225.8086$). The units of LWC are grams per cubic meter. Three different nozzle configurations were used to achieve three values of total manifold mass flow and three tunnel velocities were used for each of the three nozzles, thus providing a matrix of nine values of LWC. According to the test results of reference 16, the achievement of various LWC values by this method does affect the spray characteristics of drop size and drop distribution. The relevance of this to the aerodynamic effects of the wing model is discussed subsequently.

The height H and the width W of the water droplet spray region were determined by a photographic process which utilized manually activated cameras, high-speed strobe lights, and a near-field linear length reference. Because of the dynamic nature of water droplet sprays within the tunnel, the boundary of the spray region at any instant of time is not a precisely defined straight line; therefore, one inherent difficulty in deriving the spray region heights and widths by photographic means lies in the possible error involved in subjectively determining the usable spray region boundaries. Representative LWC values obtained in this investigation, along with the corresponding nozzle mass flow and tunnel velocities, are presented in table I.

Results and Discussion

Effects of Spray Manifold on Wing Aerodynamics

Figures 9(a) to 9(c) show the results for three tunnel velocities ($q = 10$, 30, and 50 psf). The data are for water-off conditions only (i.e., no simulated rain), with a trailing-edge flap angle of $\delta = 0°$ (cruise wing configuration). As previously mentioned, the position of the wing relative to the fuselage may result in fuselage-induced wing cross flow. This cross flow may have been the cause for the cambered airfoil of this study to have zero lift at zero angle of attack. The effects of the manifold wake were generally very small, especially for the two higher velocities. At $q = 10$ psf, the manifold wake resulted in an increase of the stall angle of attack from 14° to 18° in addition to a slight increase in drag.

Reynolds Number Effects

Varying tunnel velocity was a simple and effective means of obtaining significant variations in LWC, but it also resulted in a variation of Reynolds number from 0.76×10^6 for $q = 10$ psf to 1.69×10^6 for $q = 50$ psf. The effects of this variation in Reynolds number on the aerodynamic characteristics of the wing are presented in figures 10(a) to 10(d) for the dry wing. For this range of Reynolds numbers the effects were quite small for all configurations tested and were limited to higher angles of attack near stall. With the spray manifold removed, the Reynolds number effects were more observable but were still limited to angles of attack near stall.

Nozzle Design Effects

Before the overall static test results are discussed, it is important to note that nozzle design influenced the aerodynamics during these tests. In figure 11, two different symbols are used for LWC = 21 g/m^3, one symbol being used to designate data for the B1N7 nozzle and the other symbol being used for the 1570 nozzle. Although the measurements derived by photographic means resulted in the same LWC values for both nozzles, it is evident from the data for $\delta = 0°$ that the aerodynamic effects of the two nozzles on the wing did differ. Nozzle calibration studies (e.g., ref. 16) have shown differences in spray characteristics exist for changing LWC and nozzle types. Among these differences were variations in the arithmetic mean drop diameter, the volume percentage mean drop diameter (i.e., the volumetric contribution of each drop to the total water volume), and the dispersal pattern. These differences may have been responsible for the variation in aerodynamics results for the same value of LWC. A more detailed discussion of these parameters and their potential effects is presented in reference 14. The differences in spray characteristics, when coupled with the small Reynolds number effects discussed previously, may produce nonlinear aerodynamics results, particularly at the lower Reynolds numbers. The full impact of these nonlinearities is not yet completely understood. However, results for the high-lift configurations tested seem less sensitive to the nozzle differences, an encouraging situation since the largest degradations in aerodynamic performance are for these conditions.

Steady-State Performance Data

The portions of a flight profile in which airplanes are most susceptible to the potential influences of heavy rain are during landing and takeoff maneuvers in a potential wind shear environment wherein they may be required to operate near stall (i.e., at maximum lift coefficient). Accordingly, the angle-of-attack range for the portions of this test in which rain effects were studied was chosen to bracket the region of maximum lift coefficient $C_{L,\max}$ for this wing, generally between $\alpha = 8°$ and 20°. Tabulated test results are presented in appendix B.

Steady-state aerodynamics results are presented in figures 11 to 13 in the form of C_L versus α and C_L versus C_D at increasing tunnel velocities. Plots of C_N versus α and C_A versus α are also presented to allow a more direct correlation with the transitional data, which are discussed subsequently and which are in the form of normal and axial force.

The impact of heavy rain on the cruise configuration ($\delta = 0°$) varied with free-stream dynamic pressure. At the dynamic pressures of 10 and 30 psf (figs. 11 and 12), lift *increases* were measured for the cruise configuration below maximum lift; as dynamic pressure increased to 50 psf (fig. 13), the rain produced a lift loss above $\alpha = 10°$. At all dynamic pressures, drag increases because of rain were evident. Lift increases were also observed by Hansman and Craig in reference 9 for cruise configurations of several airfoils at a Reynolds number of 0.31×10^6. However, the lift increases noted in that reference were close to maximum lift.

The largest performance losses because of rain occurred on the high-lift configurations (i.e., $\delta = 10°$ and 20° in figs. 11 to 13). These losses agree with the findings of Dunham in reference 7. Results of that study showed greater lift losses for larger flap deflections and higher dynamic pressures. For example, results in figure 13 for $\delta = 20°$ show a 27-percent decrease in lift and a 39-percent increase in drag at the highest LWC near maximum lift ($\alpha = 14°$). Accompanying this $C_{L,\max}$ reduction is a general flattening of the lift-curve slope. This behavior is different from that of the dry-wing post-stall data, for which the lift-curve slope changes sign. For most cases the wet wing experienced an earlier, more gradual stall. This trend is also indicative of an unswept wing experiencing progressive trailing-edge separation. Although the mechanism producing these effects is not completely understood, it is known that the rain produces localized thickness variations of the airfoil in addition to creating a two-phased (water-air) boundary-layer interaction on the wing, and both may result in significant losses of maximum lift because of premature flow separation.

In general, almost all cases represented in figures 11 to 13 underwent some form of performance degradation at moderate to high angles of attack. The magnitudes of the rain effects were a function of angle of attack, with peak effects generally occurring near $\alpha = 14°$.

To better understand the wet-wing aerodynamics, observations were made of the water flow patterns existing on the wing surfaces. Figure 14(a) depicts the observed water flow characteristics at low to moderate angles of attack. For pre-stall angles, for which attached flow conditions would exist on the wing, the water adheres to the wing surface and forms the surface water patterns of droplet impact splashing, water film, and rivulet runoff discussed in references 4 and 14. It is this water-film-layer buildup, coupled with water droplets impacting the surface, which interacts with the boundary layer, and is suspected of producing the performance losses. As angle of attack is increased, providing stall has not yet been achieved, the adverse influences of the water continue to grow. The effects during wing stall on the near-field rain and surface water film are shown in figure 14(b). The separated airflow region of the upper surface of the wing causes a breakdown of the flow pattern depicted in figure 14(a) and results in regional pooling of the water, an indication of stagnated flow. The lower-surface water film behavior appears to be unaffected by the upper-surface separation and therefore still experiences the water-induced performance losses because of direct water droplet impact, which is independent of the airflow separation characteristics.

These results show the subject wing exhibited similar performance in simulated rain to that of the earlier wings studied. Additionally, the magnitude of the lift loss is proportional to the flap deflection. Establishing this static performance base was felt to be important to better explain the dynamic test results which follow.

Transitional Performance Data

An additional objective of this investigation was to determine the time required to transition from dry steady-state conditions to wet steady-state conditions. Figure 15 presents a typical sample of the instantaneous normal-force, axial-force, and piezoelectric device signal traces plotted against time. The transition time was determined by first establishing the mean values of the steady-state dry and wet portions of the traces. The moment water first impacted the model was determined by the beginning of increased amplitude on the piezoelectric trace; this became the time start reference. The transition time was then determined by the number of seconds required to go from the mean dry steady-state condition to the mean wet steady-state condition. For the data of figure 15, the transition time was 1.45 sec.

The change in the wing aerodynamics during this transition time was not always smooth as shown in figure 15. A smooth transition is defined as one in which the force data change somewhat linearly during transition from dry to wet steady-state conditions. By contrast, the data of figure 16 (which are indicative of several test cases) show a very nonlinear transition sequence. Once the final wet steady-state level was achieved, however, the mean forces remained unchanged with constant rain simulation. During the transition studies, the time for the wing to return to the dry steady-state condition was also observed for selected cases, including both cruise and high-lift configurations. Although no data are presented, transition from wet to dry steady-state conditions generally took less time than transitions from dry to wet conditions. Also, the changes in aerodynamic loads on the model during this reverse transition were smooth, without the nonlinear effects seen on some transitions from dry to wet conditions.

Although the cause for the nonlinear behavior of the wing during transition from dry to wet is not completely understood, it has been demonstrated by Hansman and Craig (ref. 9) that the transitional dynamics may be influenced by airfoil shape. The airfoil shape governs the susceptibility to premature boundary-layer transition and also affects the water film development on the wing, including the subsequent breakdown and runoff. Therefore the wing transitional behavior may be expected to vary with shape changes such as the flap deflections studied herein.

Review of the transition data obtained via the aforementioned procedure indicated the strongest trends were evident in the data obtained at the highest value of LWC and that these trends and the general consistency of the data decreased at the lower values of LWC. Therefore, for simplicity and clarity, only the results for the highest values of LWC (i.e., for the 1570 nozzles) are presented in the main body of the paper and the results for the lower values are presented in appendix C.

Since time measurements do not permit direct comparison between test cases with different tunnel speeds, transition time measurements have been converted to a nondimensional value of the equivalent number of wing chords which would be traversed within that transition time. Values of transition distance in equivalent chords are presented in figures 17 to 19 for the 1570 nozzles; similar results for the other nozzles (i.e., for lower values of LWC) are presented in appendix C. For direct comparisons of data at various dynamic pressures, it is important to note the changing ordinate (i.e., number of chords) scale. The absolute values of the performance data are plotted in bar graph form for several angles of attack. It was noted in some cases that the normal-force and axial-force transition responses differed during a test run; for this reason, separate plots for normal and axial force are presented. Those cases which displayed a nonlinear (step function) transition are represented by bar graphs with changing shades (see, for example, axial-force portion of fig. 17(a)), each shade representing the number of chords traversed before the next step took place. The percent of the total change in aerodynamic performance is shown on each graph for nonlinear transition from dry to wet steady-state performance. The top of the bar graph represents the achievement of the final wet steady-state condition.

Analysis of the transition data presented in figures 17 to 19 for angles of attack above 12° to 14° (range of largest lift losses) shows some mild trends. For $\delta = 0°$ and 20°, the transition was generally longer than for $\delta = 10°$ at a given dynamic pressure. As dynamic pressure was increased, the transition length also increased substantially for $\delta = 0°$ and 20° but remained relatively constant for $\delta = 10°$. Finally, the frequency of occurrence of nonlinear transition seems to have been most evident at the highest dynamic pressures and the highest flap deflections.

Summary of Results

An investigation of the effects of simulated rain on the steady-state and transitional aerodynamic performance of a wing model with a 1.29-ft chord and an NACA 23015 airfoil was conducted. Data were obtained at dynamic pressures of 10, 30, and 50 psf (i.e., at Reynolds numbers of 0.76×10^6, 1.31×10^6, and 1.69×10^6) in the Langley 14- by 22-Foot Subsonic Tunnel. Test variables of liquid water content, tunnel dynamic pressure, angle of attack, and trailing-edge flap angle were parametrically varied to study the aerodynamic trends during a simulated rain encounter. These aerodynamic trends for the wet wing, while evident for this wing model, may incorporate the effects of both Reynolds number and spray characteristics, which may produce nonlinear results that are not yet clearly understood. Results of this study can be summarized as follows:

1. As in previous investigations, heavy rain produced large losses in wing aerodynamic performance at high-lift conditions. A 27-percent decrease in lift and a 39-percent increase in drag were observed for the highest flap deflection at the highest test speed.

2. The largest performance losses because of rain occurred for angles of attack near maximum lift. This angle of attack for maximum lift for the wet wing was several degrees below that for the dry wing.

3. The aerodynamics of the wing as it entered the rain field exhibited both linear and highly nonlinear (stepwise) characteristics as it transitioned from dry to wet; nonlinear behavior was more evident at higher speeds and higher flap settings.

Appendix A

Data Accuracy

The internal strain-gauge balance used in this investigation has an accuracy rating no worse than ±0.5 percent of full-scale loading. The corresponding error range for each component is as follows:

Component	Load	Error
Normal force, lbf	±3000	±15
Axial force, lbf	±500	±3
Pitching moment, in-lbf . . .	±25 000	±125
Rolling moment, in-lbf . . .	±9900	±50
Yawing moment, in-lbf . . .	±10 000	±50
Side force, lbf	±1000	±5

The coefficient accuracies at $\alpha = 0°$ are as follows:

Coefficient	Accuracy for q, psf, of—		
	10	30	50
C_L	±0.15	±0.05	±0.03
C_D	±0.03	±0.01	±0.01

Appendix B

Tabulated Test Results of Steady-State Data

Table BI is an index to the data presented in table BII.

Table BI. Index to Data Tables

Run	δ, deg	q, psf	LWC, g/m^3	Nozzle
2*	0	10		
5				
93			14	B1N5
94			21	B1N7
42		↓	21	1570
3*		30		
6				
44			12	B1N5
56			17	B1N7
41		↓	23	1570
4*		50		
7				
61			10	B1N5
55			15	B1N7
40	↓	↓	22	1570
8	10	10		
48			14	B1N5
88			21	B1N7
89		↓	21	1570
9		30		
47			12	B1N5
50			17	B1N7
90		↓	23	1570
10		50		
46			10	B1N5
49			15	B1N7
92	↓	↓	22	1570
11	20	10		
84			14	B1N5
87			21	B1N7
81		↓	21	1570
12		30		
83			12	B1N5
86			17	B1N7
80		↓	23	1570
13		50		
82			10	B1N5
85			15	B1N7
24	↓	↓	22	1570

*These runs are without the spray manifold installed.

Table BII. Test Data

14X22 FOOT TUNNEL TEST 334 RUN 2

Q (PSF)	ALPHA (DEG)	CL	CD	CN	CA
10.12	-4.18	-.25105	.01836	-.25172	-.00001
10.12	-2.09	-.11179	.01025	-.11209	.00617
10.12	-.07	.01013	.01355	.01012	.01356
10.12	2.20	.16995	.01025	.17022	.00370
10.00	4.07	.29311	.01452	.29340	-.00632
10.00	6.06	.42859	.01551	.42783	-.02984
10.00	8.03	.56516	.01842	.56218	-.06075
10.00	10.18	.70477	.03217	.69936	-.09289
10.00	12.05	.81429	.04238	.80519	-.12857
10.00	14.22	.93776	.07908	.92846	-.15365
10.00	16.10	.91735	.12819	.91693	-.13117
10.00	18.15	.85049	.18670	.86633	-.08753
10.00	20.03	.88489	.22264	.90763	-.09391

14X22 FOOT TUNNEL TEST 334 RUN 3

Q (PSF)	ALPHA (DEG)	CL	CD	CN	CA
30.00	-4.15	-.27186	.02026	-.27262	.00055
30.12	-1.97	-.12248	.01652	-.12298	.01229
30.00	.01	.02221	.01351	.02221	.01350
30.00	2.07	.16852	.01539	.16897	.00929
30.00	4.03	.30699	.01648	.30738	-.00513
29.89	6.05	.45462	.02216	.45442	-.02589
30.00	8.18	.59720	.03062	.59548	-.05464
29.77	10.04	.72207	.03966	.71792	-.08683
29.89	12.10	.86504	.05532	.85741	-.12723
29.39	14.04	.98085	.07370	.96944	-.16642
30.12	16.03	1.00214	.12120	.99664	-.16028
30.12	18.03	1.02608	.16379	1.02640	-.16178
30.12	20.13	1.03036	.20116	1.03665	-.16574

Table BII. Continued

14X22 FOOT TUNNEL TEST 334 RUN 4

Q (PSF)	ALPHA (DEG)	CL	CD	CN	CA
50.12	-4.05	-.26532	.02151	-.26618	.00272
50.01	-2.04	-.12057	.01614	-.12107	.01184
50.01	.04	.02902	.01518	.02903	.01516
50.01	2.09	.17394	.01468	.17436	.00832
50.01	4.14	.32258	.01747	.32300	-.00586
49.78	6.09	.46110	.02344	.46098	-.02562
49.78	8.09	.60139	.03243	.59997	-.05248
50.24	10.04	.73052	.04183	.72663	-.08613
49.78	12.08	.87071	.05639	.86324	-.12702
49.89	14.16	.98342	.08795	.97504	-.15535
49.89	16.20	1.02041	.13275	1.01692	-.15724
50.01	18.19	1.00643	.17121	1.00959	-.15150
49.89	20.08	1.01436	.20967	1.02469	-.15133

14X22 FOOT TUNNEL TEST 334 RUN 5

Q (PSF)	ALPHA (DEG)	CL	CD	CN	CA
10.23	-4.13	-.27725	.02637	-.27843	.00632
10.12	-2.00	-.11676	.02111	-.11742	.01702
10.00	-.01	.00073	.02119	.00072	.02119
10.23	2.01	.14940	.02077	.15004	.01551
10.12	4.07	.28478	.02450	.28580	.00421
10.12	6.08	.43140	.02828	.43197	-.01754
10.12	8.09	.54087	.03623	.54059	-.04020
10.00	10.07	.68756	.04977	.68566	-.07126
10.00	12.00	.78398	.05330	.77792	-.11091
10.12	14.06	.88974	.06960	.88000	-.14862
10.00	16.01	.97568	.10755	.96750	-.16572
10.12	18.01	1.02259	.15211	1.01950	-.17158
10.12	20.04	1.01220	.19227	1.01679	-.16630

Table BII. Continued

14X22 FOOT TUNNEL TEST 334 RUN 6

Q (PSF)	ALPHA (DEG)	CL	CD	CN	CA
30.69	-4.16	-.29233	.02670	-.29350	.00541
30.58	-2.00	-.13369	.01998	-.13431	.01530
30.35	-.02	.00724	.01781	.00723	.01782
30.23	2.06	.15087	.01934	.15147	.01391
30.23	4.02	.28370	.02250	.28458	.00257
30.23	6.21	.43572	.02899	.43630	-.01831
30.23	8.08	.55763	.03707	.55730	-.04172
30.12	10.01	.69356	.04759	.69128	-.07363
30.00	12.18	.83067	.06113	.82488	-.11547
29.89	14.05	.95175	.07793	.94208	-.15618
29.77	16.10	1.02635	.11835	1.01892	-.17091
29.77	18.07	1.07063	.15748	1.06666	-.18243
29.66	20.02	1.05536	.19954	1.05990	-.17385

14X22 FOOT TUNNEL TEST 334 RUN 7

Q (PSF)	ALPHA (DEG)	CL	CD	CN	CA
50.35	-4.05	-.27767	.02504	-.27875	.00517
50.24	-2.00	-.13391	.02058	-.13455	.01589
50.24	.01	.01005	.01833	.01006	.01833
50.24	2.06	.15212	.01757	.15266	.01209
50.01	4.06	.29250	.02217	.29334	.00140
50.01	6.02	.42690	.02787	.42746	-.01709
49.89	8.10	.56366	.03397	.56282	-.04578
49.89	10.01	.70486	.04661	.70223	-.07666
49.66	12.06	.82229	.06796	.81833	-.10539
49.43	13.99	.92504	.09321	.92013	-.13322
50.35	16.21	1.02685	.12051	1.01968	-.17085
50.12	18.13	1.05387	.16129	1.05174	-.17461
50.01	20.02	1.01114	.21044	1.02207	-.14851

Table BII. Continued

14X22 FOOT TUNNEL TEST 334 RUN 8

Q (PSF)	ALPHA (DEG)	CL	CD	CN	CA
10.23	-4.05	.04968	.02638	.04769	.02982
10.23	-2.04	.18456	.02870	.18342	.03526
10.23	-.01	.32890	.03281	.32889	.03284
10.23	2.02	.46716	.03680	.46817	.02032
10.23	4.00	.57217	.04165	.57368	.00160
10.23	6.05	.71533	.05217	.71684	-.02353
10.23	8.18	.83852	.06480	.83921	-.05517
10.12	10.16	.97716	.08150	.97621	-.09217
10.12	12.15	1.09489	.09806	1.09100	-.13455
10.12	14.12	1.19411	.12116	1.18759	-.17377
10.23	15.98	1.19182	.15668	1.18890	-.17751
10.23	18.07	1.15459	.21191	1.16339	-.15658
10.00	20.08	1.14093	.26857	1.16379	-.13947

14X22 FOOT TUNNEL TEST 334 RUN 9

Q (PSF)	ALPHA (DEG)	CL	CD	CN	CA
30.00	-4.00	.06160	.02553	.05967	.02977
30.12	-2.07	.18658	.02656	.18550	.03329
30.00	.02	.33093	.03075	.33094	.03062
30.00	2.09	.46725	.03909	.46836	.02203
29.89	4.00	.59693	.04631	.59871	.00453
29.77	6.11	.72670	.05817	.72877	-.01944
29.89	8.04	.85879	.06957	.86008	-.05116
30.00	10.08	.99322	.08706	.99312	-.08810
30.00	12.03	1.12054	.10492	1.11779	-.13101
29.89	14.04	1.23164	.12588	1.22539	-.17665
29.89	16.07	1.28084	.17549	1.27937	-.18594
29.89	18.00	1.19152	.23453	1.20567	-.14515
30.12	20.16	1.15560	.28784	1.18401	-.12797

Table BII. Continued

14X22 FOOT TUNNEL TEST 334 RUN 10

Q (PSF)	ALPHA (DEG)	CL	CD	CN	CA
50.24	-4.01	.06419	.02510	.06227	.02953
50.12	-2.03	.18729	.02620	.18624	.03282
50.01	-.02	.33456	.03027	.33455	.03038
49.78	2.14	.48300	.03813	.48409	.02005
50.24	4.17	.62162	.04766	.62344	.00237
50.12	6.09	.75504	.05896	.75703	-.02151
50.01	8.16	.88987	.07261	.89117	-.05441
50.12	10.04	1.01593	.08764	1.01564	-.09090
49.89	12.09	1.14303	.10685	1.14005	-.13495
50.35	14.03	1.24573	.12726	1.23942	-.17852
50.12	16.01	1.29060	.17440	1.28864	-.18835
50.01	18.05	1.21143	.23637	1.22506	-.15057
50.12	20.28	1.13666	.29510	1.16849	-.11716

14X22 FOOT TUNNEL TEST 334 RUN 11

Q (PSF)	ALPHA (DEG)	CL	CD	CN	CA
10.00	-4.03	.25890	.05065	.25470	.06872
10.00	-2.09	.43150	.04999	.42939	.06568
10.00	.03	.55941	.05858	.55944	.05830
10.00	2.12	.68783	.06883	.68991	.04328
10.12	4.14	.82590	.08187	.82966	.02208
10.12	6.07	.94111	.09729	.94613	-.00283
10.00	8.03	1.08542	.11316	1.09058	-.03950
10.00	10.02	1.20777	.13403	1.21267	-.07809
10.00	12.03	1.32581	.15245	1.32847	-.12719
10.00	14.13	1.38349	.18592	1.38703	-.15733
10.00	16.16	1.34751	.24126	1.36141	-.14341
10.00	18.07	1.30184	.30612	1.33259	-.11269
9.89	20.08	1.27619	.36146	1.32273	-.09857

Table BII. Continued

14X22 FOOT TUNNEL TEST 334 RUN 12

Q (PSF)	ALPHA (DEG)	CL	CD	CN	CA
30.35	-4.01	.28212	.04999	.27794	.06959
30.35	-2.10	.40458	.05457	.40230	.06935
30.35	.00	.55266	.06380	.55267	.06375
30.23	2.02	.68774	.07241	.68987	.04813
30.12	4.04	.81758	.08246	.82135	.02466
30.00	6.07	.95871	.09696	.96359	-.00492
30.00	8.08	1.08610	.11653	1.09169	-.03730
29.89	10.02	1.21109	.13538	1.21618	-.07734
29.89	12.05	1.33822	.15867	1.34186	-.12416
30.23	13.95	1.42560	.17594	1.42597	-.17291
30.00	16.16	1.43820	.24056	1.44833	-.16914
30.00	18.15	1.30962	.30670	1.34001	-.11644
30.12	20.04	1.24454	.36469	1.29416	-.08388

14X22 FOOT TUNNEL TEST 334 RUN 13

Q (PSF)	ALPHA (DEG)	CL	CD	CN	CA
50.35	-4.01	.26682	.04831	.26278	.06687
50.24	-2.10	.40409	.05354	.40185	.06833
50.12	.01	.55325	.06162	.55326	.06157
50.01	2.01	.69331	.07105	.69537	.04673
50.12	4.04	.82654	.08454	.83044	.02615
49.89	6.07	.96821	.09889	.97324	-.00402
49.89	8.07	1.09511	.11684	1.10067	-.03799
50.12	10.01	1.22197	.13392	1.22665	-.08042
50.01	12.05	1.34521	.15657	1.34817	-.12857
49.89	14.13	1.45491	.18130	1.45517	-.17924
50.24	16.00	1.40706	.24229	1.41934	-.15494
50.24	18.22	1.27707	.31792	1.31245	-.09728
50.12	20.19	1.20447	.37153	1.25868	-.06697

Table BII. Continued

14X22 FOOT TUNNEL TEST 334 RUN 24

Q (PSF)	ALPHA (DEG)	CL	CD	CN	CA
50.12	7.95	1.00331	.12757	1.01130	-.01319
50.35	10.04	1.09974	.14556	1.10828	-.04838
50.24	11.96	1.08820	.19865	1.10574	-.03112
50.24	13.96	1.06598	.25147	1.09516	-.01303
50.12	15.87	1.06317	.28939	1.10179	-.01238
50.01	18.02	1.09333	.34000	1.14488	-.01488
50.24	19.94	1.07653	.38119	1.14195	-.00881

14X22 FOOT TUNNEL TEST 334 RUN 40

Q (PSF)	ALPHA (DEG)	CL	CD	CN	CA
49.89	8.03	.60057	.06922	.60435	-.01532
50.12	10.03	.68983	.08661	.69437	-.03485
49.89	11.95	.76432	.11206	.77096	-.04857
50.01	13.98	.81474	.14748	.82623	-.05376
49.89	15.92	.87812	.17659	.89288	-.07099
50.01	17.94	.91553	.22388	.93997	-.06905
49.89	19.99	.95459	.26716	.98841	-.07531

14X22 FOOT TUNNEL TEST 334 RUN 41

Q (PSF)	ALPHA (DEG)	CL	CD	CN	CA
29.89	8.00	.69654	.07503	.70020	-.02269
30.12	10.00	.81541	.08999	.81865	-.05296
30.00	11.96	.88571	.14074	.89565	-.04586
30.00	13.92	.91766	.18035	.93410	-.04573
29.89	15.99	.98579	.21317	1.00638	-.06659
30.00	18.06	1.04235	.24514	1.06700	-.09002
30.00	20.04	1.09887	.29070	1.13195	-.10355

Table BII. Continued

14X22 FOOT TUNNEL TEST 334 RUN 42

Q (PSF)	ALPHA (DEG)	CL	CD	CN	CA
10.00	8.01	.74479	.07481	.74794	-.02975
10.12	10.01	.84711	.08554	.84908	-.06298
10.00	11.99	.95244	.13219	.95911	-.06862
10.12	13.99	.98288	.16472	.99354	-.07783
10.00	15.99	1.04959	.23162	1.07278	-.06653
10.00	17.96	1.04585	.29151	1.08477	-.04527
10.00	19.98	1.08211	.34180	1.13377	-.04852

14X22 FOOT TUNNEL TEST 334 RUN 44

Q (PSF)	ALPHA (DEG)	CL	CD	CN	CA
29.89	7.99	.51086	.06182	.51449	-.00980
29.89	10.03	.64753	.07741	.65112	-.03650
30.12	11.96	.76120	.09695	.76477	-.06292
30.00	13.94	.80621	.12860	.81345	-.06942
29.89	15.96	.81788	.16833	.83264	-.06304
29.89	17.99	.86264	.19718	.88136	-.07893
29.77	19.98	.83768	.25350	.87388	-.04796

14X22 FOOT TUNNEL TEST 334 RUN 46

Q (PSF)	ALPHA (DEG)	CL	CD	CN	CA
50.01	7.99	.75560	.06705	.75759	-.03860
50.12	10.08	.87124	.08273	.87227	-.07107
50.12	11.97	.97071	.10100	.97056	-.10247
50.01	13.90	.92457	.16036	.93602	-.06637
50.12	15.89	.96895	.19235	.98459	-.08023
50.01	17.96	1.00028	.23102	1.02278	-.08860
50.01	19.94	.97213	.28465	1.01093	-.06390

Table BII. Continued

14X22 FOOT TUNNEL TEST 334 RUN 47

Q (PSF)	ALPHA (DEG)	CL	CD	CN	CA
30.00	8.03	.74517	.06922	.74753	-.03561
29.89	10.05	.86781	.08911	.87005	-.06363
30.00	12.00	.92158	.12854	.92816	-.06592
30.00	13.99	1.00561	.15131	1.01236	-.09627
29.89	15.99	1.00576	.20110	1.02225	-.08378
30.00	18.02	1.04819	.24344	1.07209	-.09269
29.89	19.99	1.06643	.27882	1.09749	-.10261

14X22 FOOT TUNNEL TEST 334 RUN 48

Q (PSF)	ALPHA (DEG)	CL	CD	CN	CA
10.12	8.03	.74087	.09469	.74683	-.00976
10.23	10.02	.86383	.11063	.86989	-.04142
10.12	11.97	.94635	.15412	.95774	-.04548
10.12	14.00	1.02331	.18896	1.03863	-.06429
10.00	15.99	1.04817	.24151	1.07415	-.05653
10.12	17.97	1.11057	.27734	1.14196	-.07887
10.00	20.02	1.07635	.34167	1.12827	-.04755

14X22 FOOT TUNNEL TEST 334 RUN 49

Q (PSF)	ALPHA (DEG)	CL	CD	CN	CA
49.89	7.92	.74696	.07242	.74981	-.03125
49.78	10.01	.85804	.08637	.85999	-.06407
50.24	11.94	.89320	.12331	.89939	-.06413
50.24	13.91	.91614	.16778	.92960	-.05745
50.01	15.89	.97843	.20503	.99718	-.07072
49.89	17.93	.95736	.25357	.98893	-.05339
49.78	19.94	.99157	.29814	1.03380	-.05792

Table BII. Continued

14X22 FOOT TUNNEL TEST 334 RUN 50

Q (PSF)	ALPHA (DEG)	CL	CD	CN	CA
30.12	7.98	.74640	.08012	.75030	-.02422
30.00	9.98	.86580	.09858	.86979	-.05296
30.00	11.94	.92341	.13455	.93128	-.05934
30.12	13.96	.94866	.17476	.96281	-.05920
30.12	15.90	1.00063	.21308	1.02072	-.06919
29.89	17.97	1.03824	.24595	1.06348	-.08634
29.89	19.95	.99601	.29457	1.03670	-.06375

14X22 FOOT TUNNEL TEST 334 RUN 55

Q (PSF)	ALPHA (DEG)	CL	CD	CN	CA
50.01	7.96	.55647	.04343	.55712	-.03407
50.01	10.04	.67744	.06104	.67771	-.05803
50.12	11.94	.73497	.09886	.73952	-.05537
49.78	13.85	.76707	.13691	.77754	-.05074
50.12	15.87	.82260	.17111	.83804	-.06031
50.24	17.93	.89342	.20225	.91230	-.08260
49.89	19.93	.86795	.24717	.90022	-.06357

14X22 FOOT TUNNEL TEST 334 RUN 56

Q (PSF)	ALPHA (DEG)	CL	CD	CN	CA
29.89	8.01	.58548	.07332	.58998	-.00897
30.12	9.98	.71050	.08962	.71528	-.03483
30.00	11.97	.76175	.11772	.76960	-.04278
30.00	13.91	.78327	.15098	.79660	-.04171
30.00	15.85	.84273	.17911	.85957	-.05843
29.89	18.02	.90042	.21088	.92150	-.07798
30.23	20.01	.93939	.25080	.96850	-.08575

Table BII. Continued

14X22 FOOT TUNNEL TEST 334 RUN 61

Q (PSF)	ALPHA (DEG)	CL	CD	CN	CA
50.01	8.08	.53807	.03294	.53736	-.04305
50.35	10.09	.65926	.05092	.65799	-.06535
50.12	11.97	.73083	.08530	.73263	-.06818
50.24	14.00	.75026	.13066	.75958	-.05479
50.24	15.93	.80257	.16193	.81620	-.06454
50.24	18.02	.86591	.19412	.88348	-.08325
50.24	19.96	.84436	.23923	.87531	-.06331

14X22 FOOT TUNNEL TEST 334 RUN 80

Q (PSF)	ALPHA (DEG)	CL	CD	CN	CA
30.12	8.01	.98736	.12411	.99502	-.01469
30.12	10.04	1.09178	.14608	1.10053	-.04643
30.00	12.01	1.04561	.20936	1.06628	-.01284
29.89	13.97	1.08400	.25013	1.11233	-.01894
30.00	16.00	1.11290	.28715	1.14894	-.03081
30.12	17.99	1.12310	.33064	1.17031	-.03246
30.12	19.99	1.07484	.37512	1.13832	-.01484

14X22 FOOT TUNNEL TEST 334 RUN 81

Q (PSF)	ALPHA (DEG)	CL	CD	CN	CA
10.00	8.07	.97112	.13852	.98095	.00075
10.00	10.08	1.03529	.17414	1.04979	-.00971
10.12	12.00	1.05967	.22051	1.08236	-.00458
10.00	14.10	1.12129	.26685	1.15252	-.01441
10.00	16.05	1.14793	.29736	1.18540	-.03163
10.12	18.03	1.21138	.35140	1.26066	-.04070
10.00	20.03	1.14650	.39633	1.21290	-.02037

Table BII. Continued

14X22 FOOT TUNNEL TEST 334 RUN 82

Q (PSF)	ALPHA (DEG)	CL	CD	CN	CA
50.35	8.03	1.02791	.12223	1.03491	-.02247
50.12	10.03	1.14235	.14125	1.14949	-.05987
50.24	12.01	1.16267	.19089	1.17694	-.05520
50.01	14.01	1.23513	.23000	1.25407	-.07581
50.12	15.90	1.15260	.28107	1.18550	-.04551
50.12	17.99	1.15667	.32362	1.20008	-.04942
50.12	20.00	1.09929	.37839	1.16241	-.02042

14X22 FOOT TUNNEL TEST 334 RUN 83

Q (PSF)	ALPHA (DEG)	CL	CD	CN	CA
30.12	8.04	1.00892	.12386	1.01633	-.01849
30.00	10.00	1.12416	.14189	1.13172	-.05553
30.12	12.00	1.15771	.19149	1.17222	-.05346
30.00	14.03	1.24490	.22954	1.26340	-.07912
30.12	16.02	1.18140	.28801	1.21500	-.04913
30.12	17.98	1.20143	.32823	1.24408	-.05857
30.23	20.04	1.13041	.38061	1.19239	-.02975

14X22 FOOT TUNNEL TEST 334 RUN 84

Q (PSF)	ALPHA (DEG)	CL	CD	CN	CA
10.12	8.07	.99667	.12552	1.00442	-.01559
10.00	10.12	1.16199	.15468	1.17109	-.05190
10.00	12.03	1.14909	.20178	1.16591	-.04214
10.00	14.07	1.24193	.24269	1.26367	-.06654
10.12	16.05	1.17765	.29781	1.21408	-.03939
10.00	18.01	1.17616	.33747	1.22287	-.04276
10.00	20.00	1.16624	.37499	1.22417	-.04650

Table BII. Continued

14X22 FOOT TUNNEL TEST 334 RUN 85

Q (PSF)	ALPHA (DEG)	CL	CD	CN	CA
49.89	7.98	1.01599	.12176	1.02305	-.02047
49.89	10.02	1.13332	.14170	1.14068	-.05769
50.01	12.00	1.15470	.19139	1.16926	-.05282
50.01	13.92	1.10530	.24037	1.13066	-.03261
49.78	15.90	1.14324	.28188	1.17672	-.04211
50.12	18.04	1.16233	.32596	1.20613	-.04991
50.24	20.02	1.09612	.37256	1.15743	-.02520

14X22 FOOT TUNNEL TEST 334 RUN 86

Q (PSF)	ALPHA (DEG)	CL	CD	CN	CA
30.00	8.05	.99467	.12212	1.00197	-.01839
29.89	10.02	1.11933	.14286	1.12711	-.05406
29.89	12.02	1.14997	.19507	1.16538	-.04865
29.89	13.96	1.13040	.24089	1.15513	-.03888
30.00	15.95	1.16552	.27676	1.19670	-.05414
30.00	17.97	1.19345	.32092	1.23424	-.06285
30.12	20.00	1.19601	.36771	1.24964	-.06349

14X22 FOOT TUNNEL TEST 334 RUN 87

Q (PSF)	ALPHA (DEG)	CL	CD	CN	CA
9.89	8.03	.97894	.12170	.98634	-.01633
10.00	10.04	1.06778	.14487	1.07669	-.04355
10.00	12.05	1.11585	.19001	1.13093	-.04708
10.00	14.03	1.12380	.24599	1.14991	-.03380
10.00	16.04	1.14048	.27765	1.17280	-.04824
10.00	18.04	1.19489	.32675	1.23735	-.05928
10.00	20.06	1.16164	.35960	1.21452	-.06062

Table BII. Continued

14X22 FOOT TUNNEL TEST 334 RUN 88

Q (PSF)	ALPHA (DEG)	CL	CD	CN	CA
10.00	8.02	.83239	.07924	.83530	-.03766
10.00	10.01	.94129	.10006	.94436	-.06509
10.12	12.00	.99698	.13973	1.00425	-.07054
10.00	14.04	1.08079	.18100	1.09242	-.08655
10.12	16.04	1.04947	.23023	1.07223	-.06866
10.12	18.06	1.10234	.26919	1.13149	-.08572
9.89	19.98	1.14635	.31420	1.18471	-.09648

14X22 FOOT TUNNEL TEST 334 RUN 89

Q (PSF)	ALPHA (DEG)	CL	CD	CN	CA
10.12	8.04	.84321	.09602	.84835	-.02282
10.12	10.03	.91576	.12964	.92434	-.03187
10.12	12.00	.96103	.17289	.97598	-.03075
10.00	14.04	1.02404	.21624	1.04591	-.03874
10.12	16.07	1.05860	.24651	1.08547	-.05612
10.00	18.04	1.13147	.28929	1.16543	-.07538
10.12	20.03	1.23467	.30932	1.26594	-.13227

14X22 FOOT TUNNEL TEST 334 RUN 90

Q (PSF)	ALPHA (DEG)	CL	CD	CN	CA
30.12	7.95	.79685	.08601	.80108	-.02499
29.89	10.00	.89613	.11270	.90208	-.04466
30.00	11.99	.96548	.14910	.97540	-.05468
30.00	13.96	.96794	.19118	.98547	-.04793
30.00	15.99	.99863	.22594	1.02224	-.05787
30.00	17.99	1.04591	.26576	1.07686	-.07026
30.12	20.01	1.08973	.30660	1.12886	-.08482

Table BII. Concluded

14X22 FOOT TUNNEL TEST 334 RUN 92

Q (PSF)	ALPHA (DEG)	CL	CD	CN	CA
50.12	7.99	.82098	.08207	.82442	-.03278
50.12	10.00	.88658	.11596	.89325	-.03967
49.89	11.96	.93397	.14986	.94475	-.04694
50.12	13.97	.94055	.18806	.95813	-.04454
49.89	15.95	.98059	.22660	1.00511	-.05165
50.12	17.92	1.00537	.27103	1.03999	-.05138
50.01	20.00	1.00600	.31316	1.05244	-.04988

14X22 FOOT TUNNEL TEST 334 RUN 93

Q (PSF)	ALPHA (DEG)	CL	CD	CN	CA
10.23	8.02	.55371	.04708	.55486	-.03068
10.35	10.01	.68861	.06693	.68976	-.05380
10.12	12.02	.79896	.09228	.80066	-.07610
10.12	13.99	.83381	.13082	.84069	-.07471
10.12	16.00	.90958	.16787	.92060	-.08942
10.12	18.03	.96071	.20012	.97548	-.10701
10.12	19.99	.99543	.24015	1.01756	-.11458

14X22 FOOT TUNNEL TEST 334 RUN 94

Q (PSF)	ALPHA (DEG)	CL	CD	CN	CA
10.12	8.00	.55681	.04632	.55783	-.03166
10.23	10.01	.66980	.05649	.66942	-.06081
10.12	12.02	.78752	.08301	.78754	-.08281
10.00	14.03	.83596	.11252	.83830	-.09346
10.00	16.01	.87834	.16111	.88871	-.08732
10.12	18.00	.91918	.19476	.93437	-.09885
9.89	20.00	1.01468	.23937	1.03536	-.12213

Appendix C

Steady-State and Transitional Aerodynamic Data

Results are presented for the lower range of LWC values obtained with the B1N7 and B1N5 spray nozzles. (See table I for values of LWC.) The transitional aerodynamics are highlighted herein and are presented in a bar graph format that is described in the main text in the *Results and Discussion* section. Accompanying the transitional results are the static aerodynamics shown in both body- and wind-axis systems.

Results for the B1N7 nozzles are presented in figures C1 to C3 and those for the B1N5 nozzles are presented in figures C4 to C6. These results are incomplete in that transitional data were not obtained at the same angles of attack for each flap and dynamic pressure condition. This problem is more evident in the data presented in this appendix than in those presented in the main text.

In general, the tendency for longer transitions at the higher dynamic pressures is evident for the midrange values of LWC (15 to 21 g/m^3), but this trend actually seems to disappear or reverse at the lowest values of LWC (10 to 14 g/m^3). At the lowest values of LWC, the transitional behavior appears to become consistently more complex (e.g., exhibiting secondary and tertiary stages much more frequently) than at higher values of LWC.

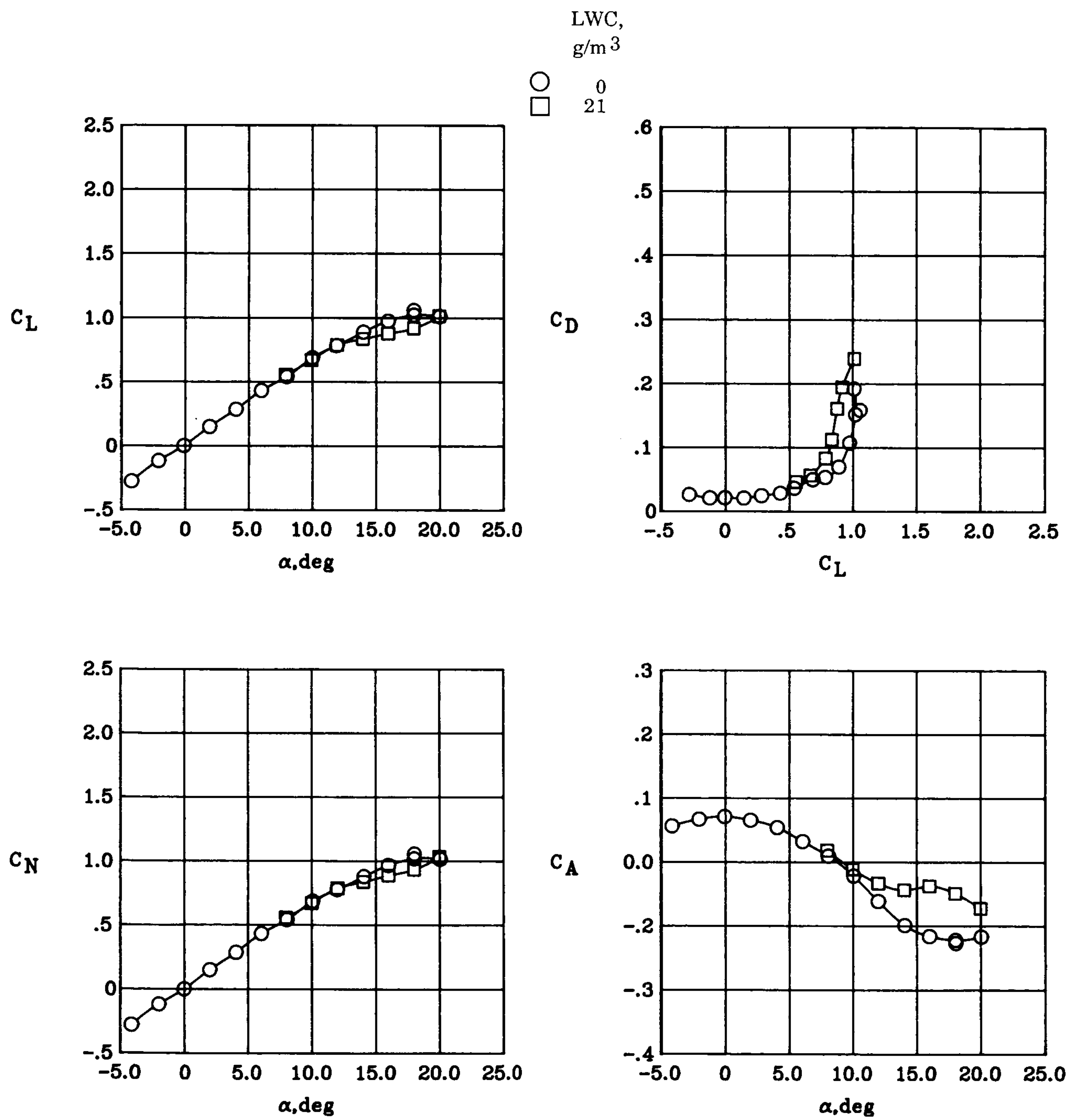

(a) $\delta = 0°$.

Figure C1. Dry to wet transition time graphs and steady-state force data for B1N7 nozzles and $q = 10$ psf.

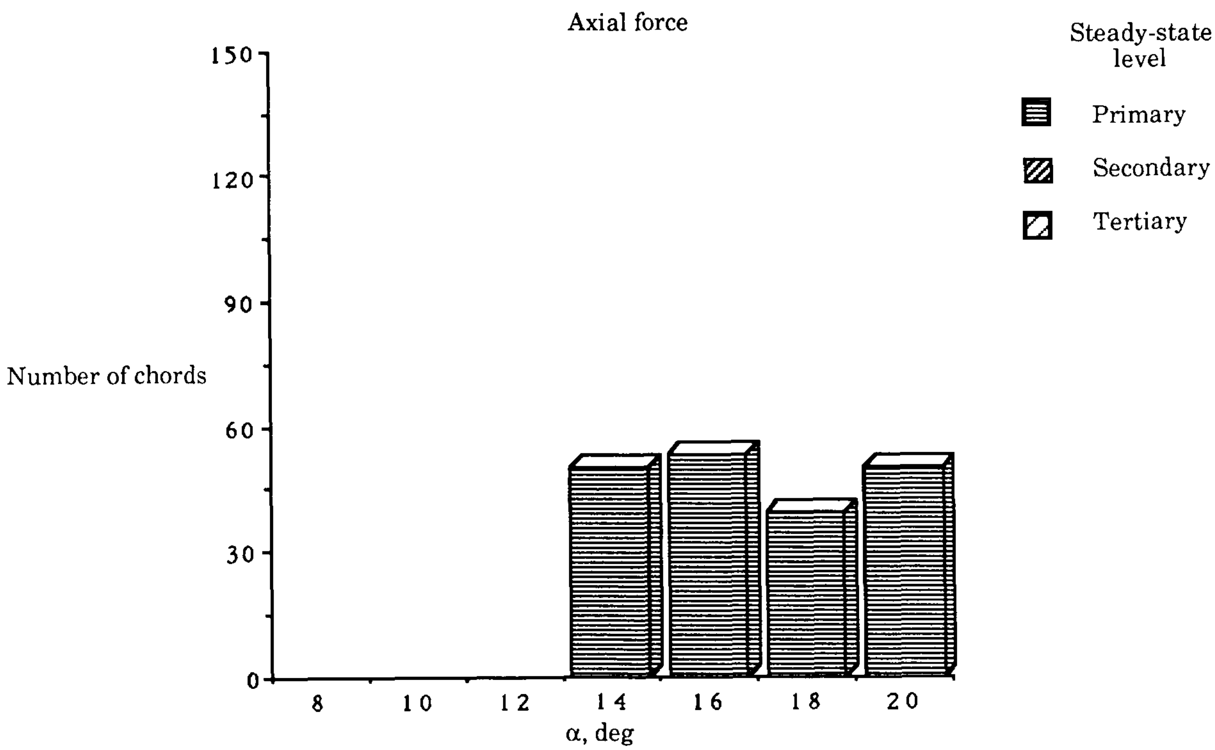

(b) $\delta = 10°$ and LWC = 21 g/m^3.

Figure C1. Continued.

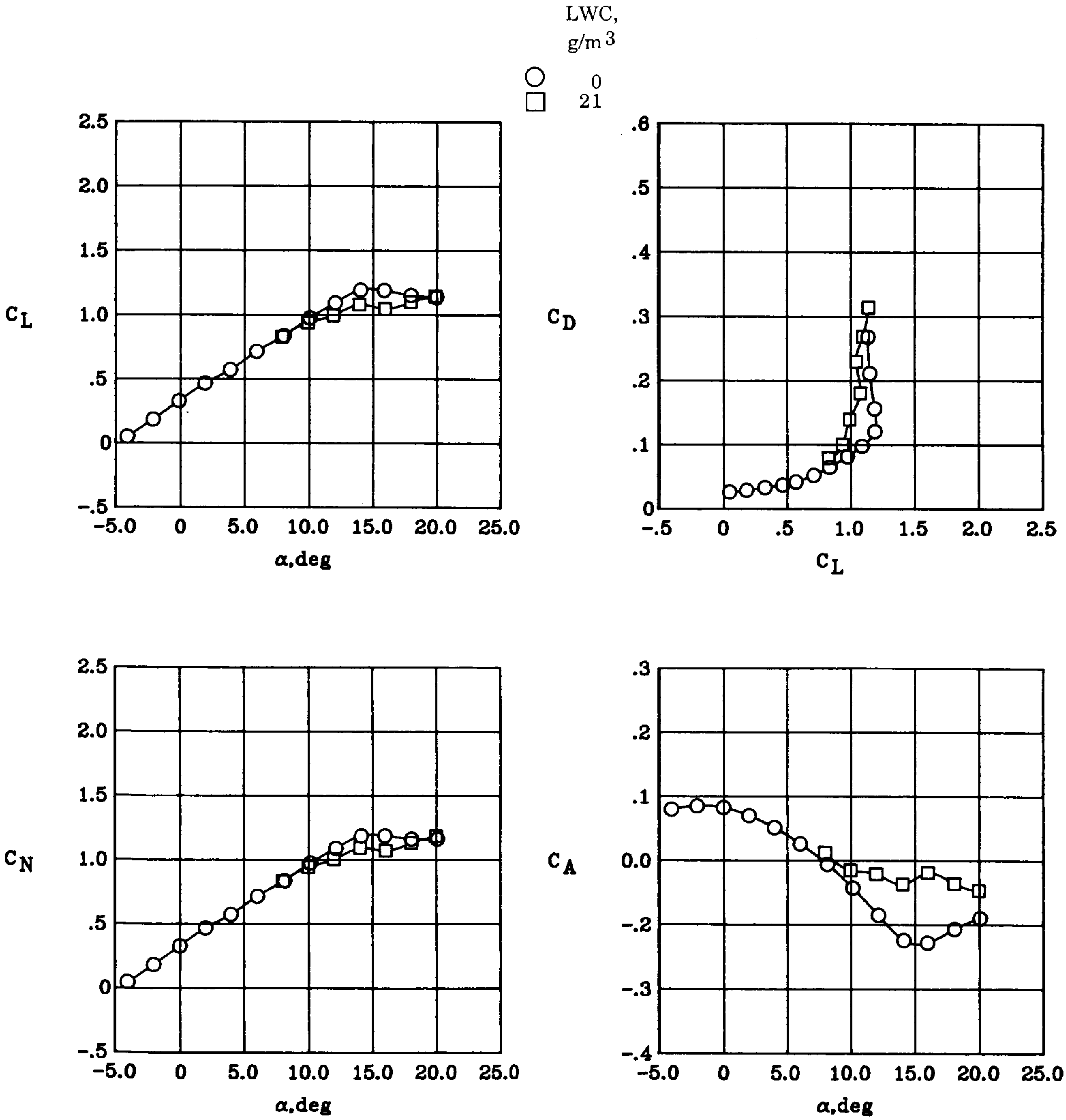

(c) $\delta = 10^{\circ}$.

Figure C1. Continued.

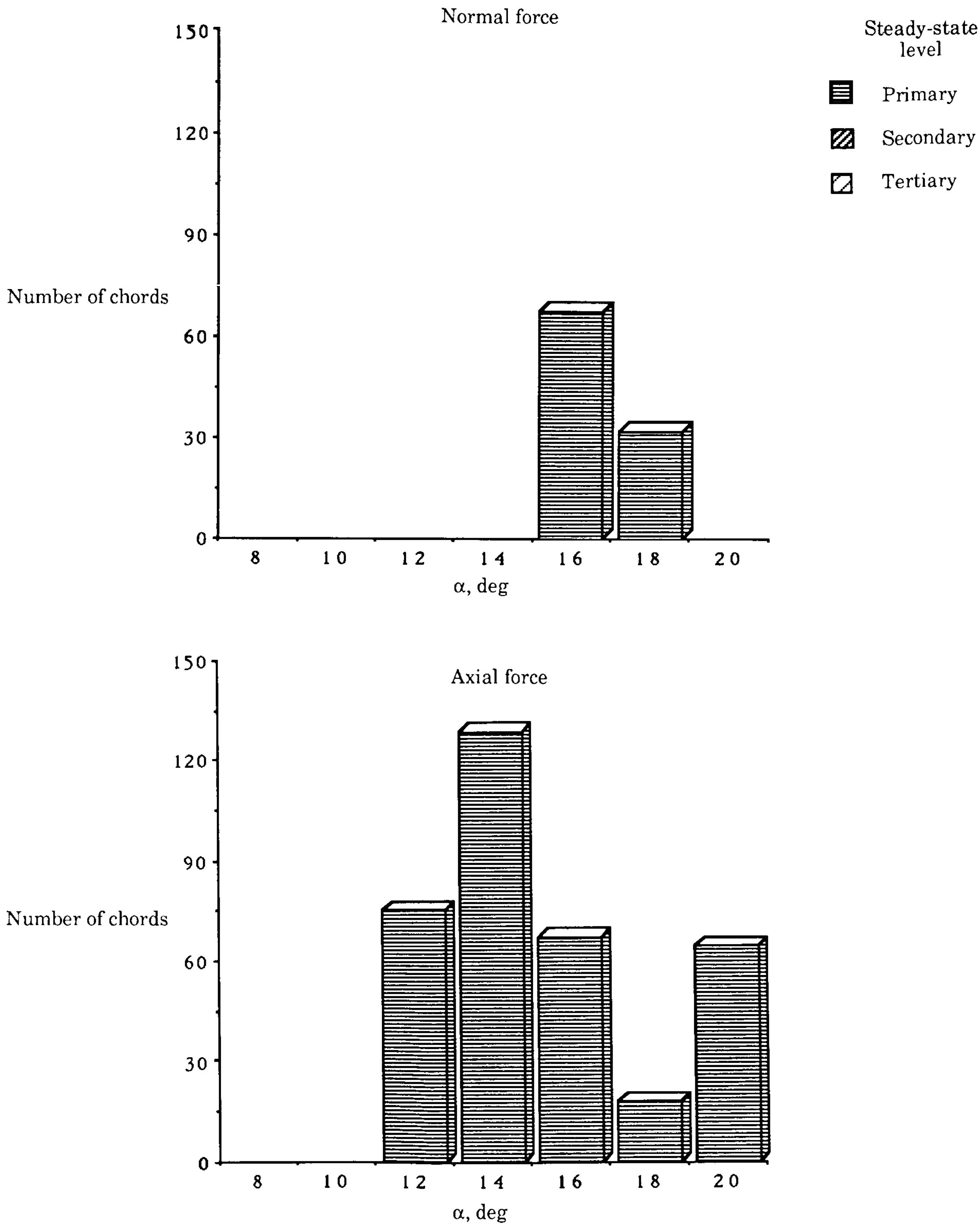

(d) $\delta = 20°$ and LWC = 21 g/m^3.

Figure C1. Continued.

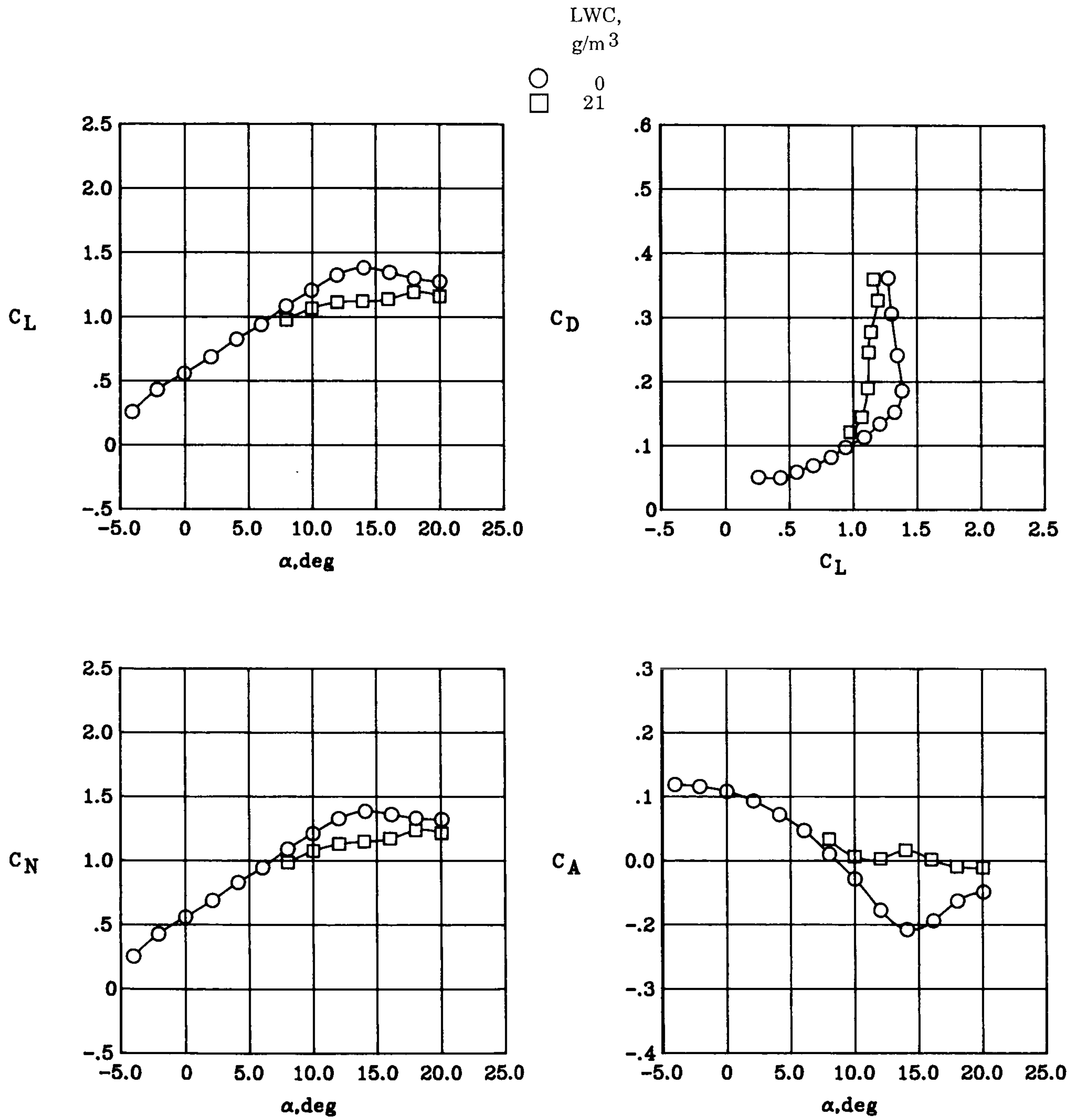

(e) $\delta = 20°$.

Figure C1. Concluded.

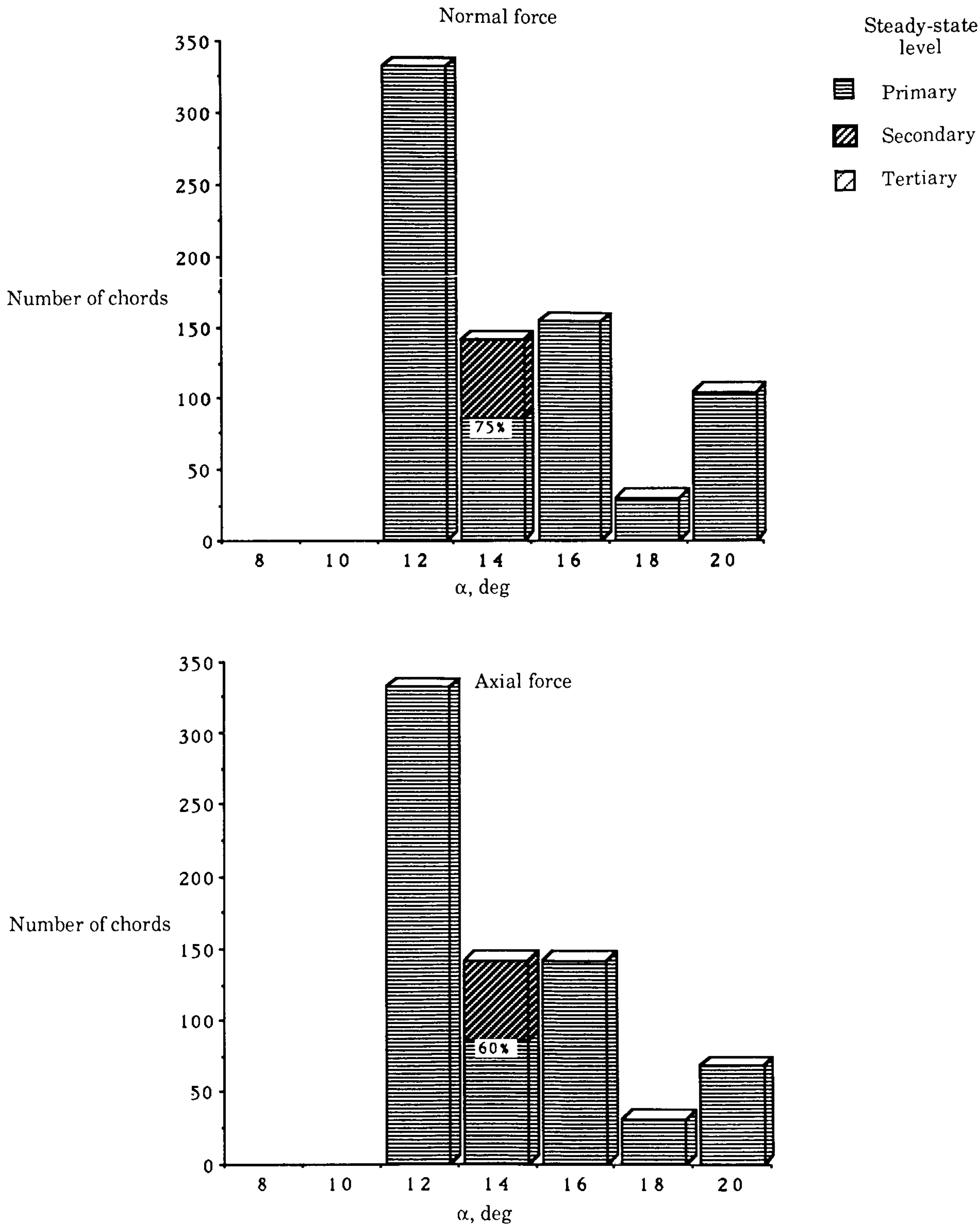

(a) $\delta = 0°$ and LWC = 17 g/m^3.

Figure C2. Dry to wet transition time graphs and steady-state force data for B1N7 nozzles and $q = 30$ psf.

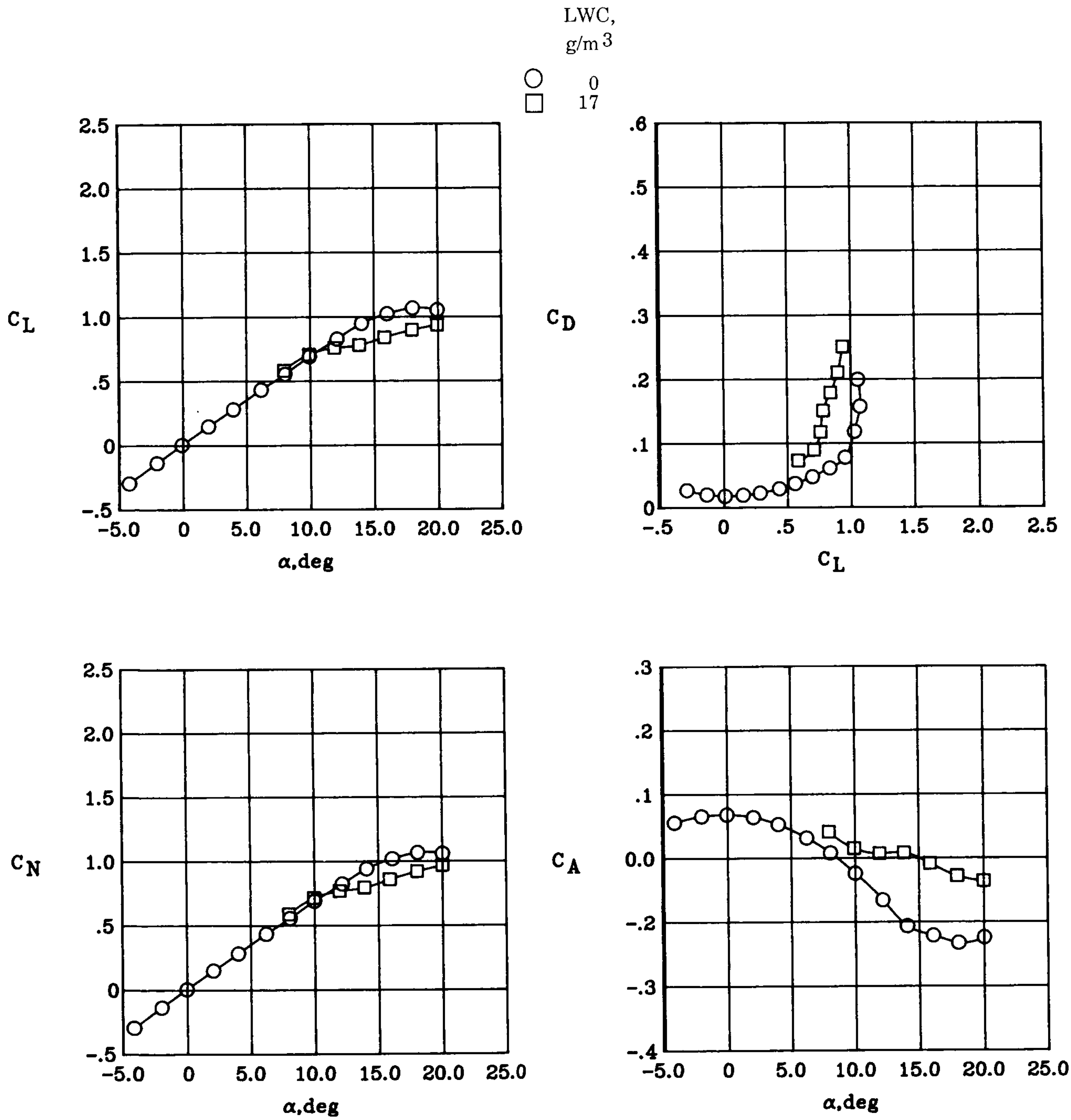

(b) $\delta = 0°$.

Figure C2. Continued.

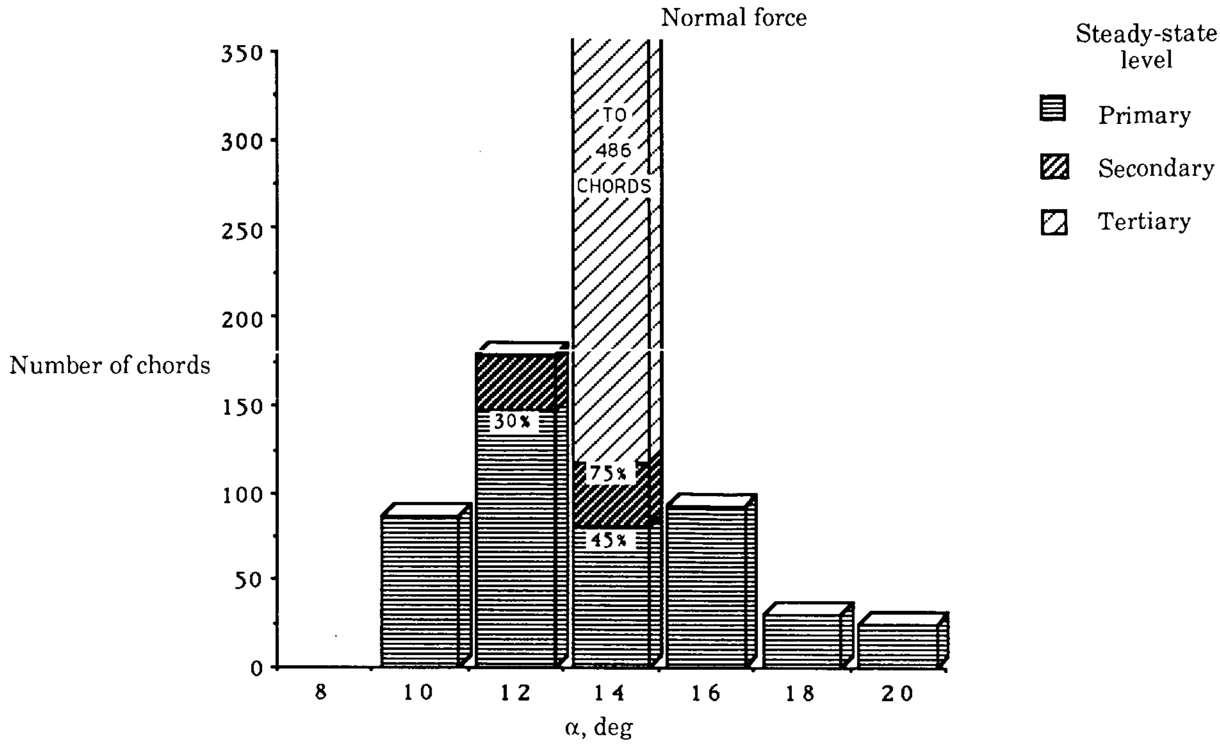

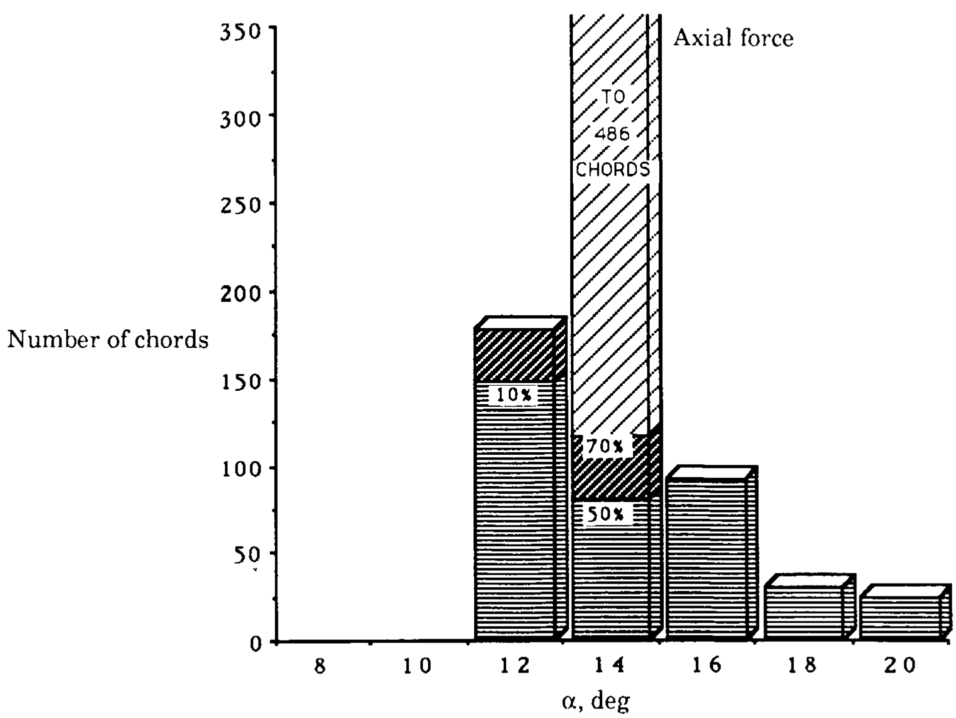

(c) $\delta = 10°$ and LWC = 17 g/m^3.

Figure C2. Continued.

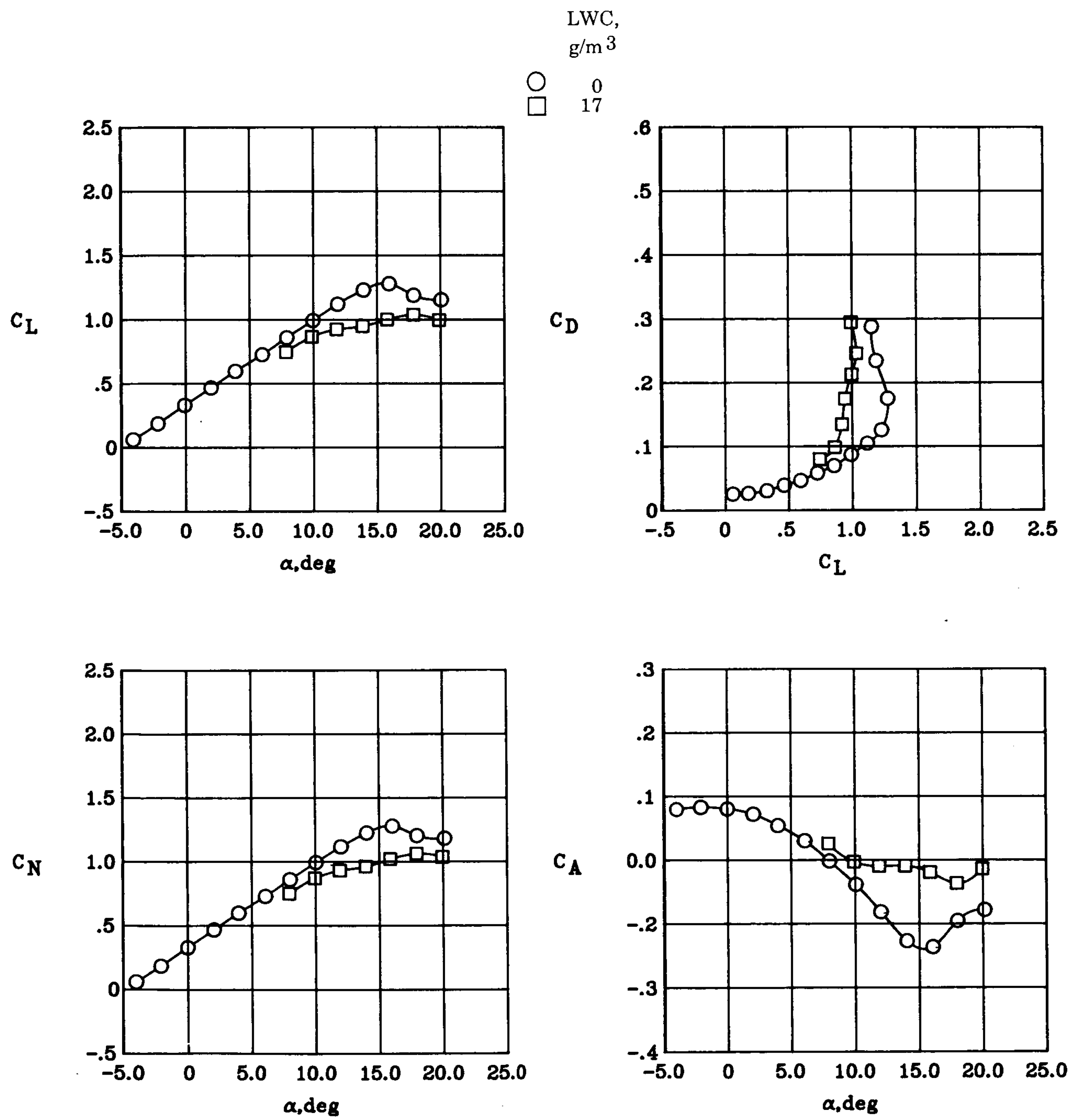

(d) $\delta = 10°$.

Figure C2. Continued.

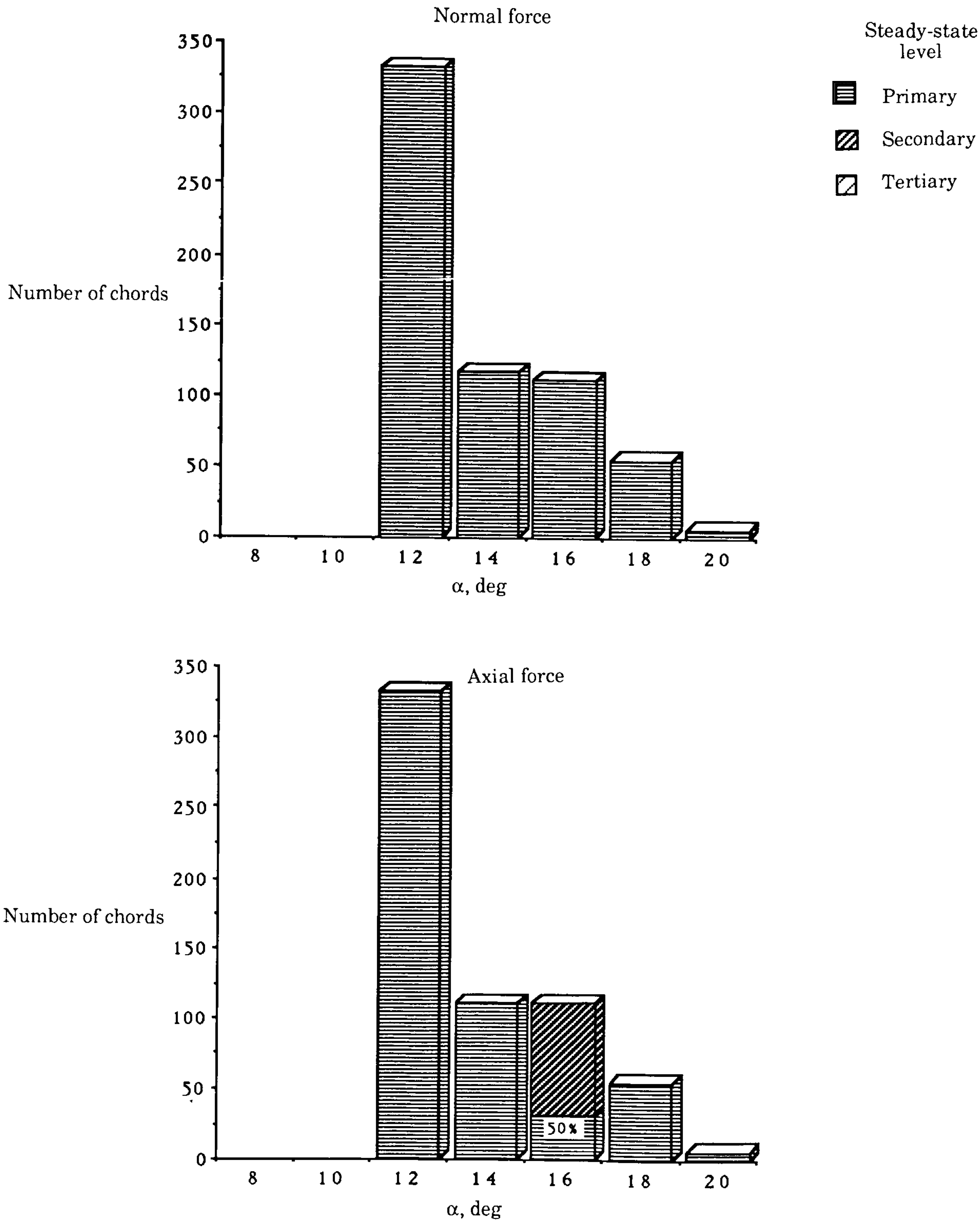

(e) $\delta = 20°$ and LWC = 17 g/m^3.

Figure C2. Continued.

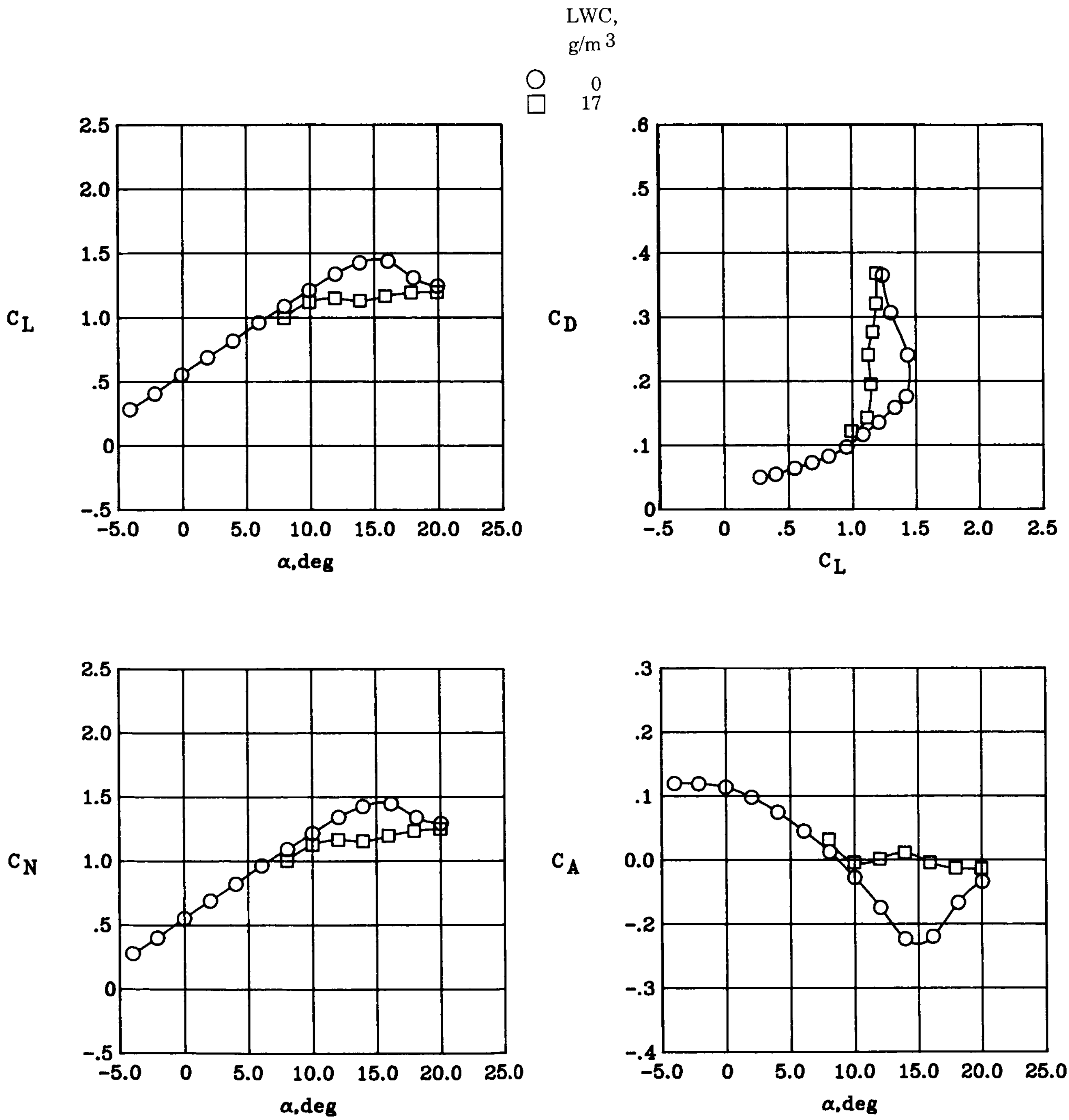

(f) $\delta = 20^{\circ}$.

Figure C2. Concluded.

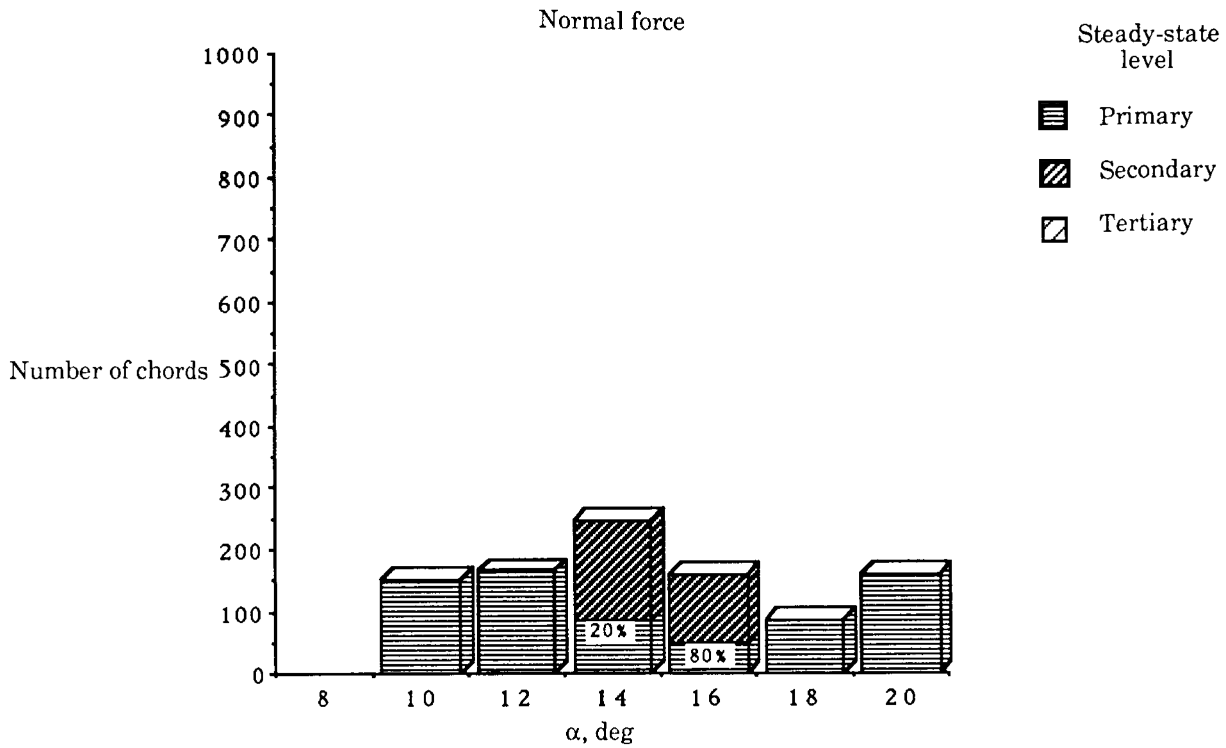

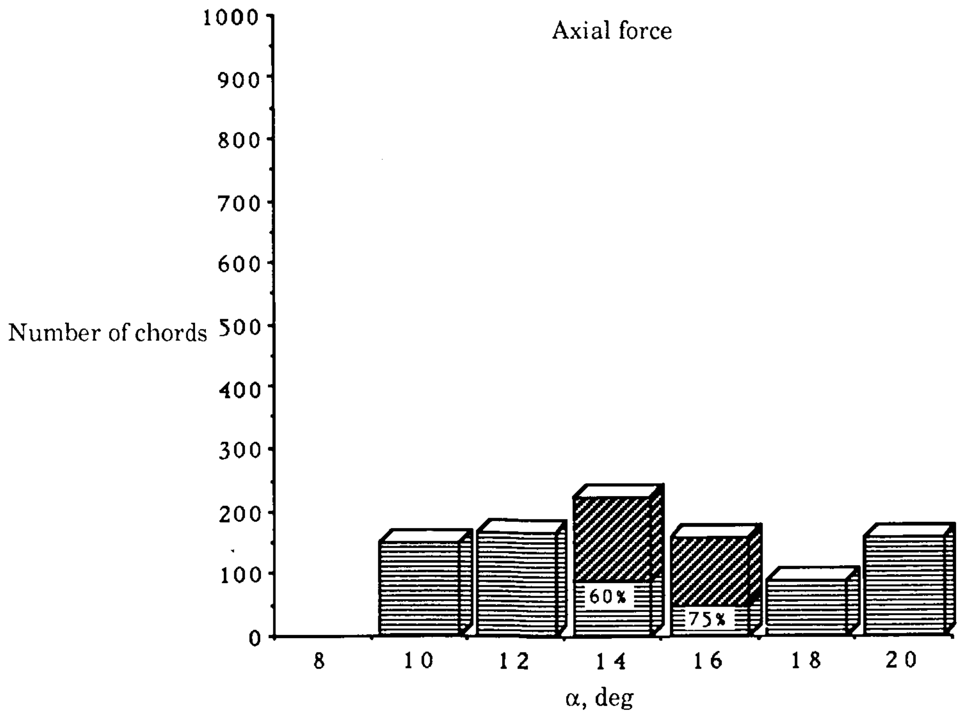

(a) $\delta = 0°$ and LWC = 15 g/m^3.

Figure C3. Dry to wet transition time graphs and steady-state force data for B1N7 nozzles and q = 50 psf.

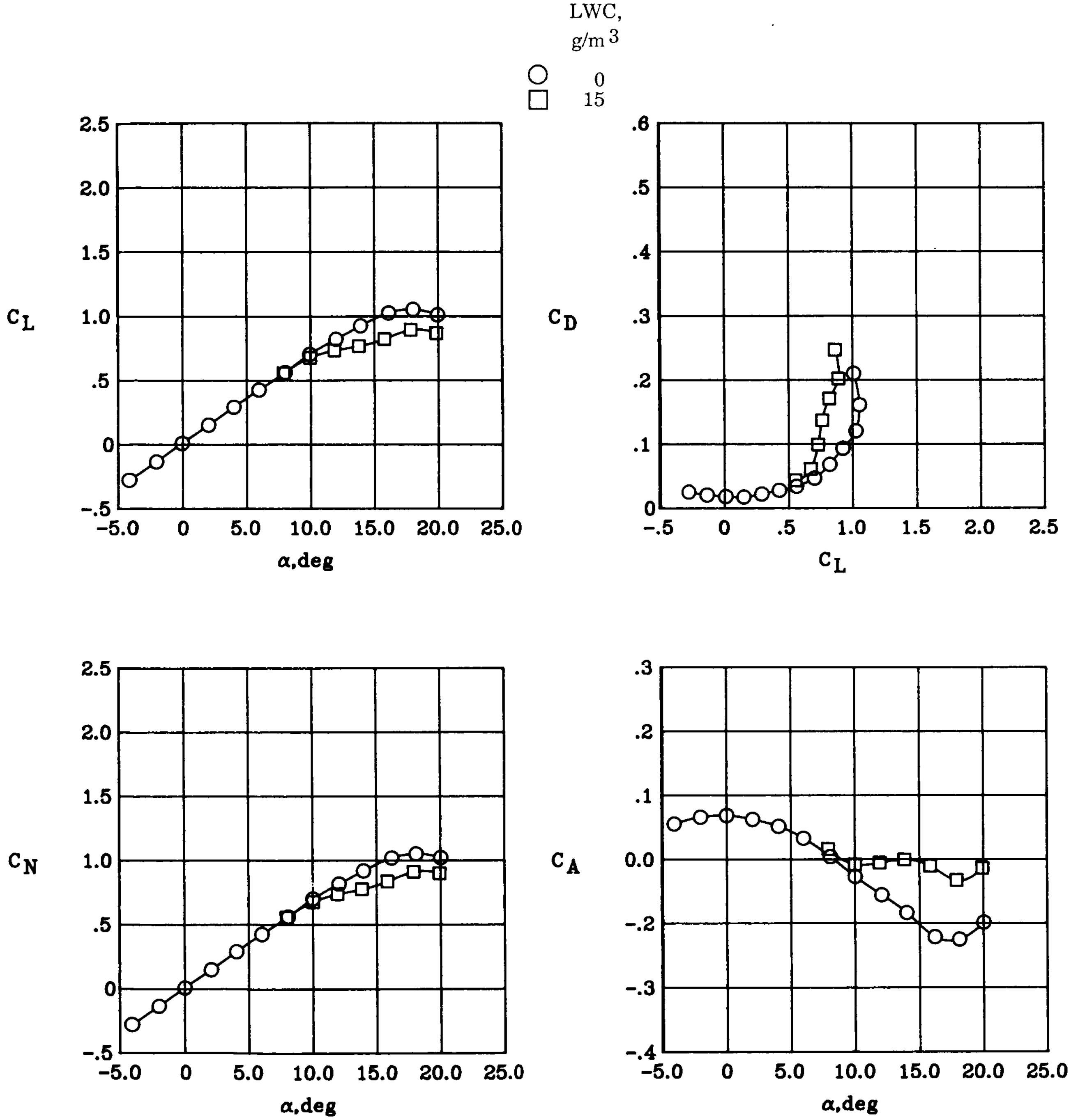

(b) $\delta = 0°$.

Figure C3. Continued.

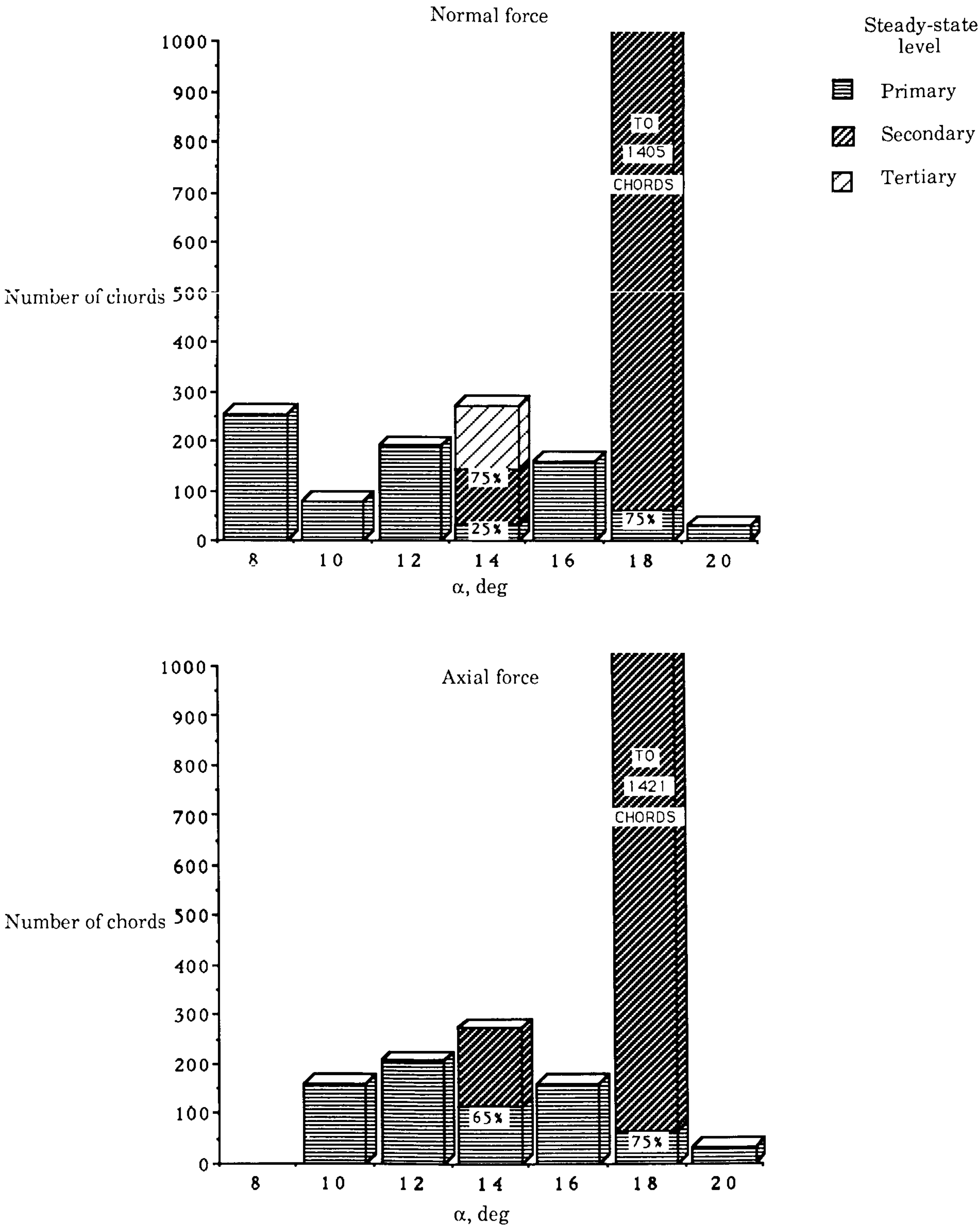

(c) $\delta = 10^\circ$ and LWC = 15 g/m^3.

Figure C3. Continued.

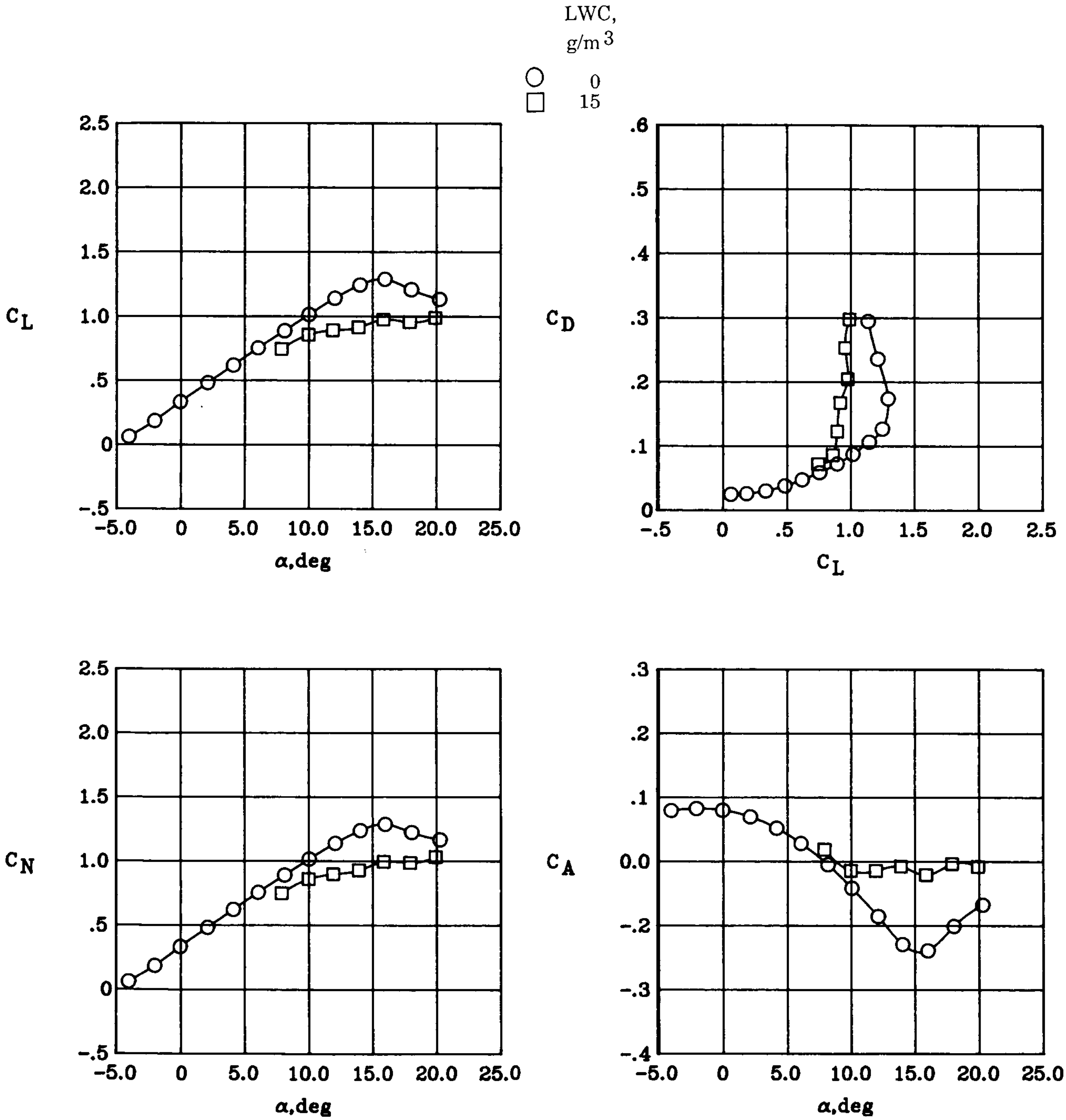

(d) $\delta = 10°$.

Figure C3. Continued.

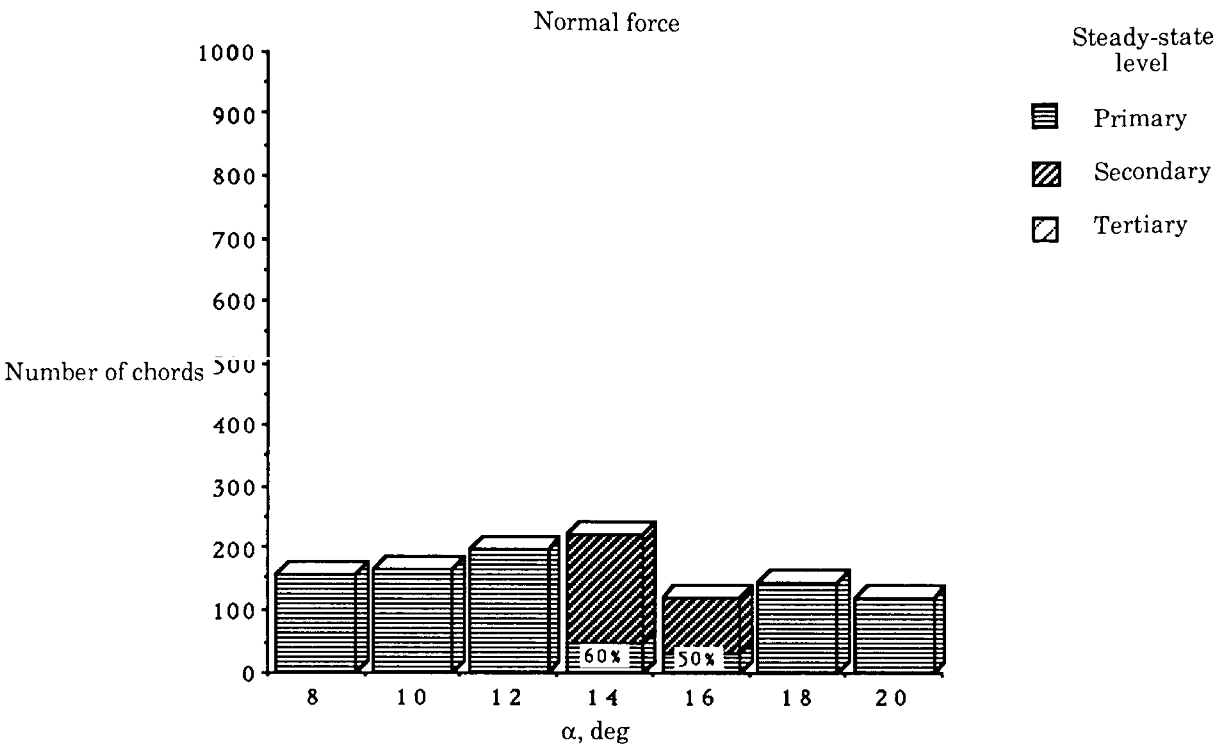

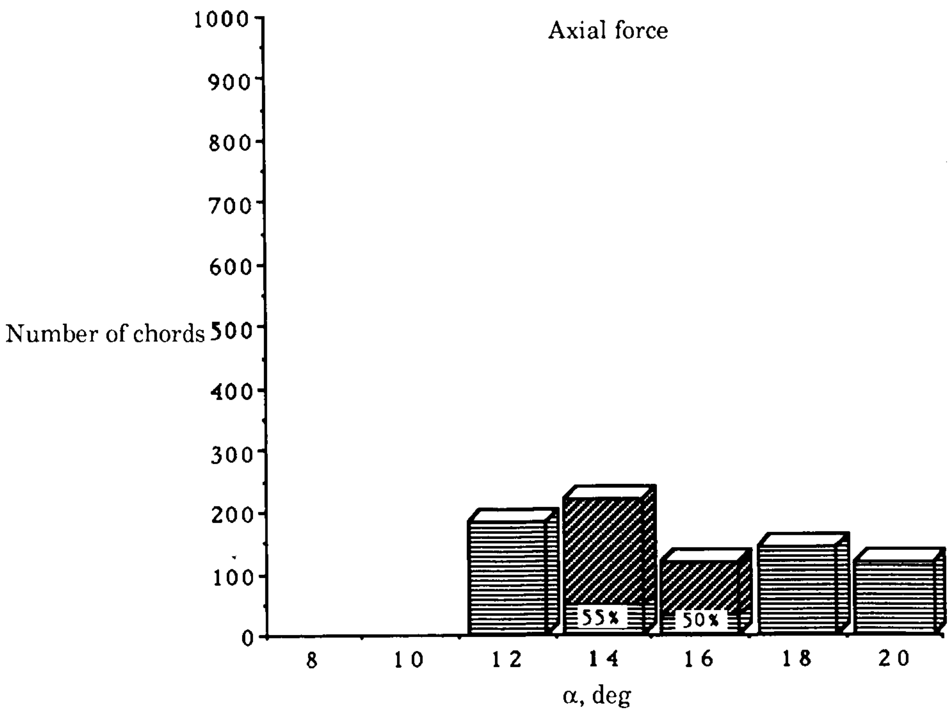

(e) $\delta = 20^{\circ}$ and LWC = 15 g/m^3.

Figure C3. Continued.

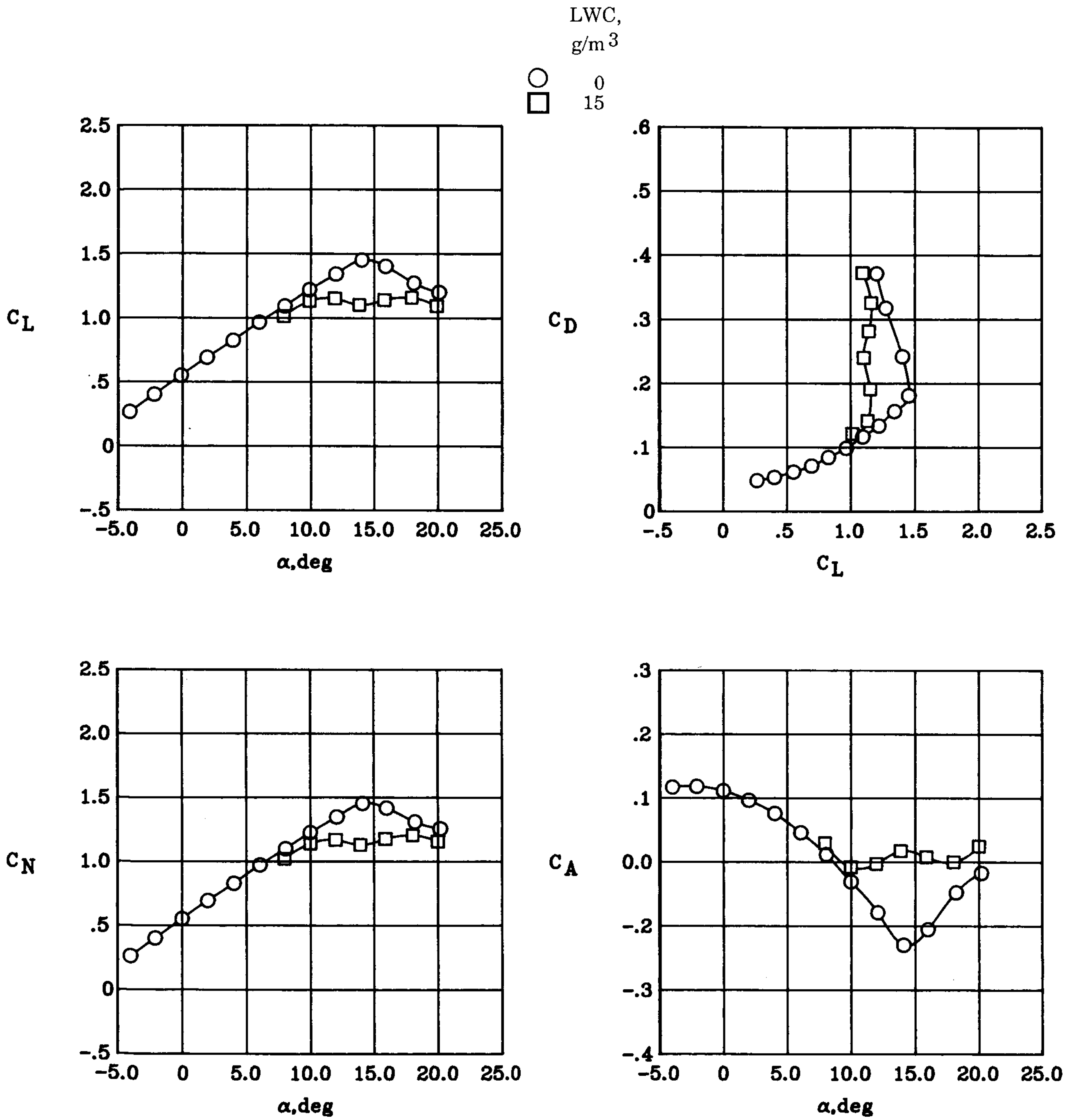

(f) $\delta = 20°$.

Figure C3. Concluded.

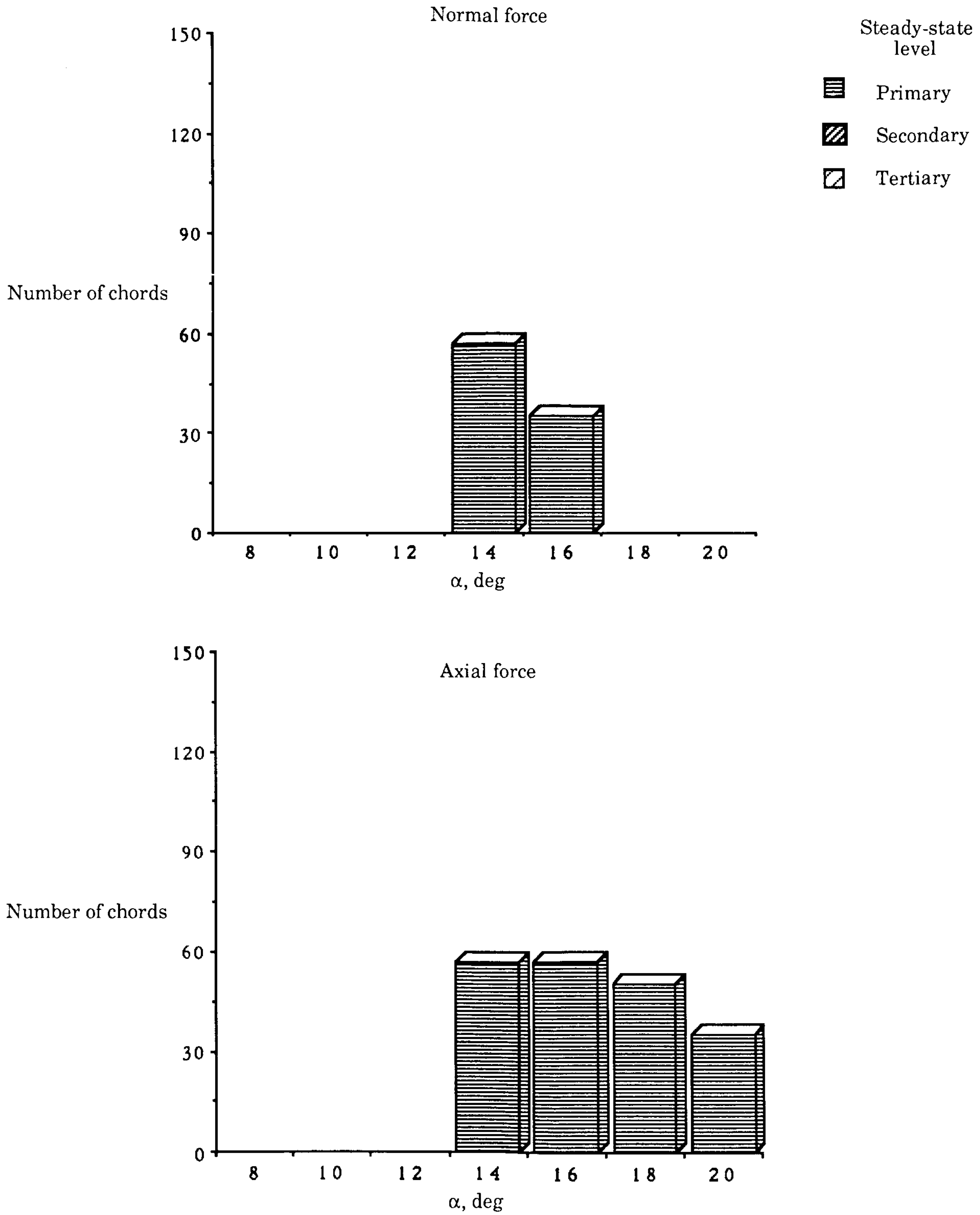

(a) $\delta = 0°$ and LWC = 14 g/m^3.

Figure C4. Dry to wet transition time graphs and steady-state force data for B1N5 nozzles and $q = 10$ psf.

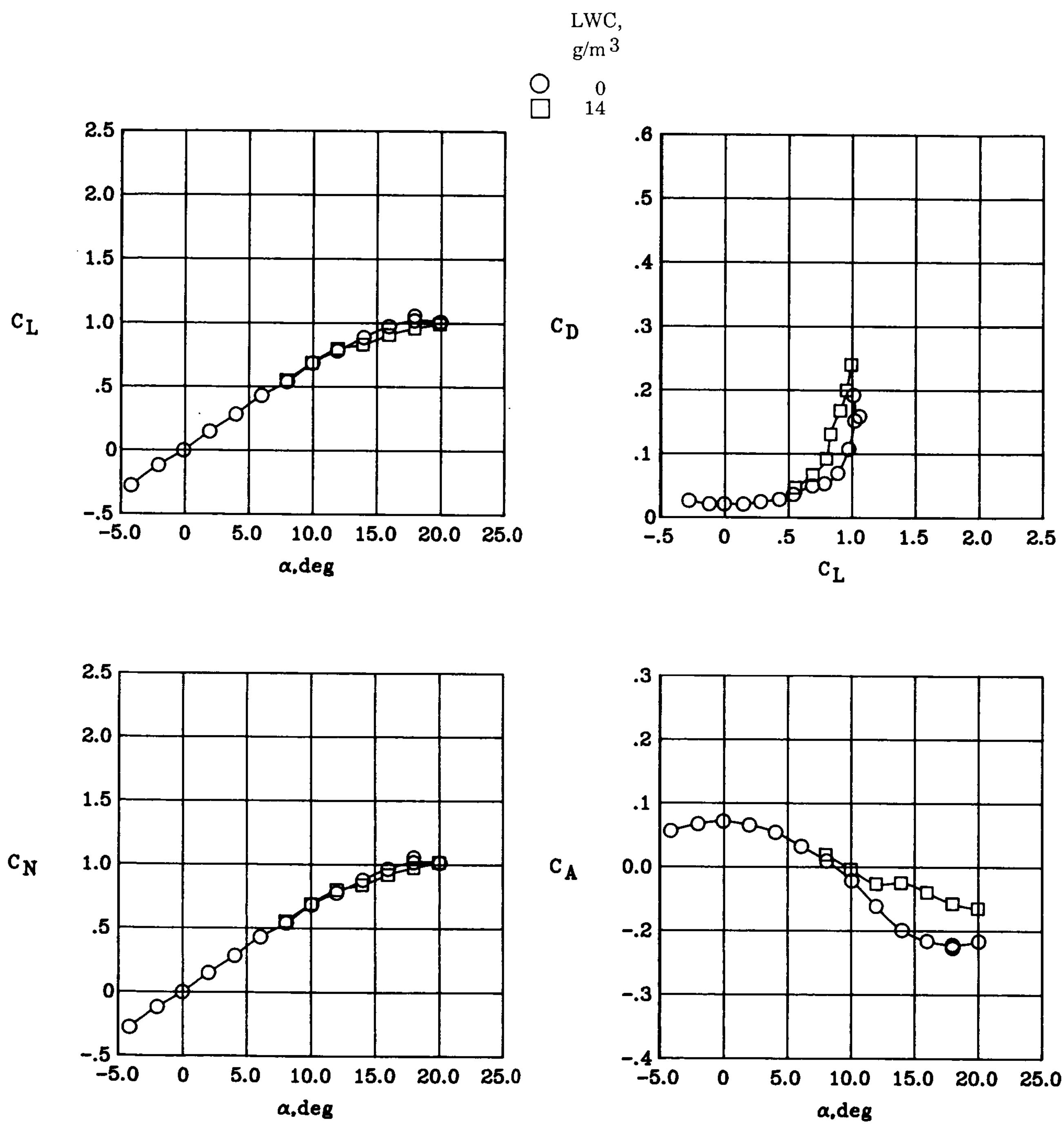

(b) $\delta - 0°$.

Figure C4. Continued.

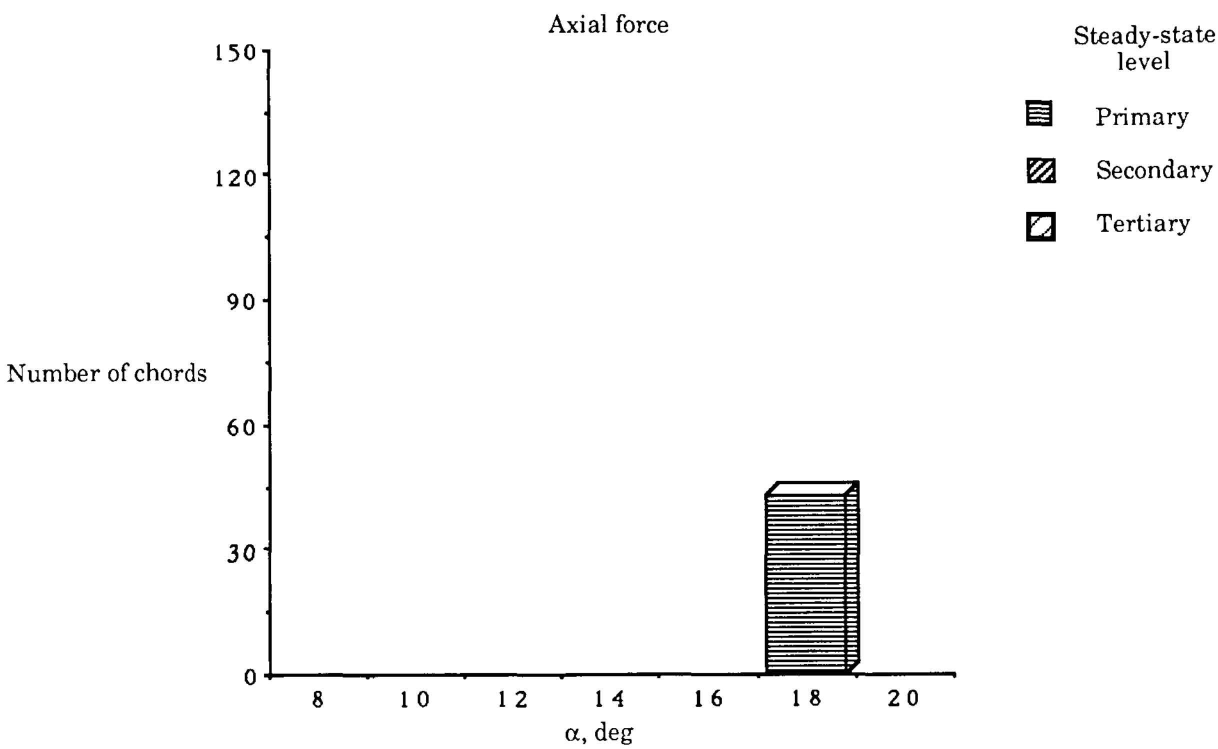

(c) $\delta = 10°$ and LWC = 14 g/m^3.

Figure C4. Continued.

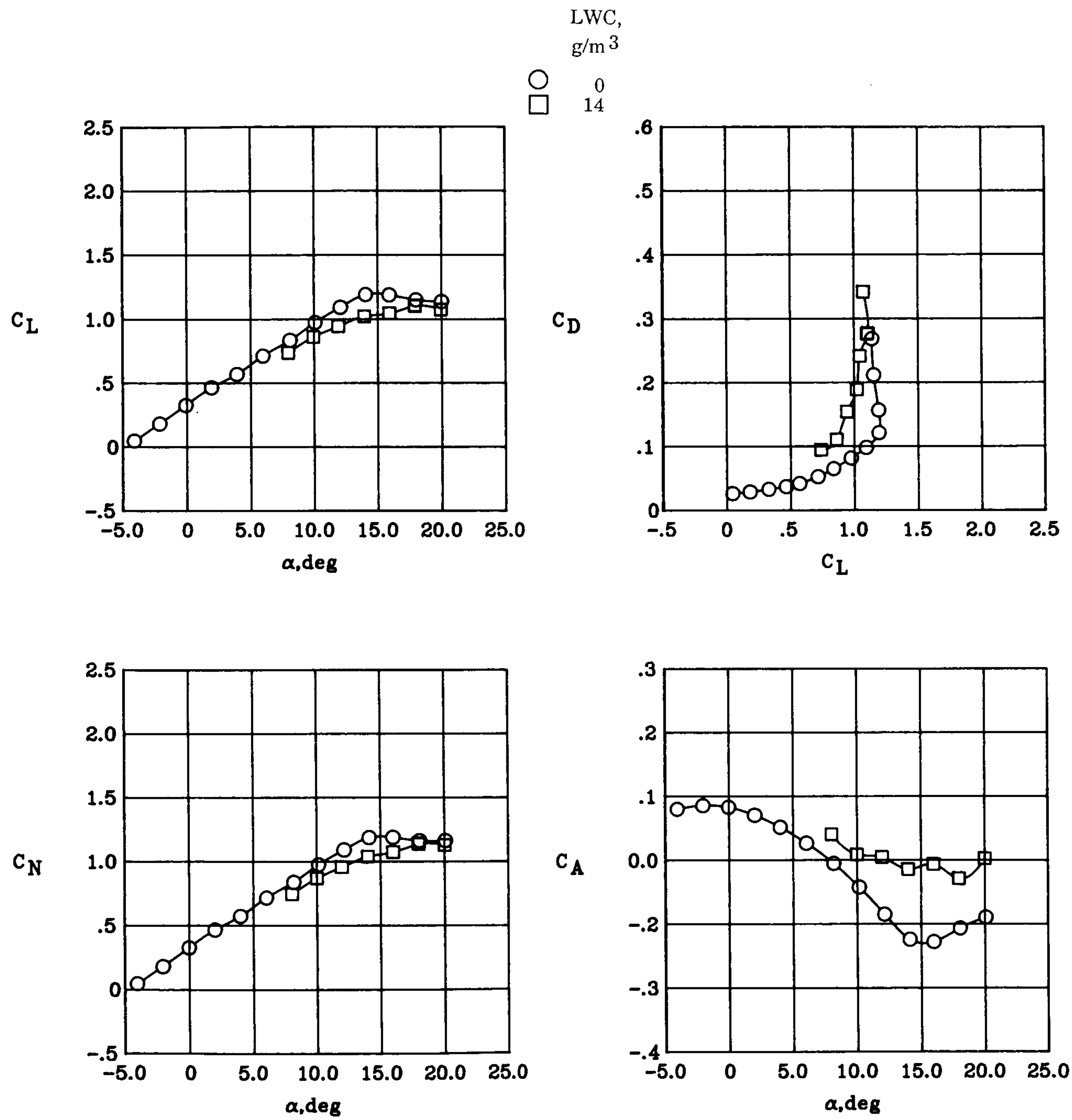

(d) $\delta = 10°$.

Figure C4. Continued.

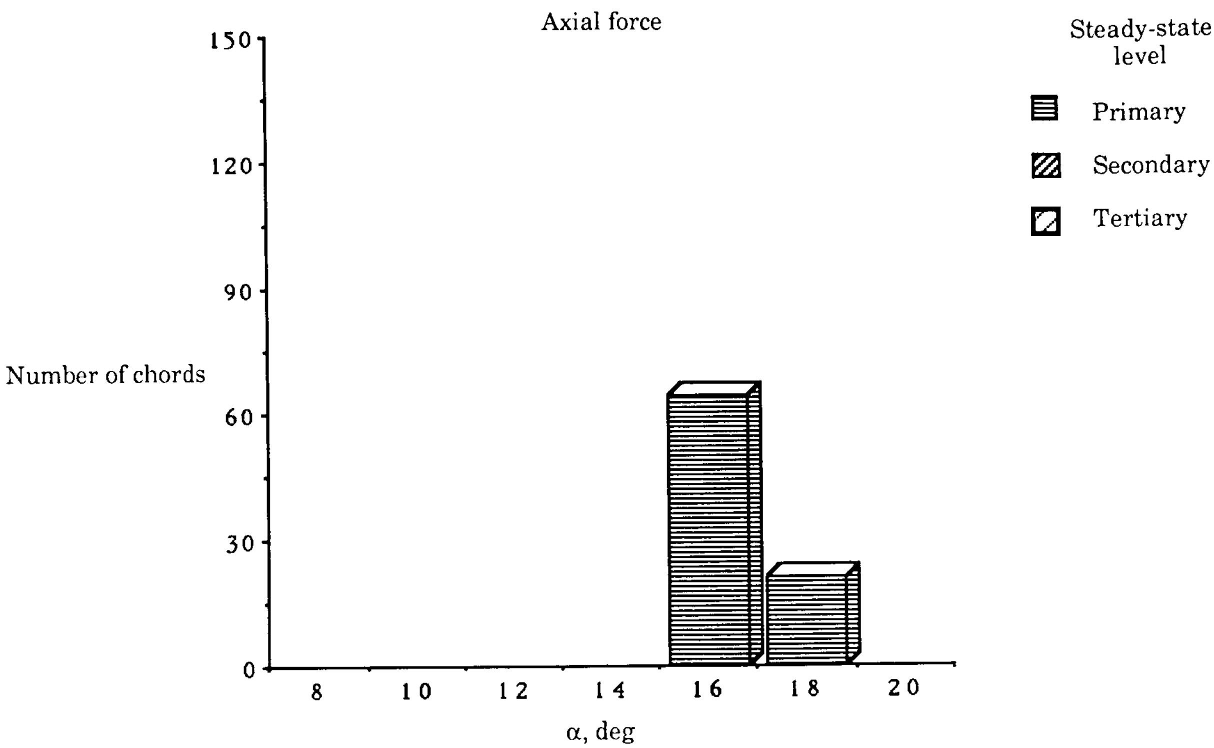

(e) $\delta = 20^\circ$ and LWC = 14 g/m^3.

Figure C4. Continued.

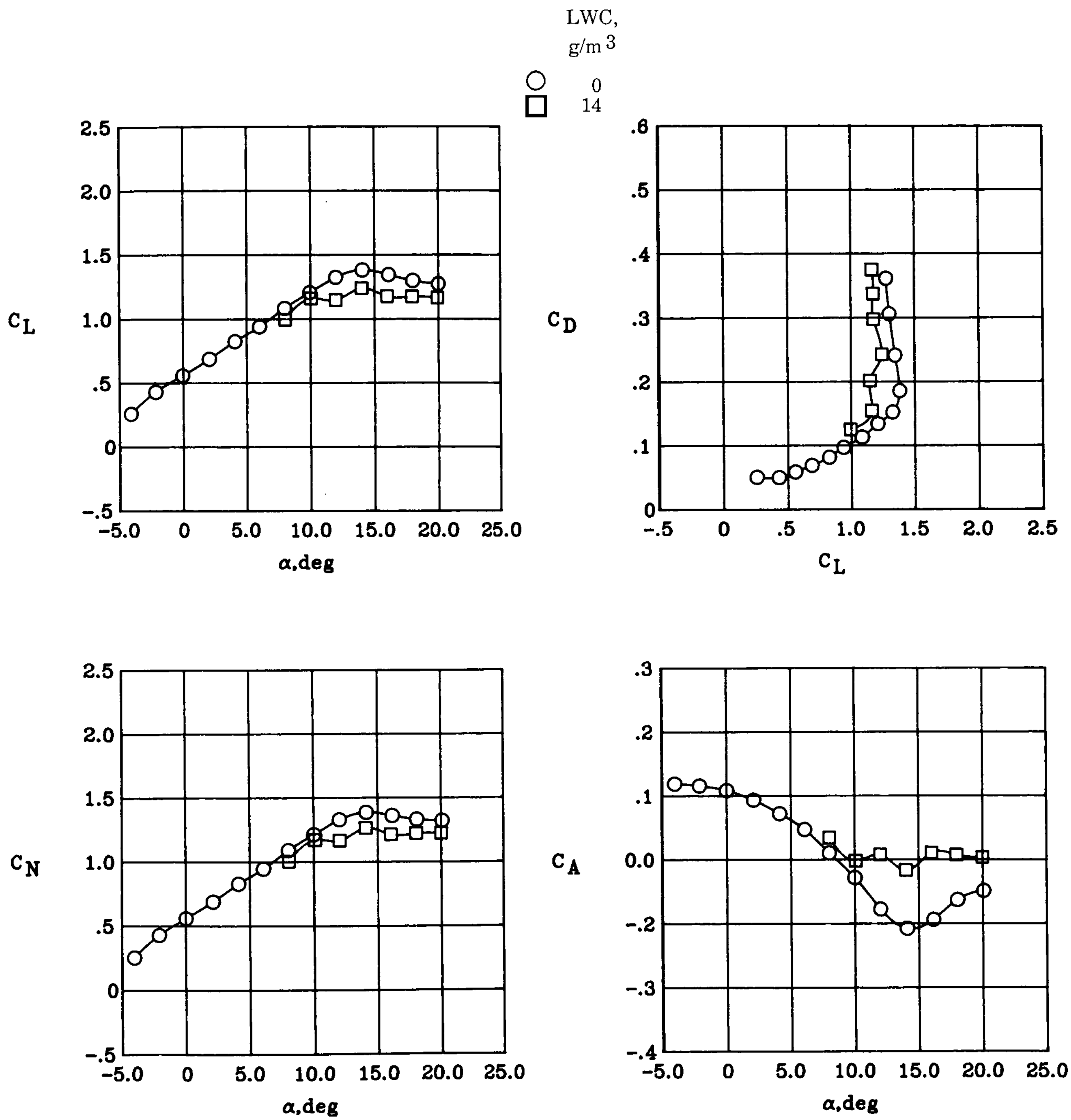

(f) $\delta = 20°$.

Figure C4. Concluded.

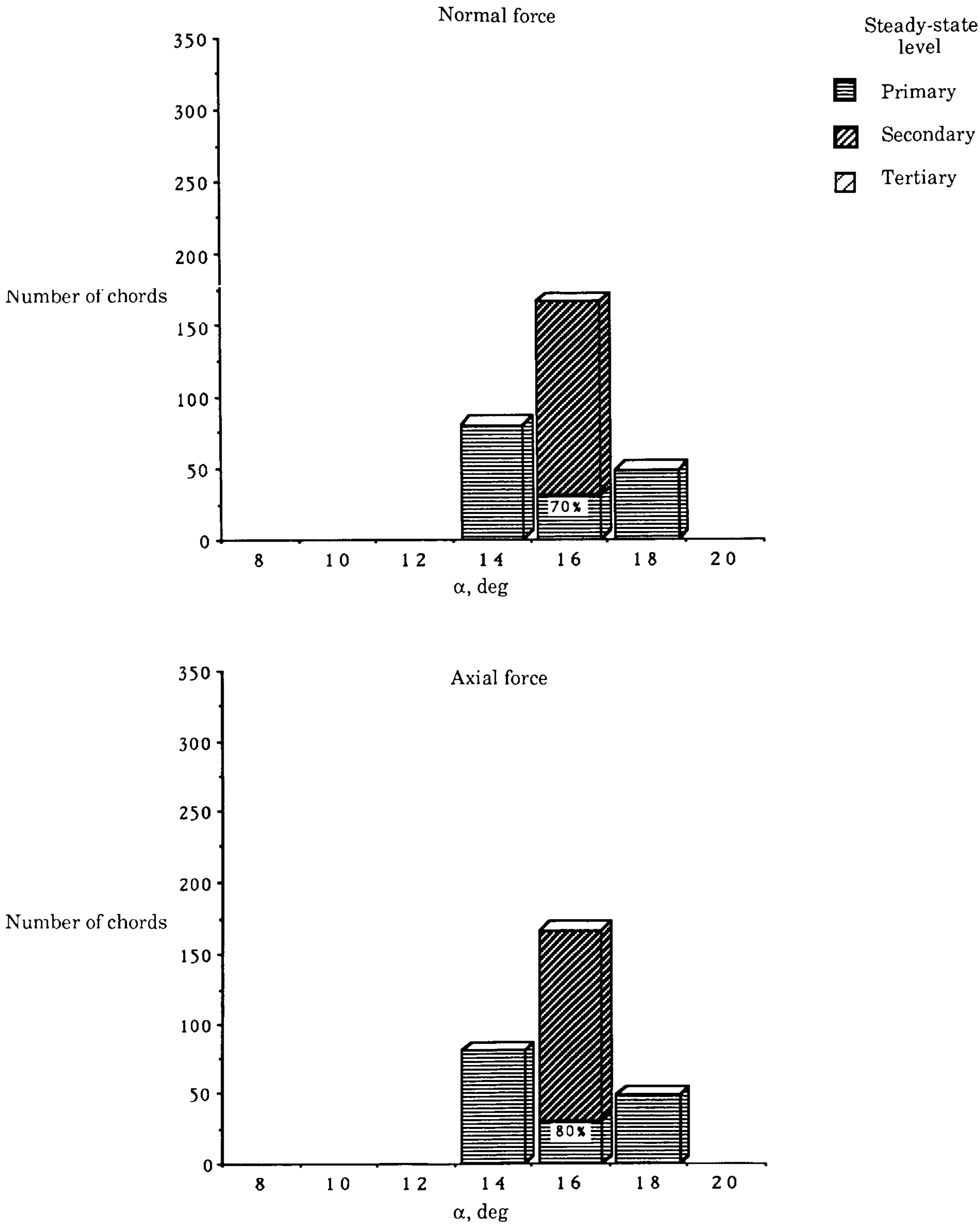

(a) $\delta = 0°$ and LWC = 12 g/m^3.

Figure C5. Dry to wet transition time graphs and steady-state force data for B1N5 nozzles and q = 30 psf.

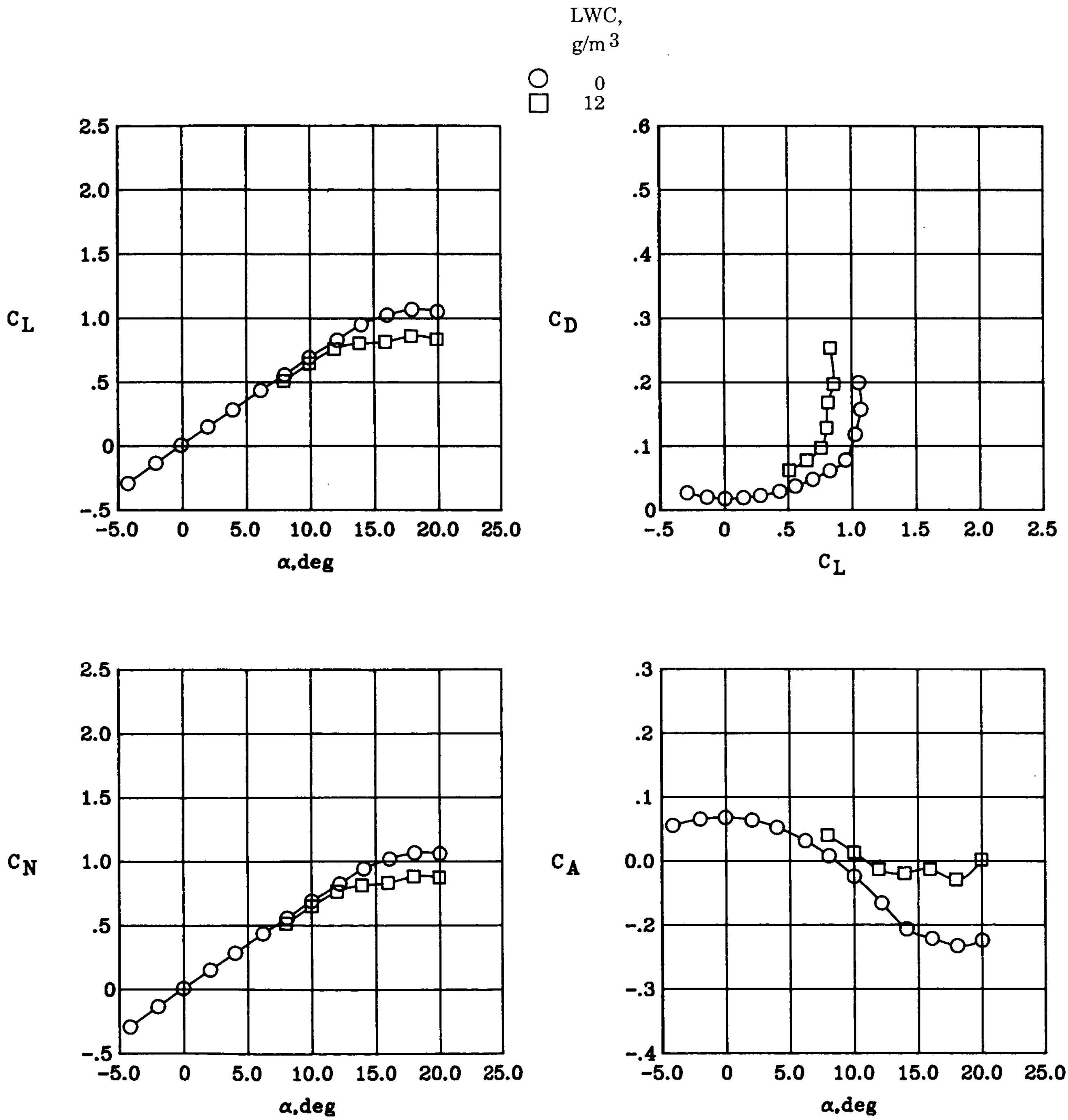

(b) $\delta = 0°$.

Figure C5. Continued.

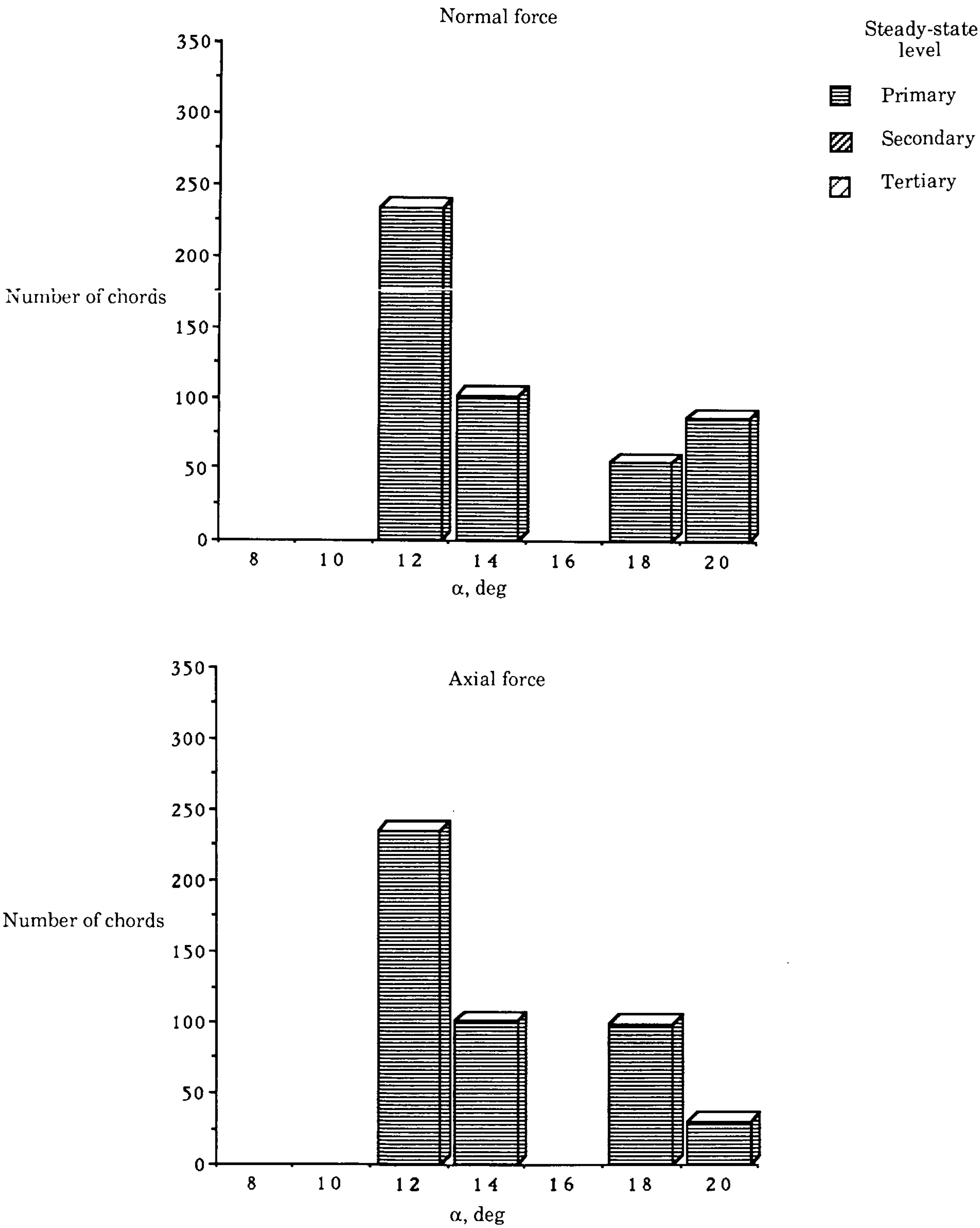

(c) $\delta = 10°$ and LWC = 12 g/m^3.

Figure C5. Continued.

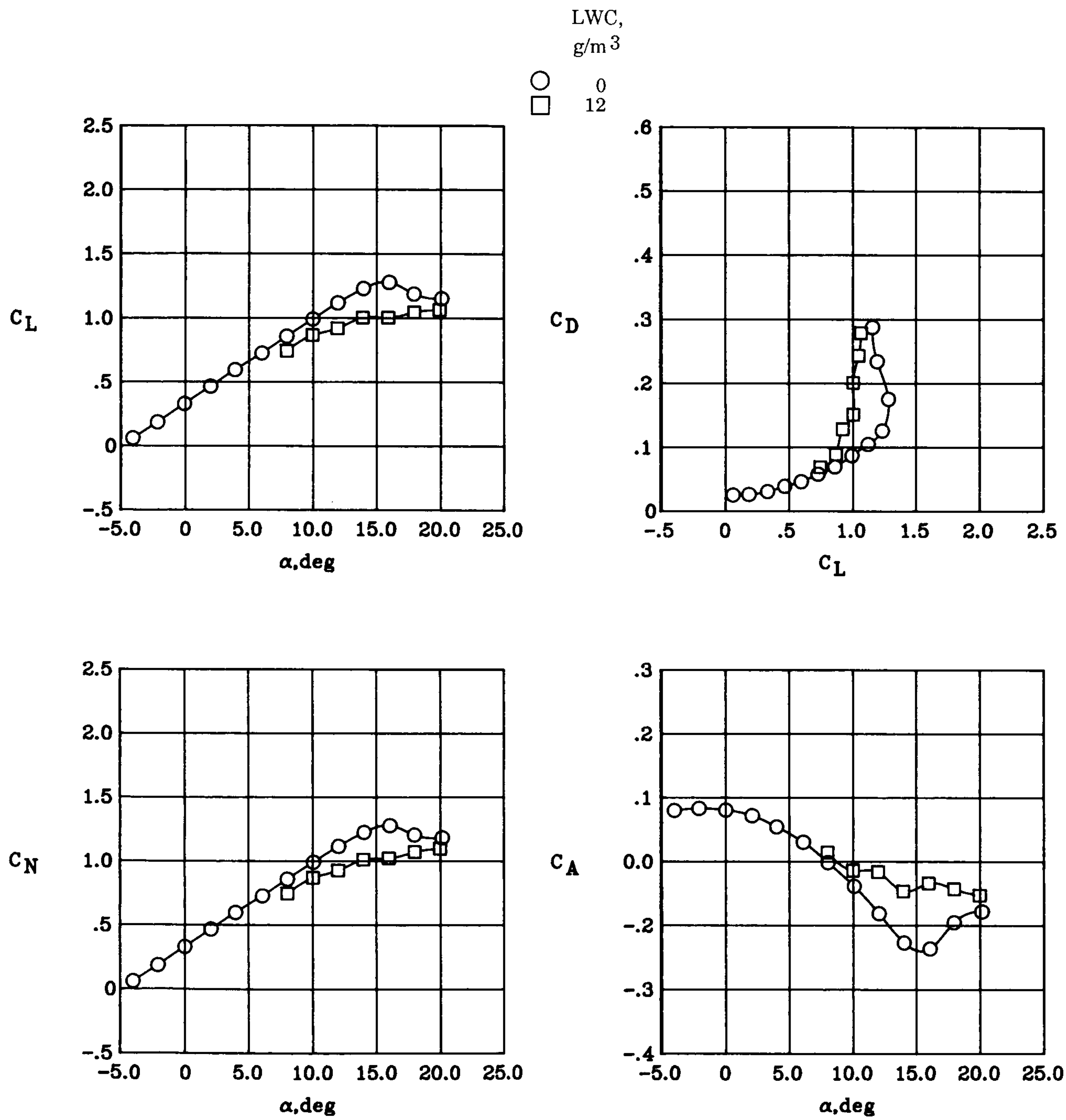

(d) $\delta = 10°$.

Figure C5. Continued.

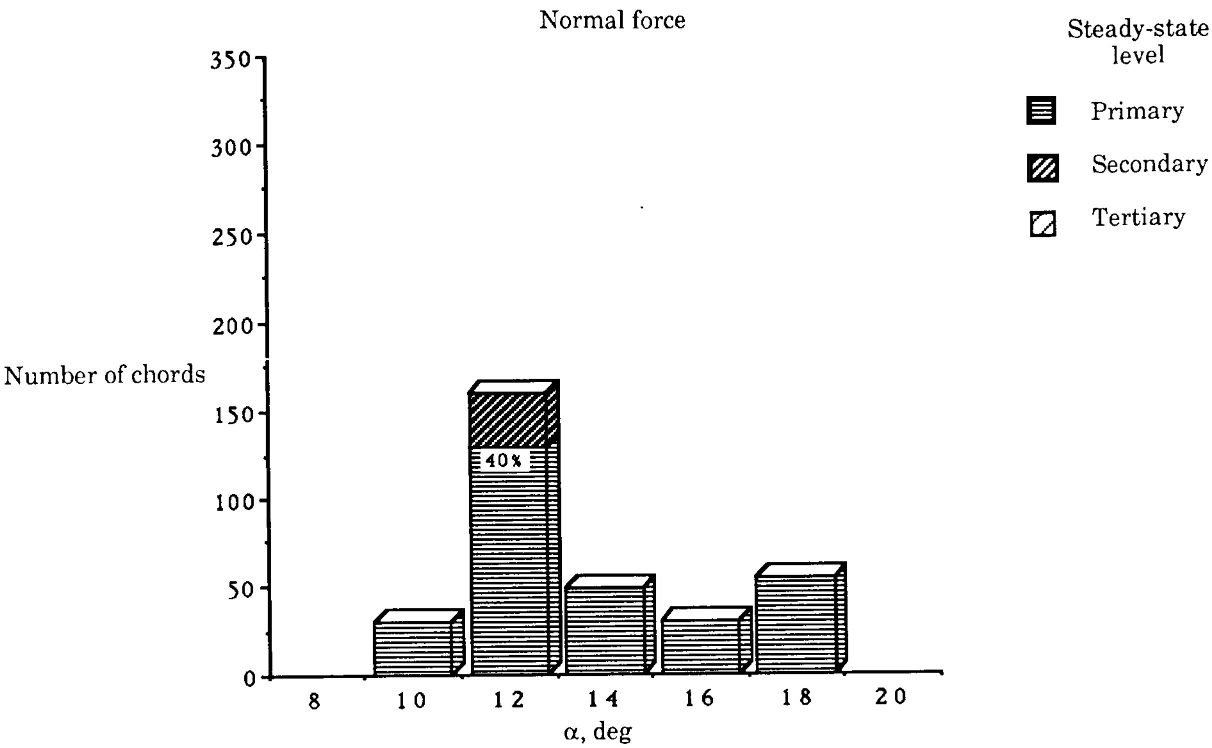

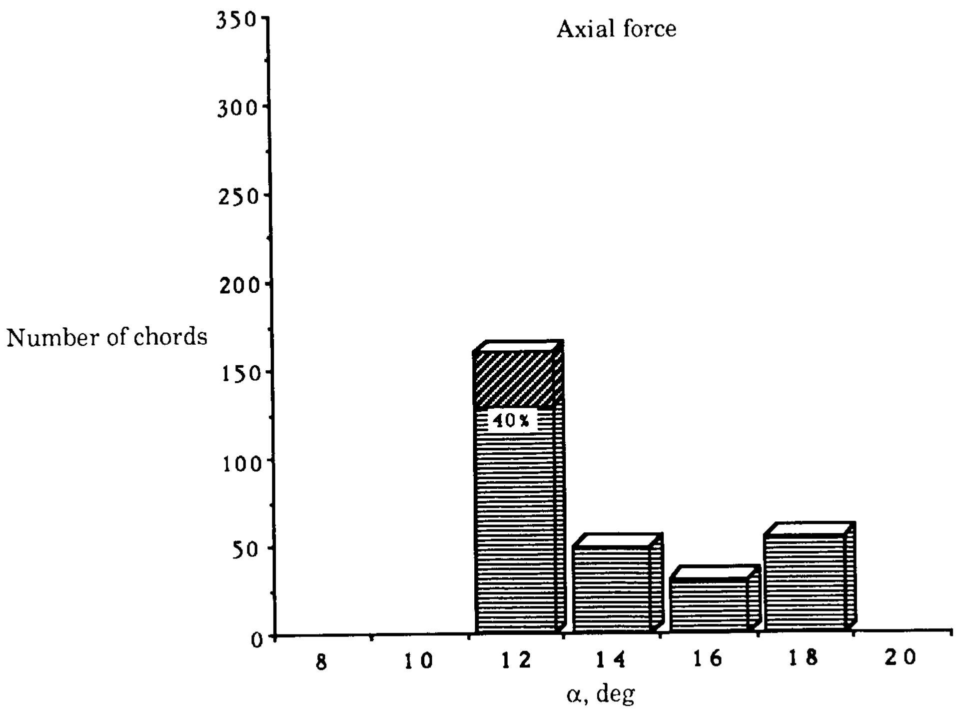

(e) $\delta = 20°$ and LWC = 12 g/m^3.

Figure C5. Continued.

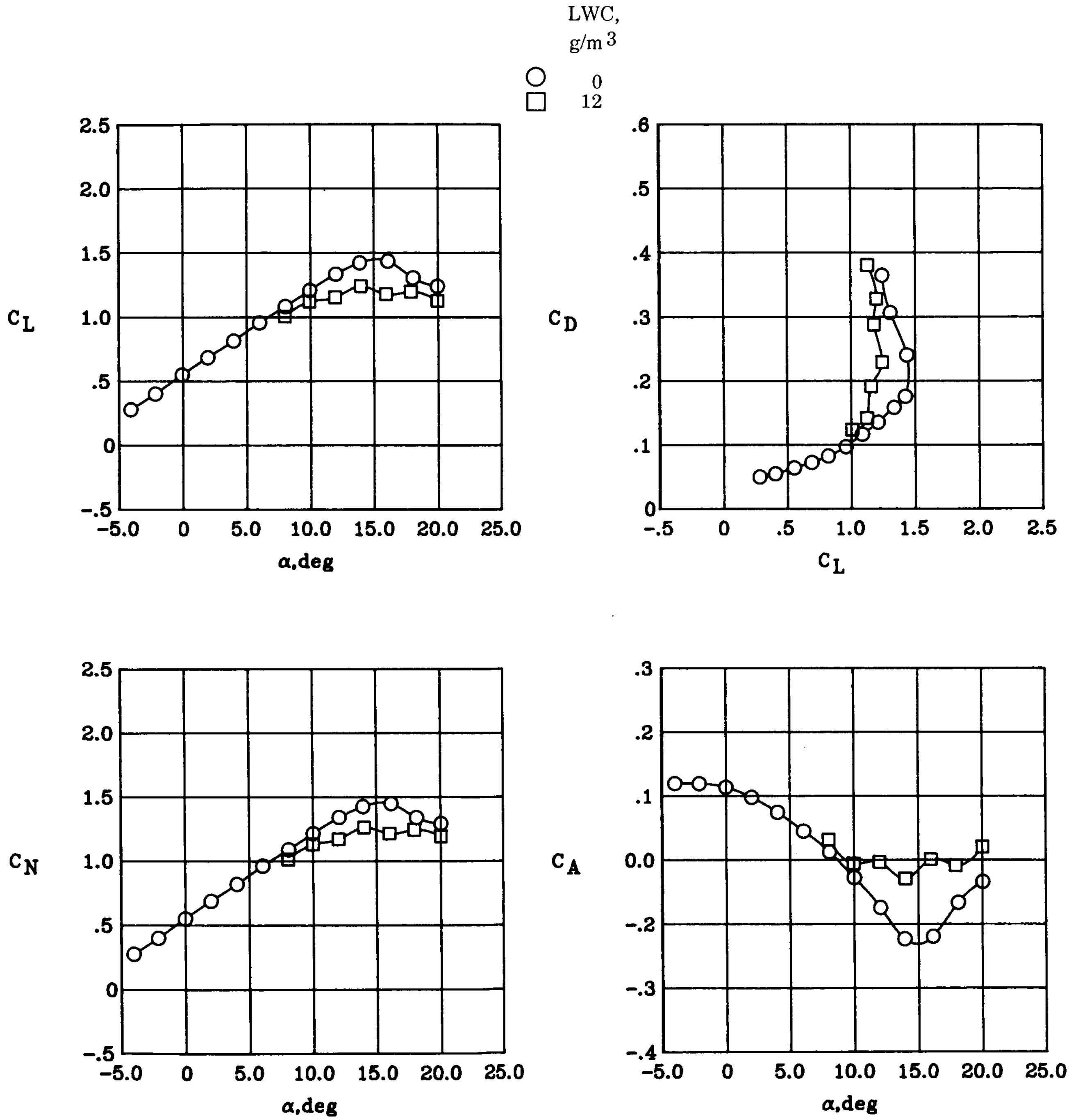

(f) $\delta = 20°$.

Figure C5. Concluded.

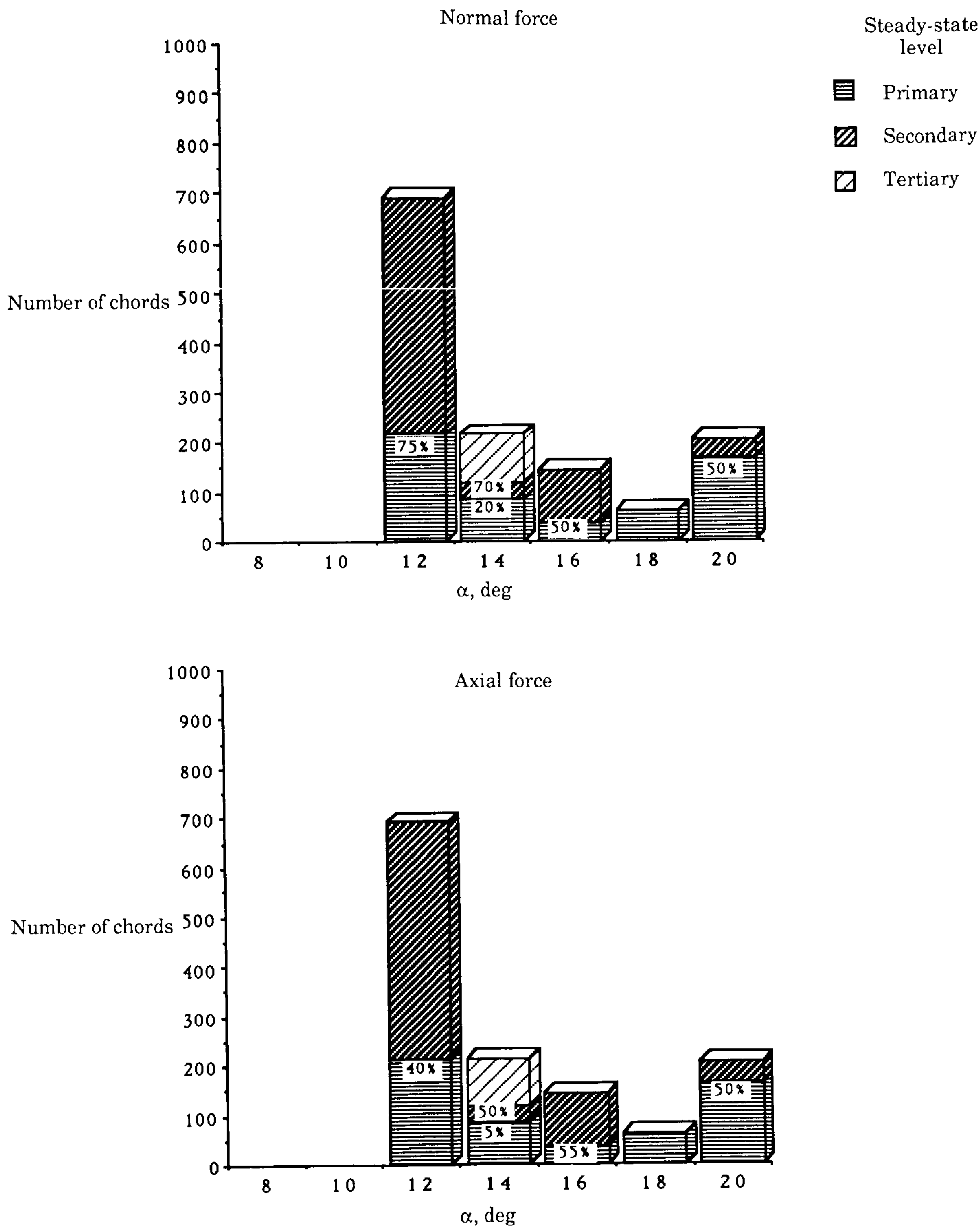

(a) $\delta = 0°$ and LWC = 10 g/m^3.

Figure C6. Dry to wet transition time graphs and steady-state force data for B1N5 nozzles and $q = 50$ psf.

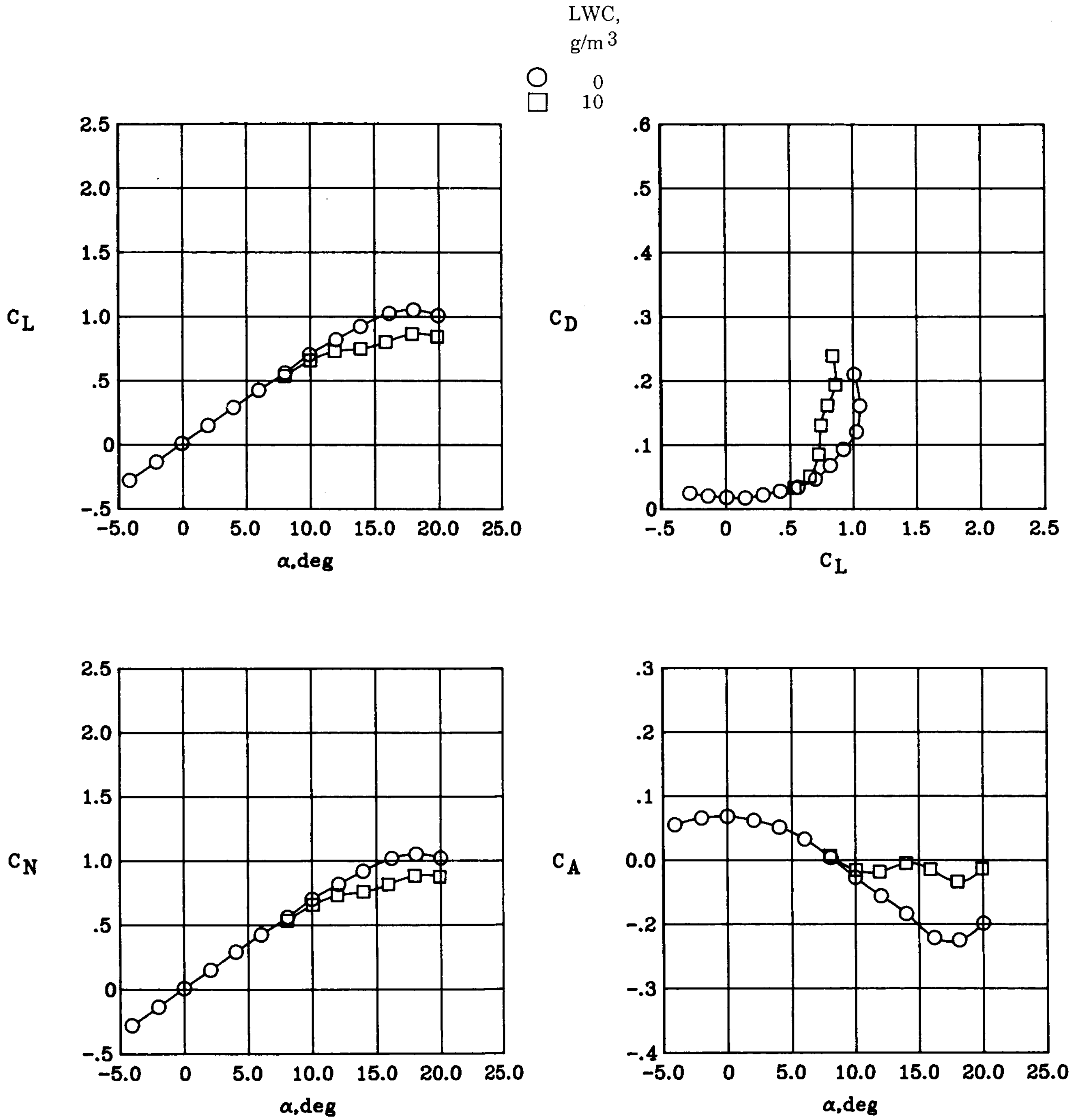

(b) $\delta = 0°$.

Figure C6. Continued.

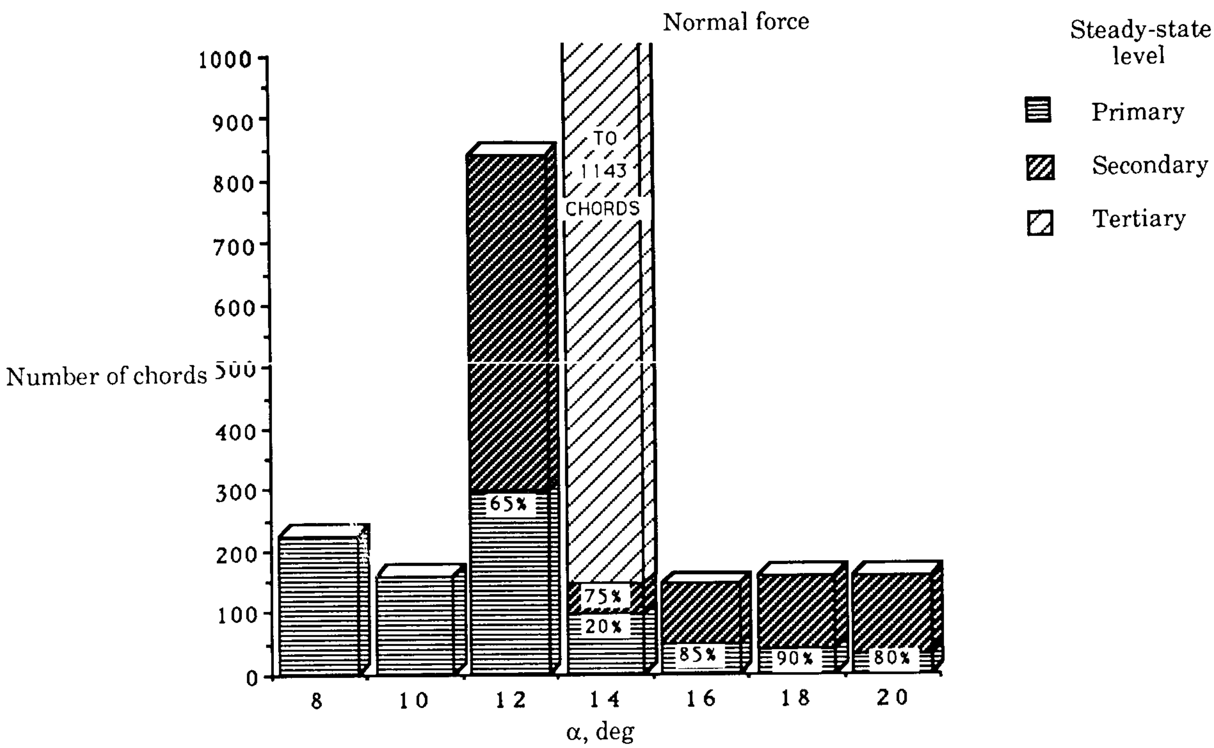

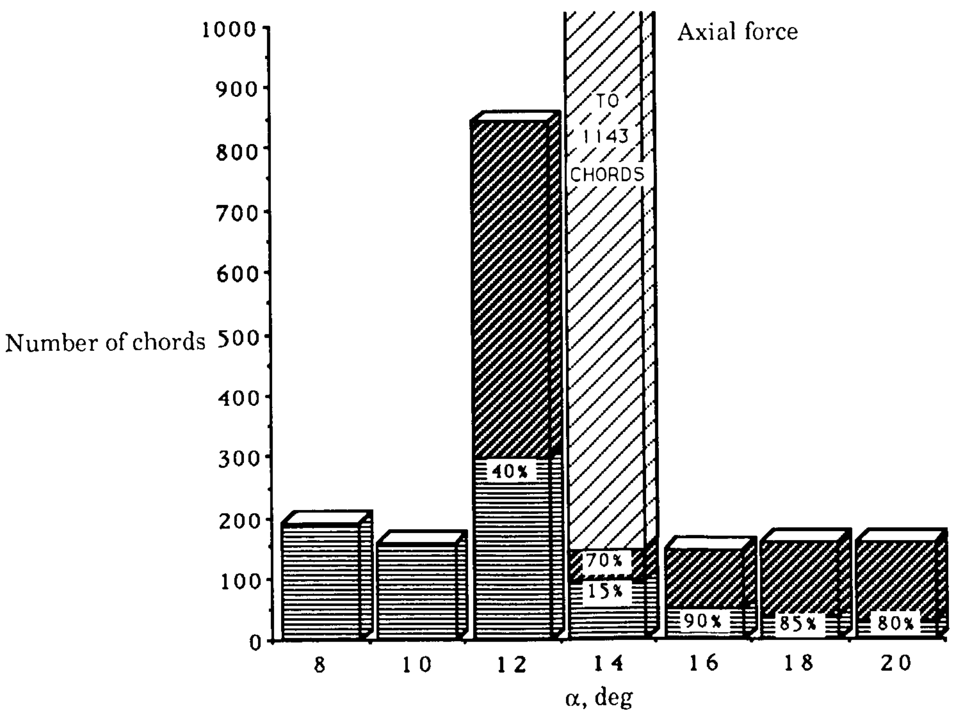

(c) $\delta = 10°$ and LWC = 10 g/m^3.

Figure C6. Continued.

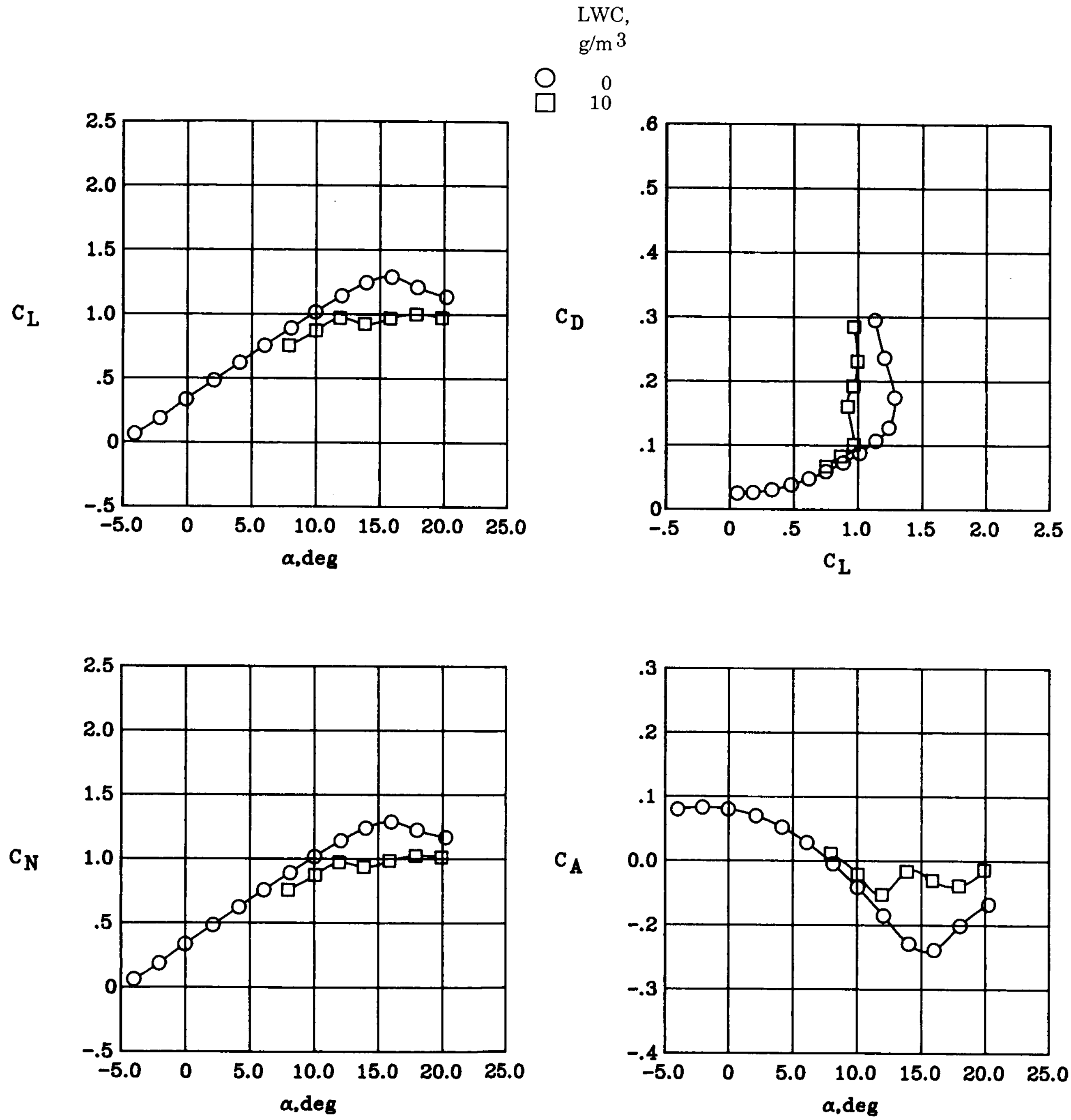

(d) $\delta = 10^\circ$.

Figure C6. Continued.

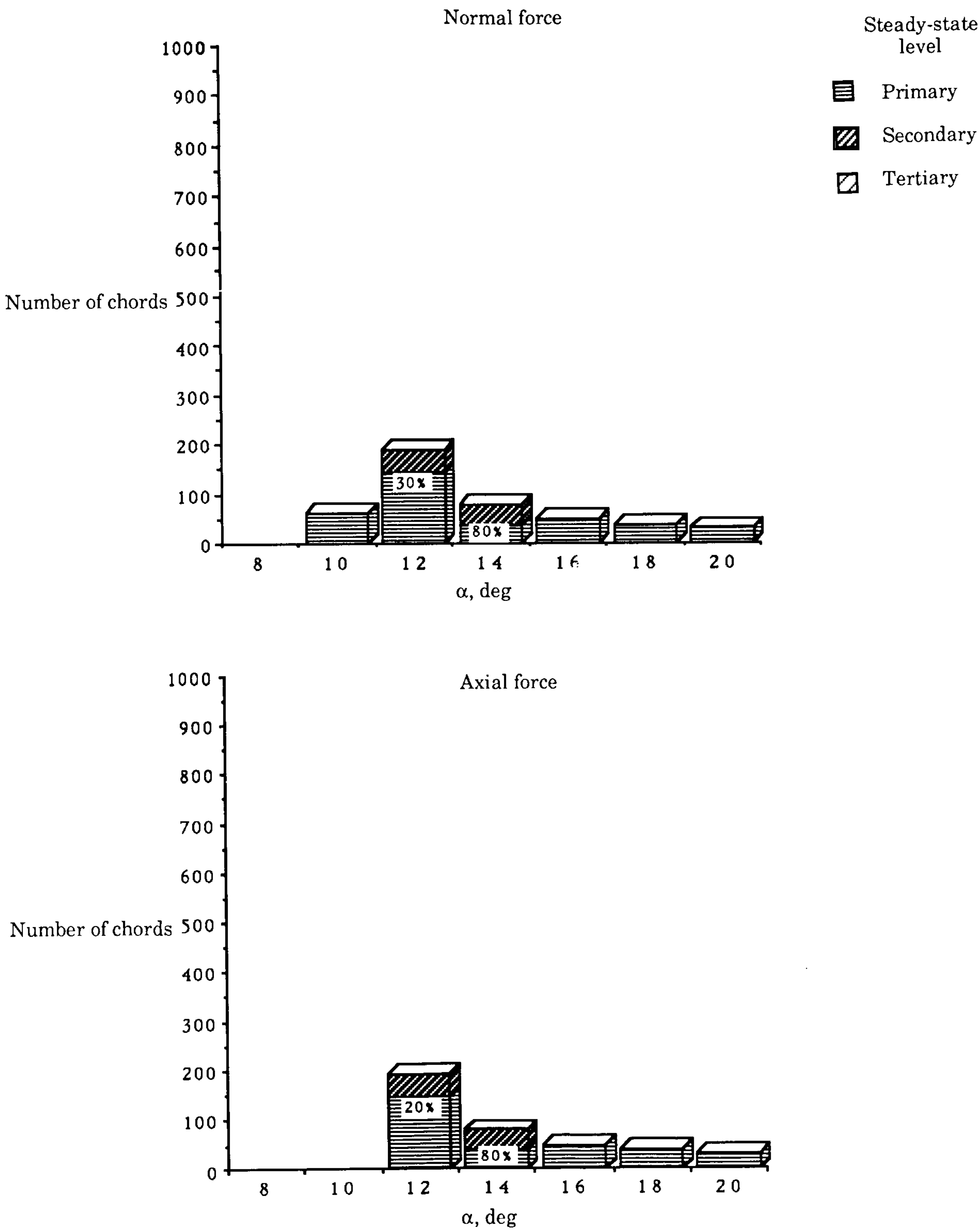

(e) $\delta = 20°$ and LWC = 10 g/m^3.

Figure C6. Continued.

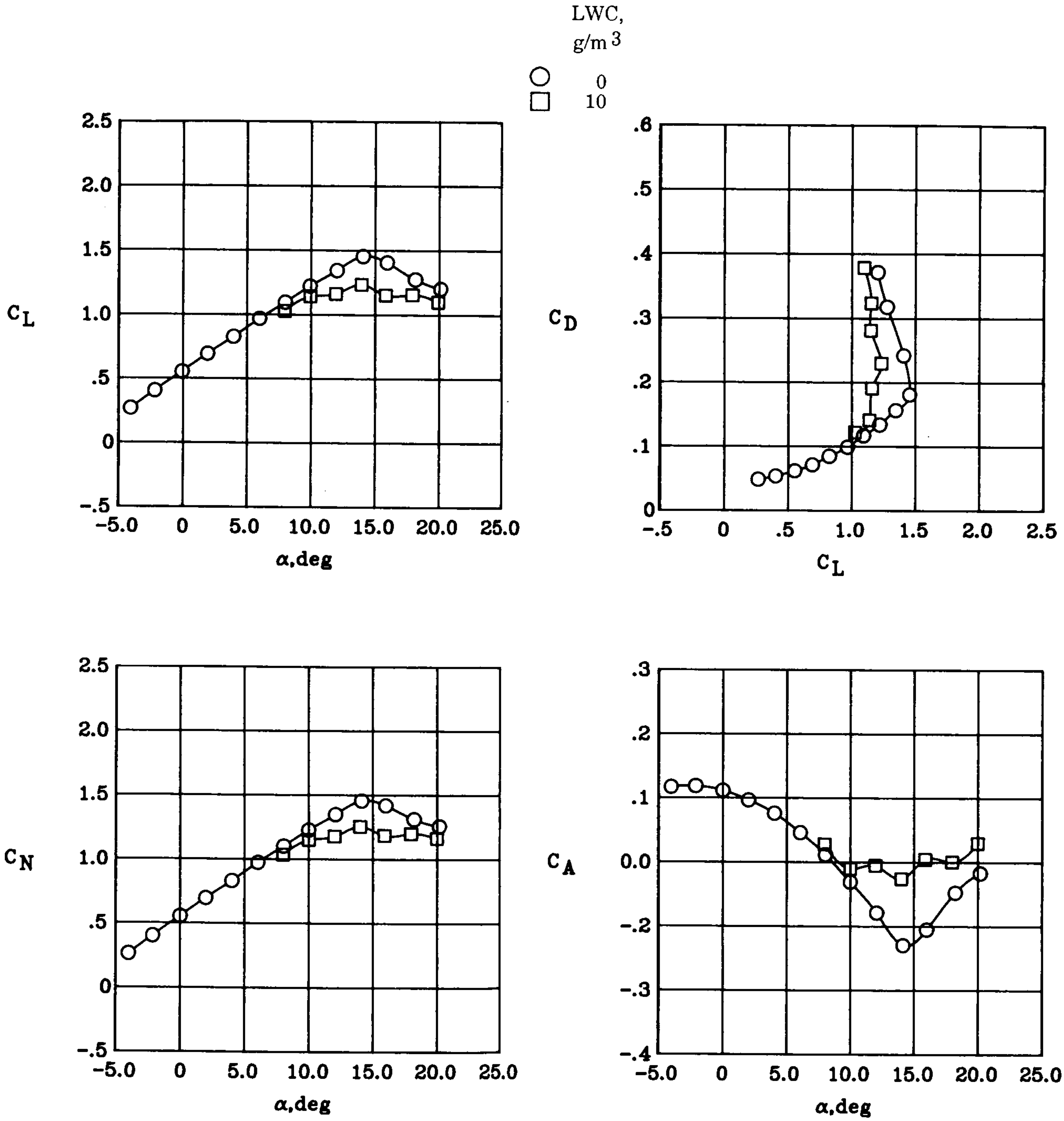

(f) $\delta = 20°$.

Figure C6. Concluded.

References

1. Spady, Amos A., Jr.; Bowles, Roland L.; and Schlickenmaier, Herbert, compilers: *Airborne Wind Shear Detection and Warning Systems—First Combined Manufacturers' and Technologists' Conference.* NASA CP-10006, DOT/FAA/PS-88/7, 1988.
2. National Research Council: *Low-Altitude Wind Shear and Its Hazard to Aviation.* National Academy Press, 1983.
3. Haines, P. A.; and Luers, J. K.: *Aerodynamic Penalties of Heavy Rain on a Landing Aircraft.* NASA CR-156885, 1982.
4. Hastings, E. C., Jr.; and Manuel, G. S.: Measurements of Water Film Characteristics on Airfoil Surfaces From Wind-Tunnel Tests With Simulated Heavy Rain. AIAA-85-0259, Jan. 1985.
5. Bezos, G. M.; Dunham, R. E., Jr.; Gentry, G. L., Jr.; and Melson, W. Edward, Jr.: Wind Tunnel Test Results of Heavy Rain Effects on Airfoil Performance. AIAA-87-0260, Jan. 1987.
6. Dunham, R. Earl, Jr.; Bezos, Gaudy M.; Gentry, Garl L., Jr.; and Melson, Edward, Jr.: Two-Dimensional Wind Tunnel Tests of a Transport-Type Airfoil in a Water Spray. AIAA-85-0258, Jan. 1985.
7. Dunham, R. E., Jr.: Potential Influences of Heavy Rain on General Aviation Airplane Performance. AIAA-86-2606, Sept.-Oct. 1986.
8. Dunham, R. Earl, Jr.: The Potential Influence of Rain on Airfoil Performance. Influence of Environmental Factors on Aircraft Wing Performance, VKI-LS-1987-03, Von Karman Inst. for Fluid Dynamics, Feb. 1987.
9. Hansman, R. John, Jr.; and Craig, Anthony P.: Comparative Low Reynolds Number Tests of NACA 64-210, NACA 0012, and Wortmann FX67-K170 Airfoils in Heavy Rain. AIAA-87-0259, Jan. 1987.
10. Taylor, John T.; Moore, Cadd T., III; Campbell, Bryan A.; and Melson, W. Edward, Jr.: The Development of a Facility for Full-Scale Testing of Airfoil Performance in Simulated Rain. AIAA-88-0055, Jan. 1988.
11. Bezos, Gaudy M.; Campbell, Bryan A.; and Melson, W. Edward: The Development of a Capability for Aerodynamic Testing of Large-Scale Wing Sections in a Simulated Natural Rain Environment. AIAA-89-0762, Jan. 1989.
12. Applin, Zachary T.: *Flow Improvements in the Circuit of the Langley 4- by 7-Meter Tunnel.* NASA TM-85662, 1983.
13. Braslow, Albert L.; Hicks, Raymond M.; and Harris, Roy V., Jr.: *Use of Grit-Type Boundary-Layer-Transition Trips on Wind-Tunnel Models.* NASA TN D-3579, 1966.
14. Bilanin, Alan J.: Scaling Laws for Testing of High Lift Airfoils Under Heavy Rainfall. AIAA-85-0257, Jan. 1985.
15. Schumacher, Paul W. J.; and Wilk, Kenneth E.: Liquid Water Content at High Levels. AIAA Paper No. 63-293, July 1963.
16. Hernan, M. A.; Gharib, M.; Parikh, P.; and Sarohia, V.: *Simulation and Analysis of Natural Rain in a Wind Tunnel Via Digital Image Processing Techniques—Interim Report.* JPL D-2231 (Contract NAS7-918, Task Order RE 65/Ammendment 459), California Inst. of Technology, Oct. 31, 1984.

Table I. Water Droplet Spray Characteristics

Nozzle	Q, gal/min	q, psf	V_∞, ft/sec	Spray area, ft^2	LWC,* g/m^3
B1N5	19.5	10	92	34	14
B1N5	19.5	30	159	24	12
B1N5	19.5	50	205	21	10
B1N7	27.0	10	92	31	21
B1N7	27.0	30	159	23	17
B1N7	27.0	50	205	19	15
1570	41.2	10	92	47	21
1570	41.2	30	159	25	23
1570	41.2	50	205	20	22

*LWC = $\frac{KQ}{V_\infty HW}$, where K = 2225.8086.

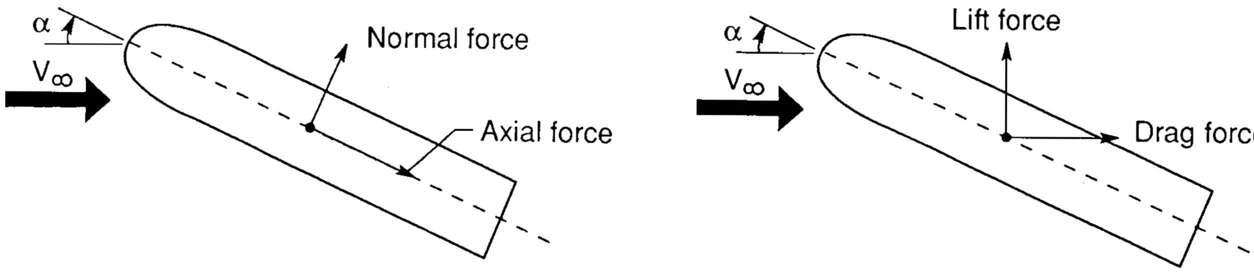

(a) Body-axis system.

(b) Wind-axis system.

Figure 1. Measurement axis systems.

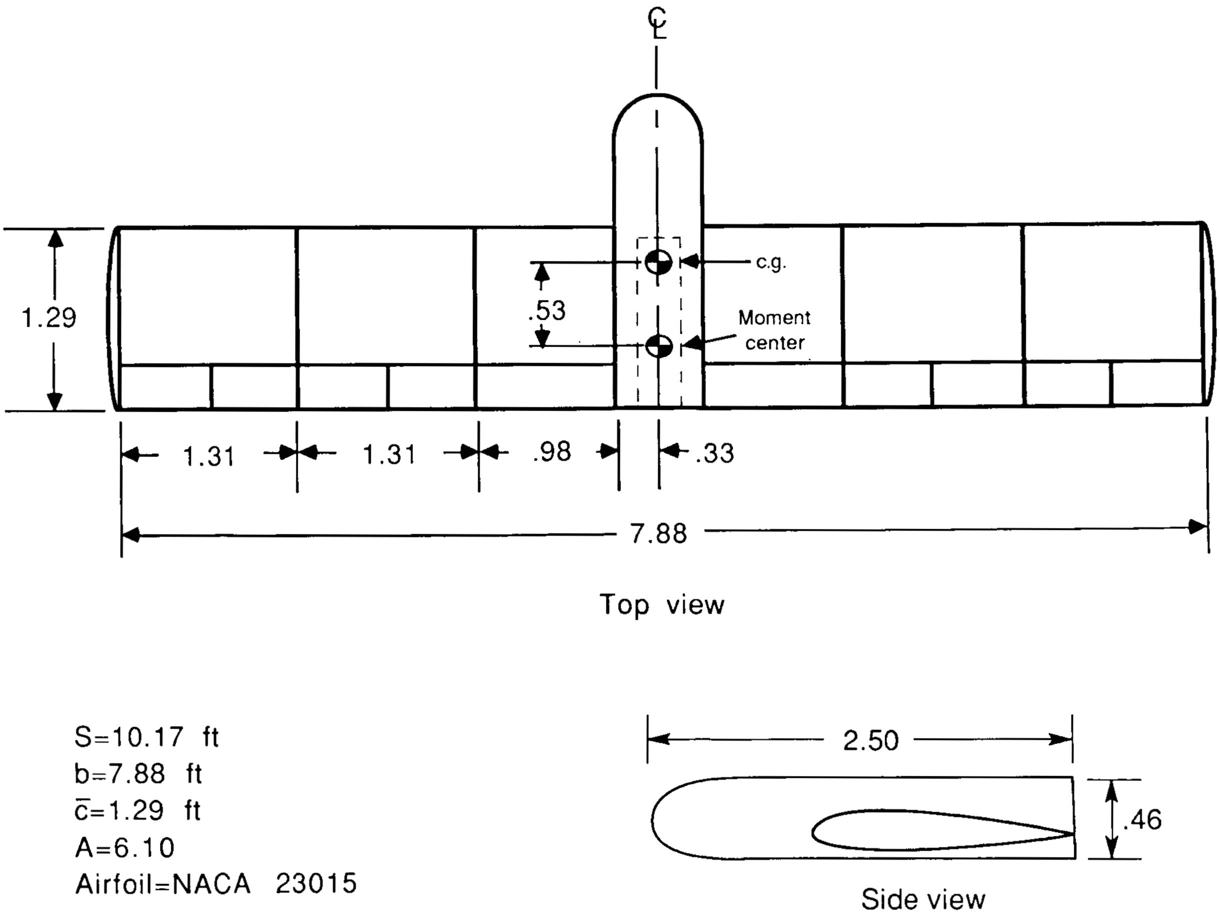

Figure 2. Geometric characteristics of wing model. All linear measurements are in feet and have been rounded off to two decimal places.

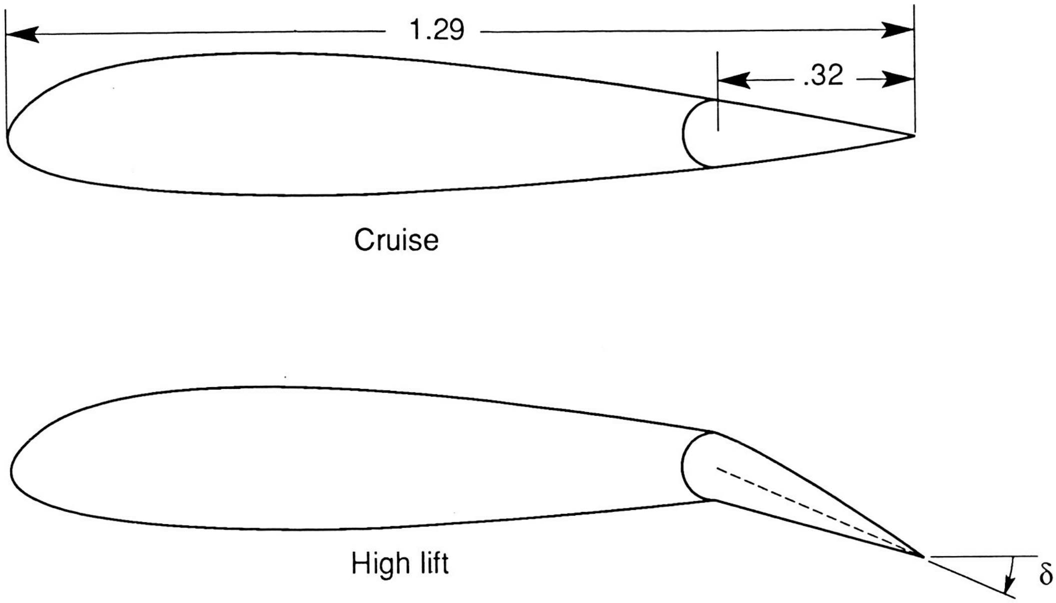

Figure 3. Cross section of NACA 23015 airfoil in cruise ($\delta = 0°$) and high-lift ($\delta = 20°$) configurations. All linear measurements are in feet and have been rounded off to two decimal places.

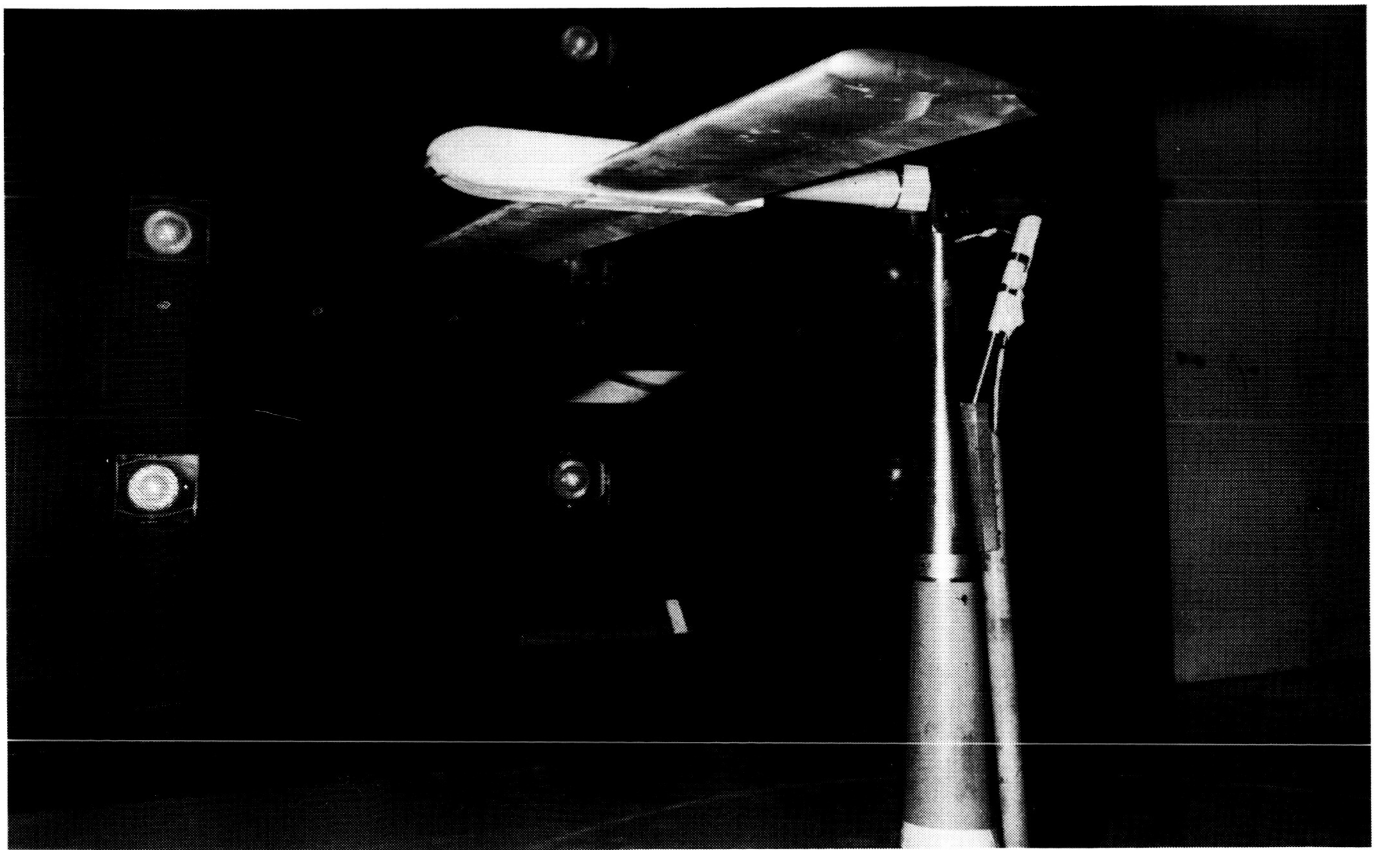

L-86-10524

Figure 4. Model in Langley 14- by 22-Foot Subsonic Tunnel.

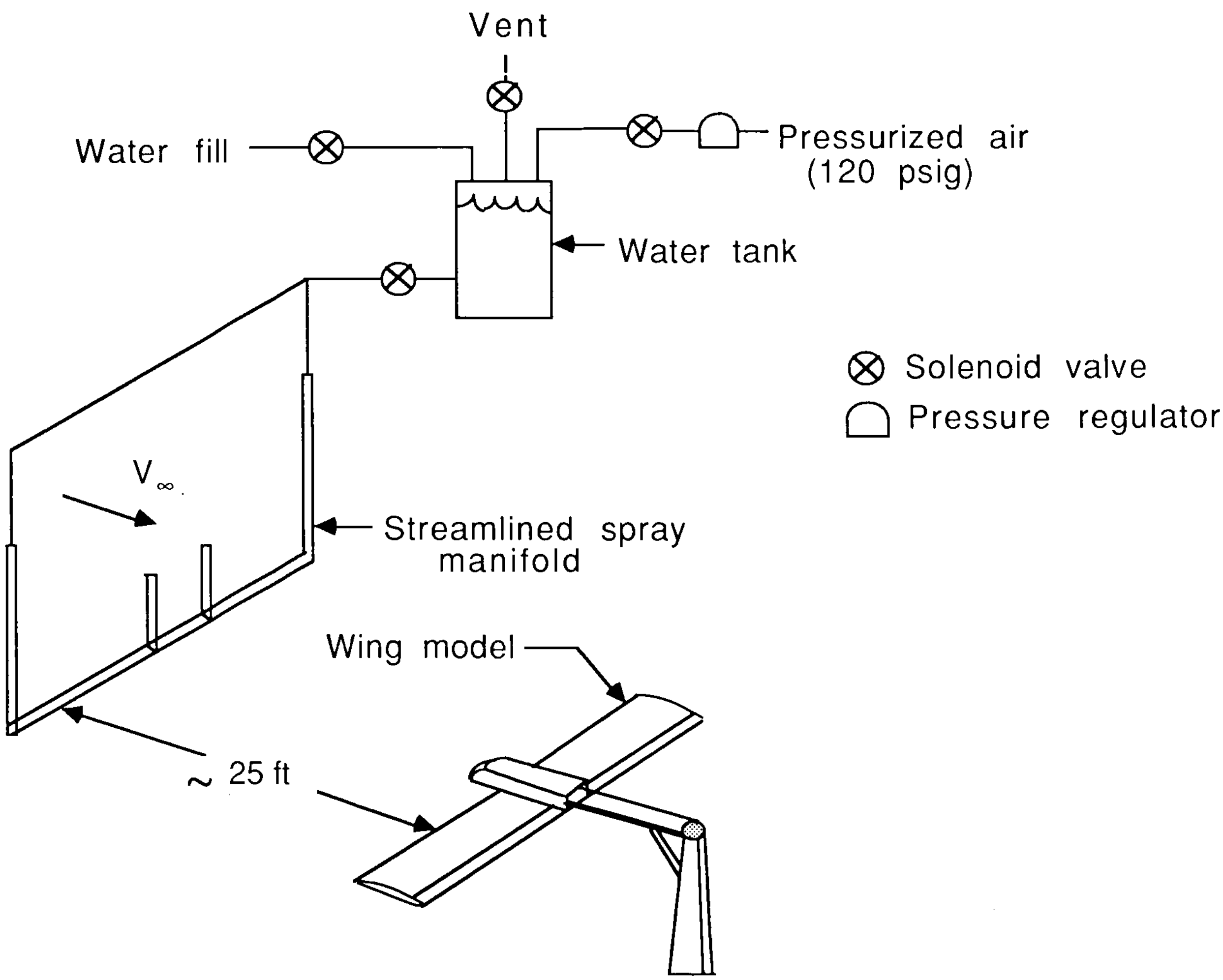

Figure 5. Rain simulation system.

L-87-07697

Figure 6. Rain simulation system mounted in Langley 14- by 22-Foot Subsonic Tunnel.

L-86-10526

Figure 7. Close-up detail of nozzle and solenoid arrangement on the spray manifold.

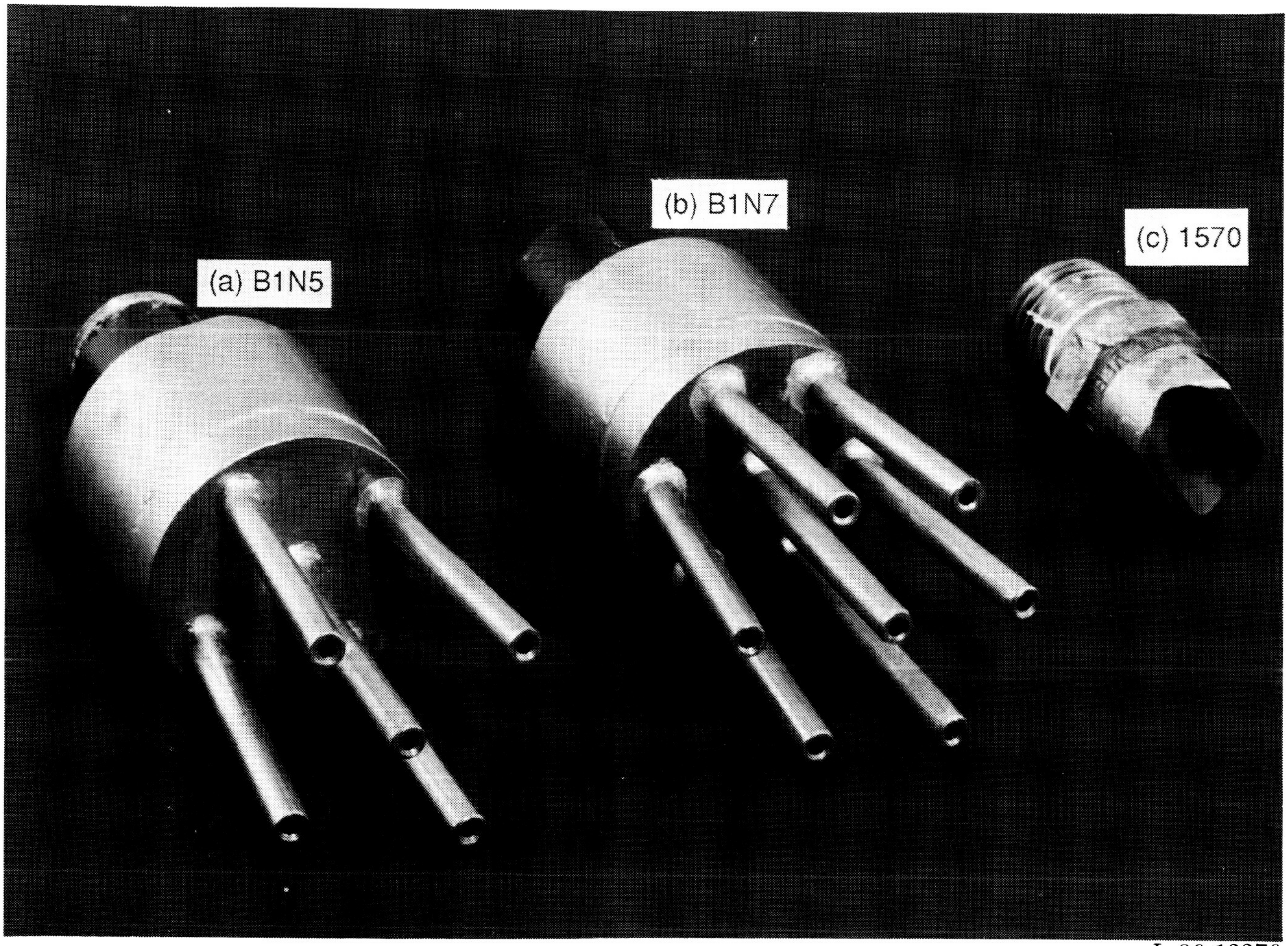

L-86-12276

Figure 8. Test nozzles.

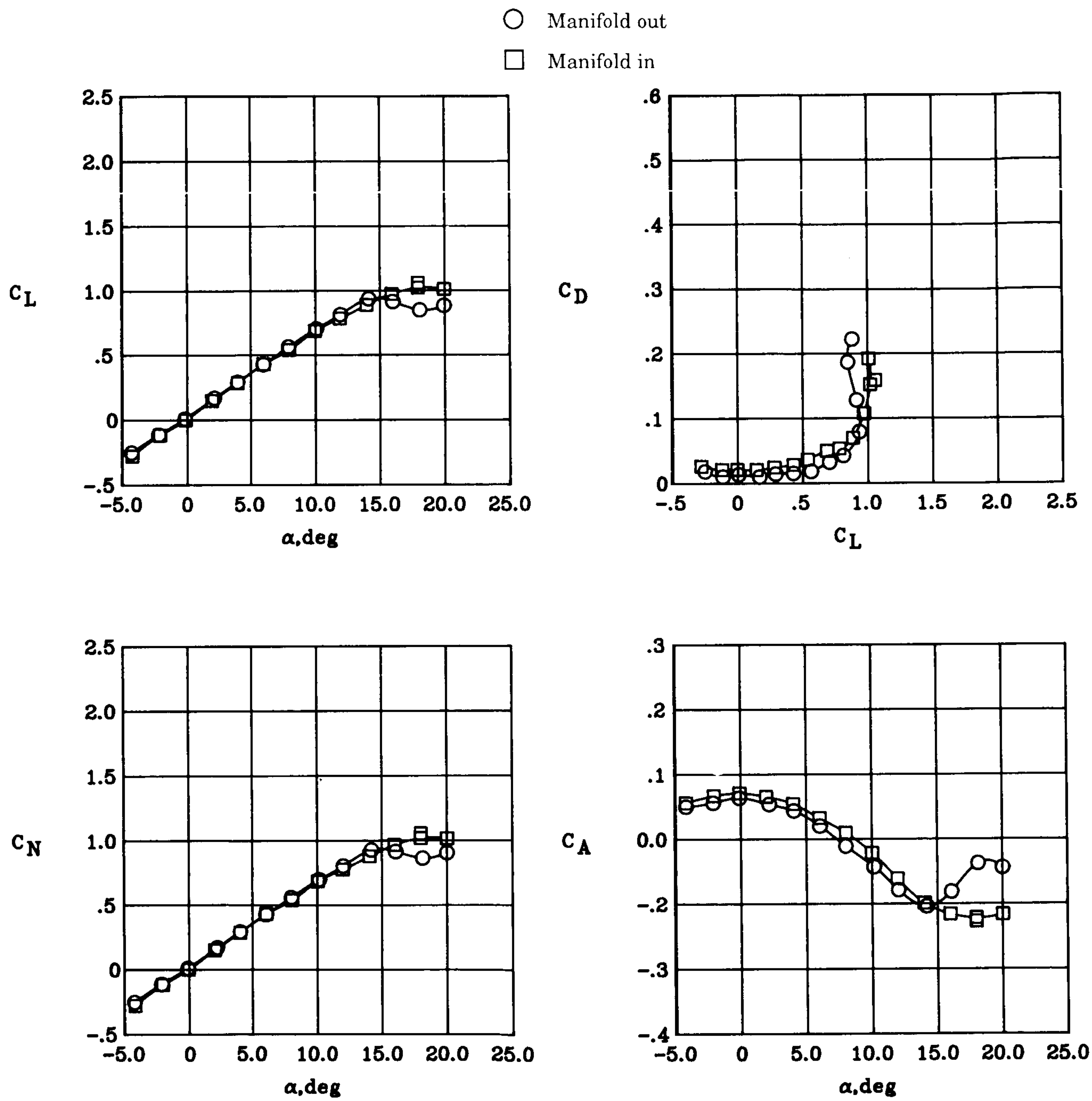

(a) $q = 10$ psf.

Figure 9. Effects of spray manifold on wing aerodynamics. $\delta = 0°$.

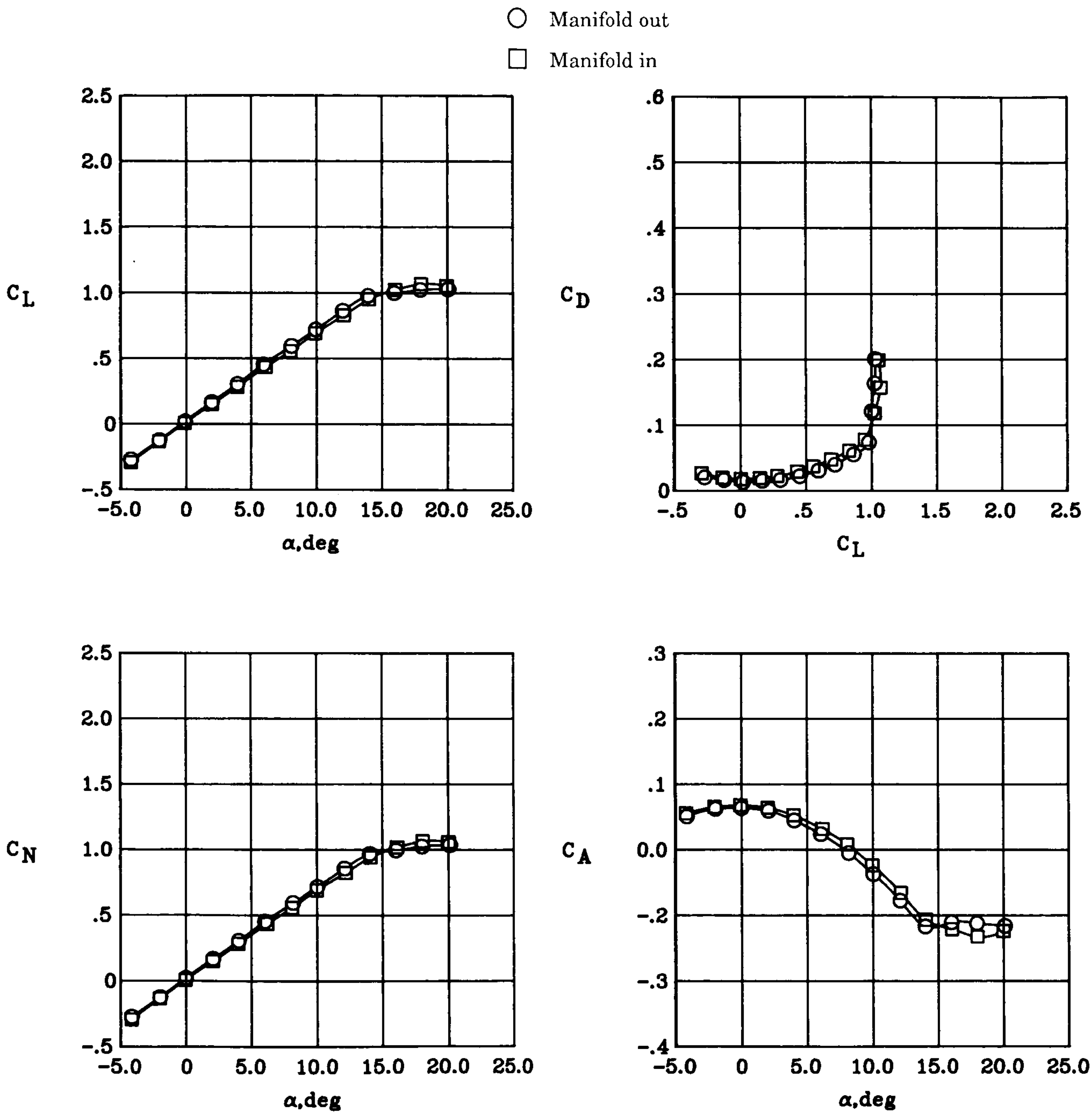

(b) $q = 30$ psf.

Figure 9. Continued.

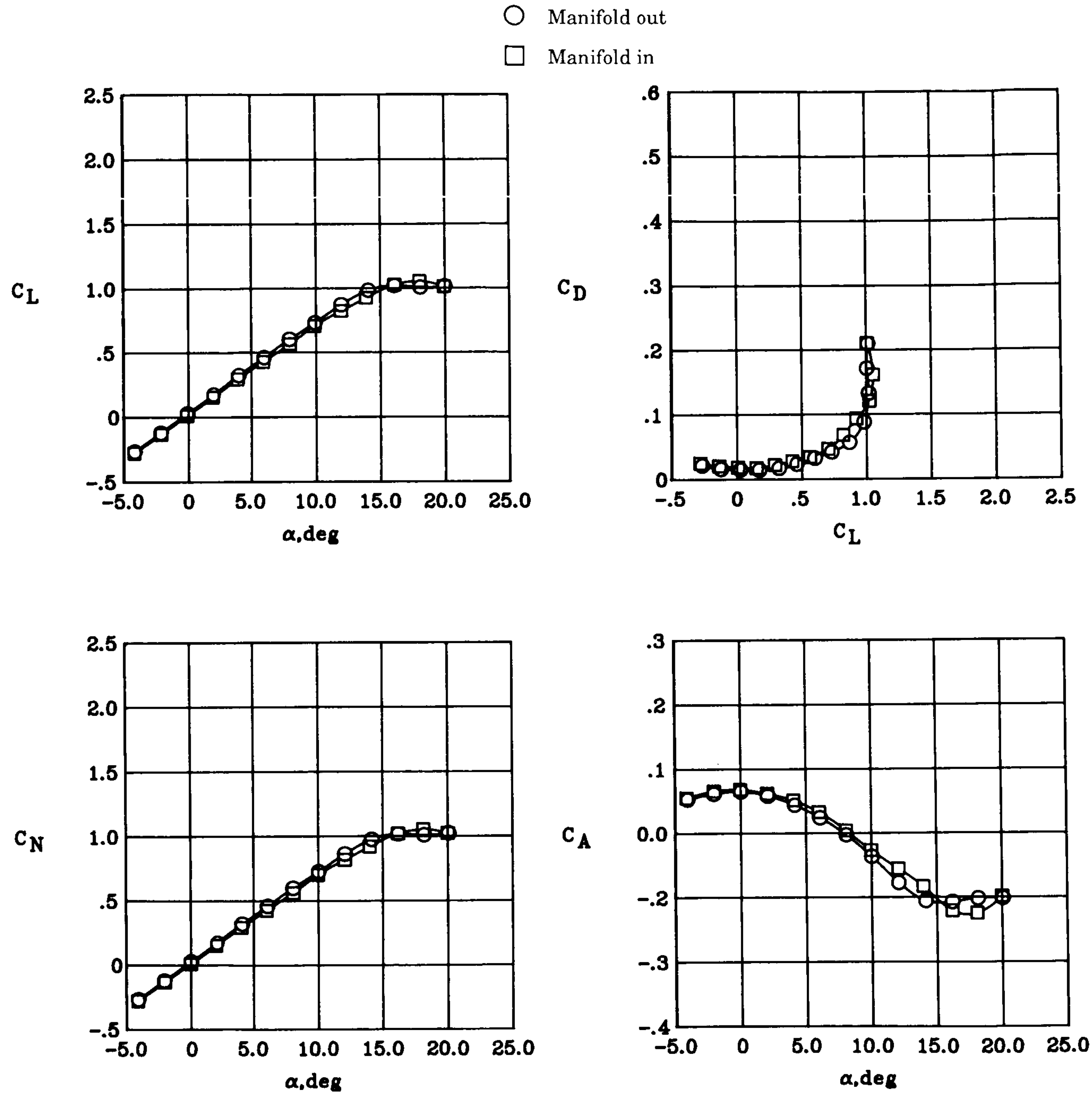

(c) $q = 50$ psf.

Figure 9. Concluded.

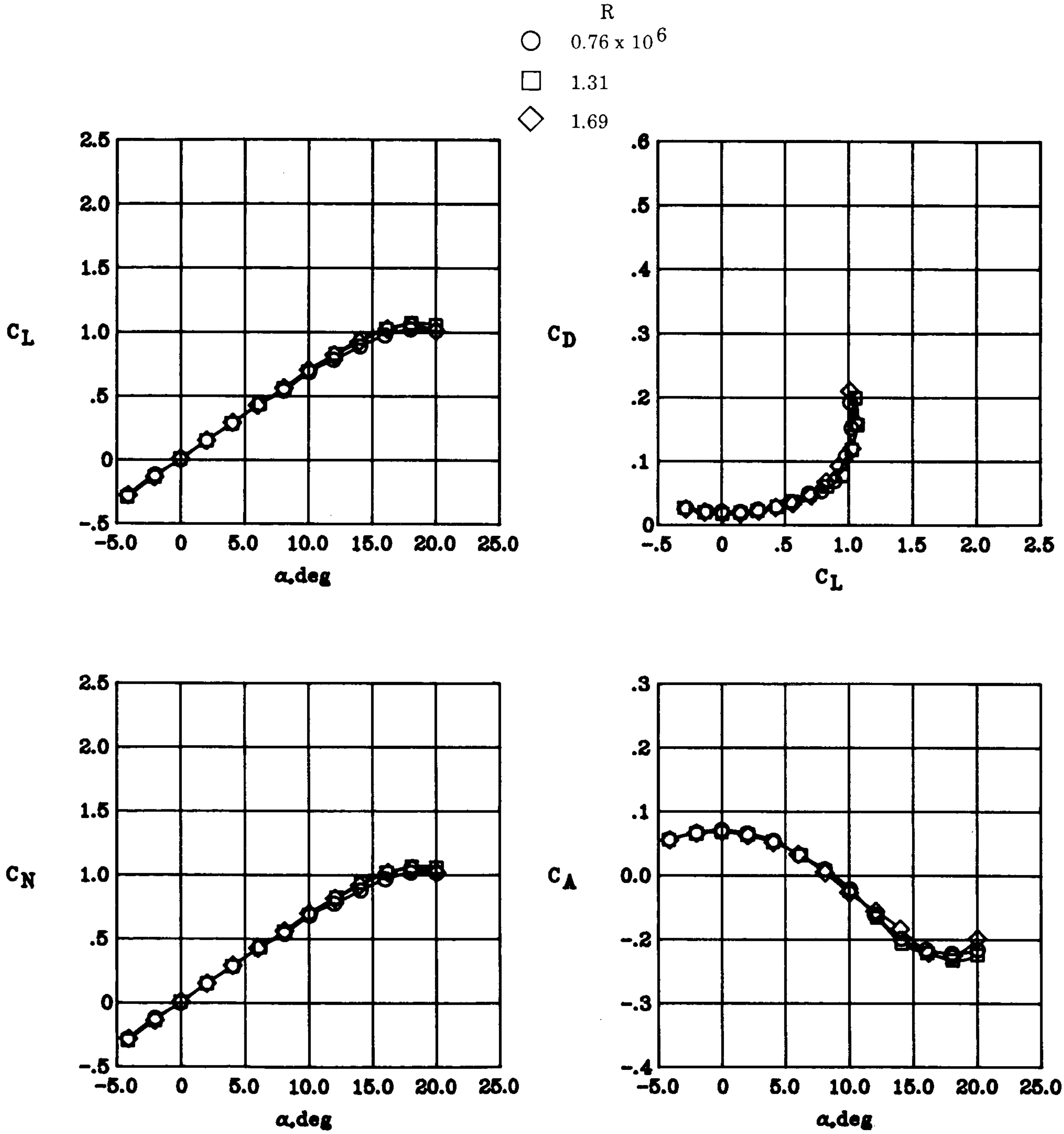

(a) Spray manifold installed; $\delta = 0°$.

Figure 10. Effects of Reynolds number variation on wing aerodynamics.

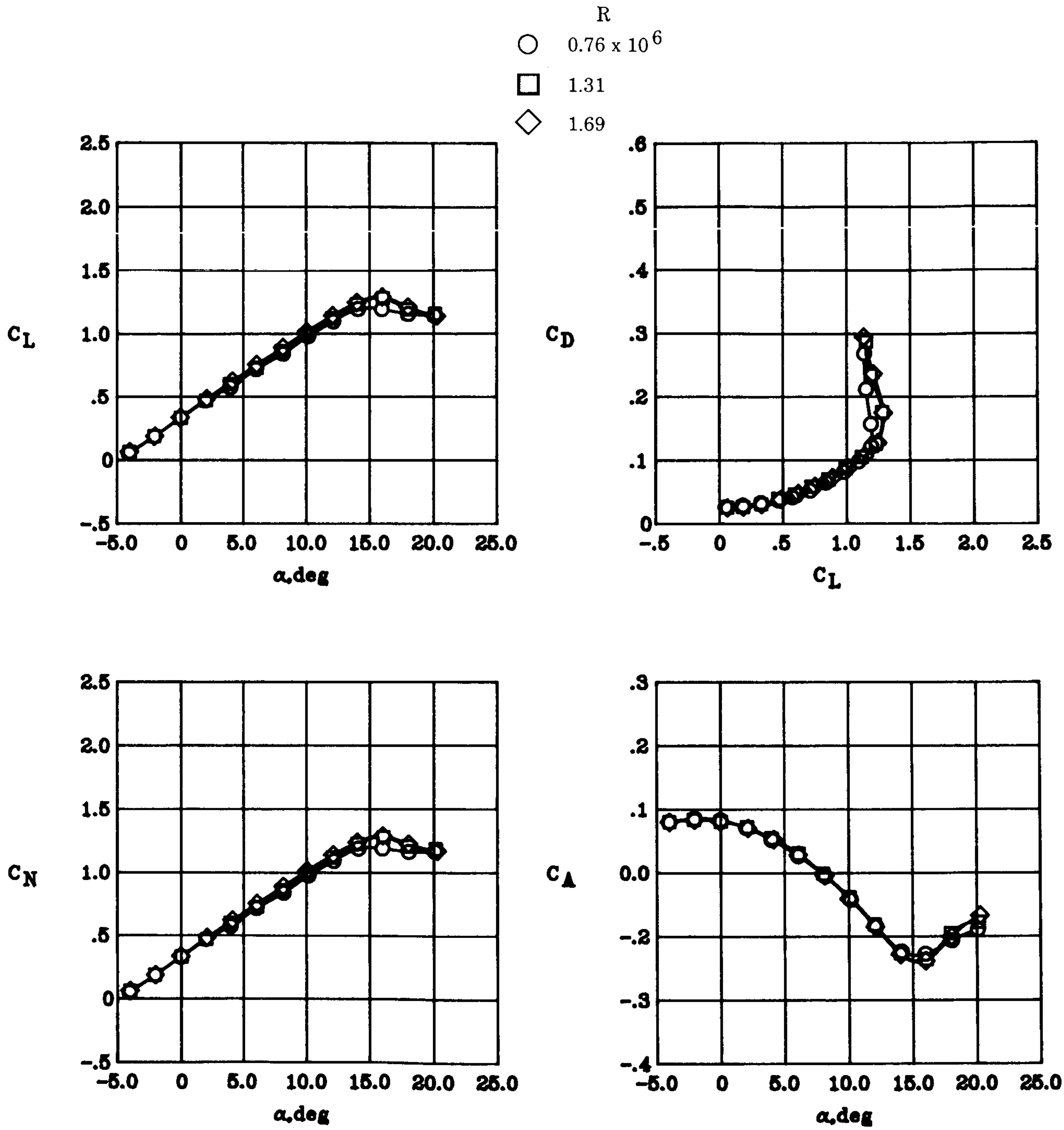

(b) Spray manifold installed; $\delta = 10°$

Figure 10. Continued.

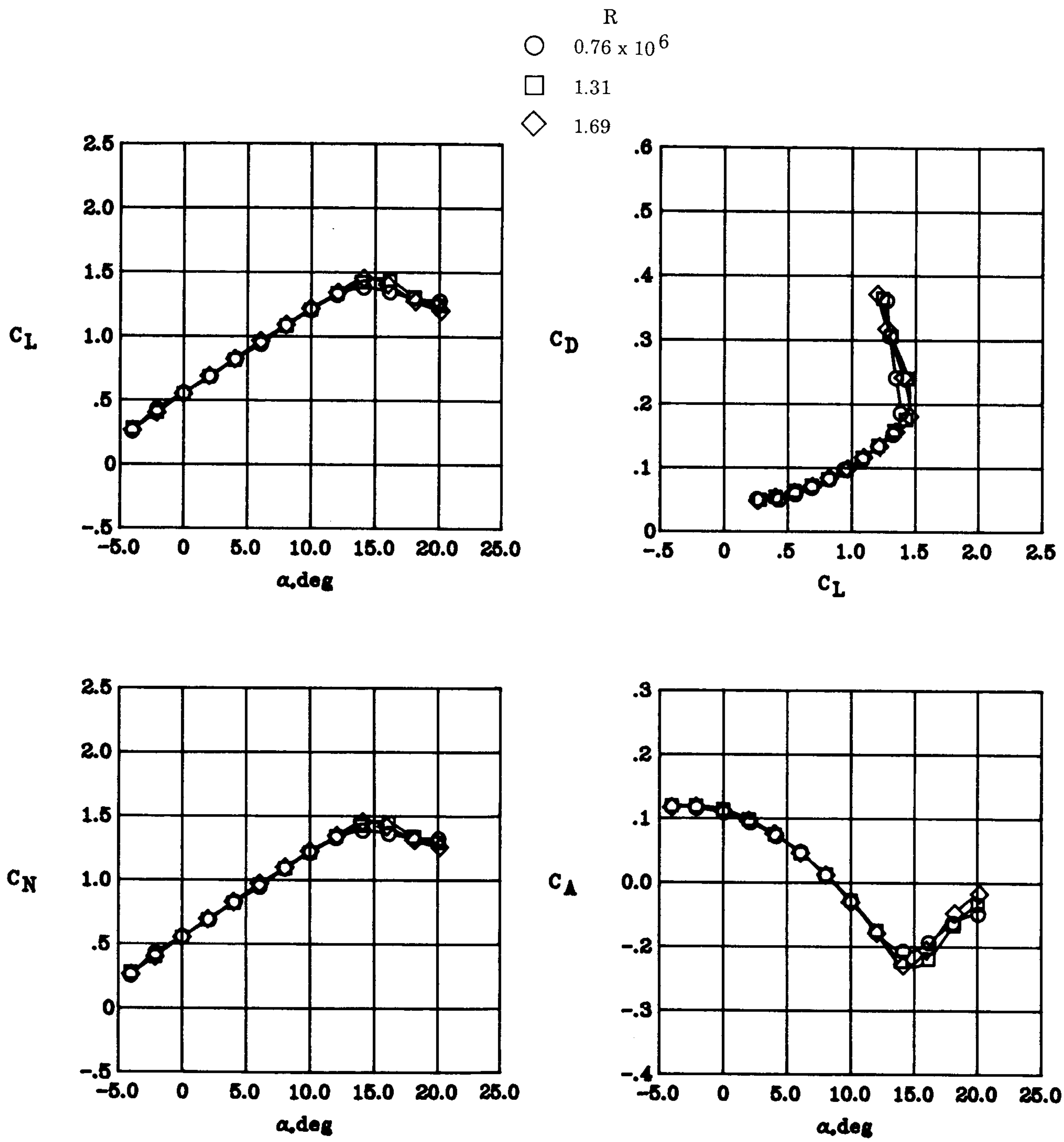

(c) Spray manifold installed; $\delta = 20°$.

Figure 10. Continued.

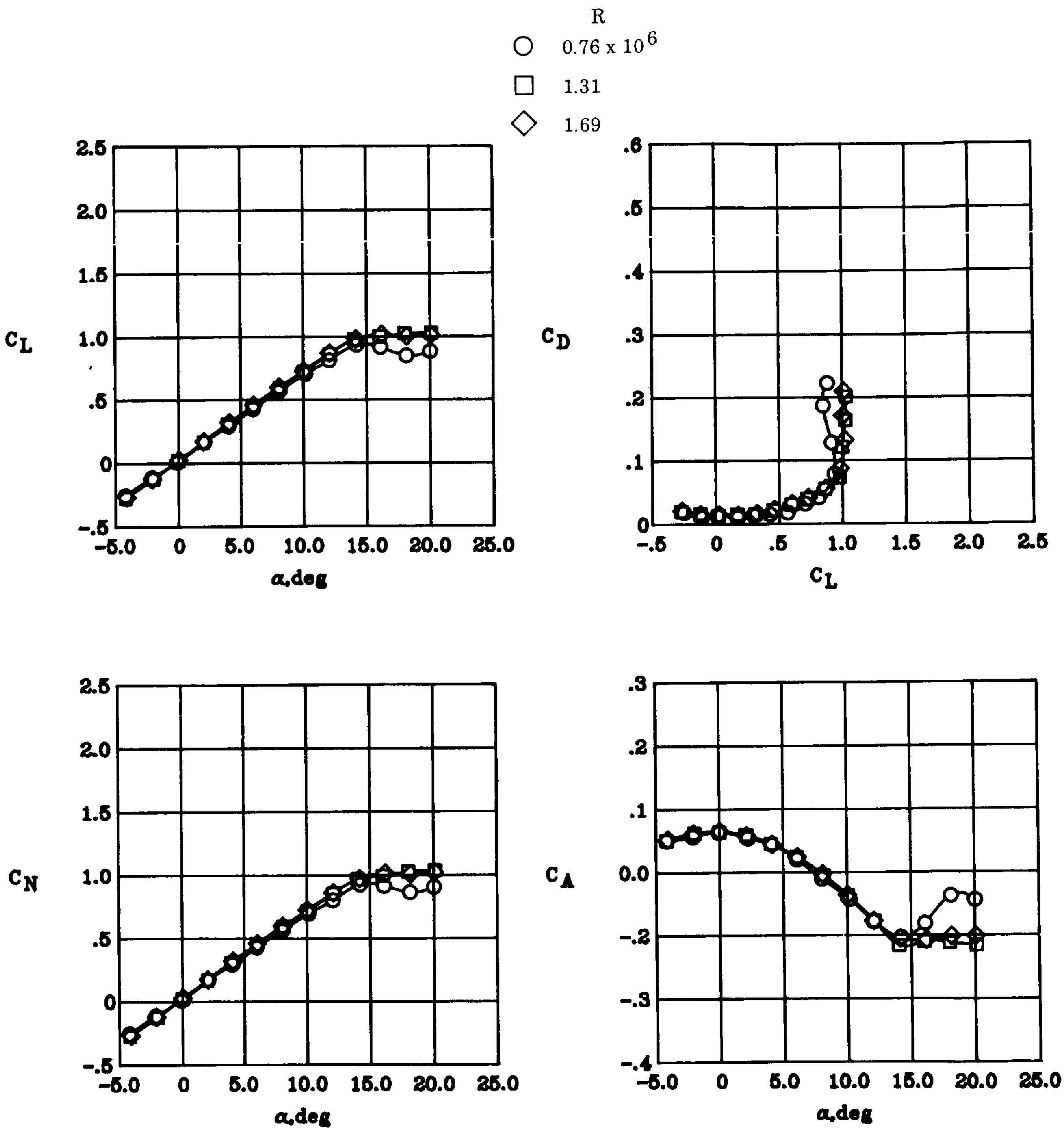

(d) Spray manifold removed; $\delta = 0°$.

Figure 10. Concluded.

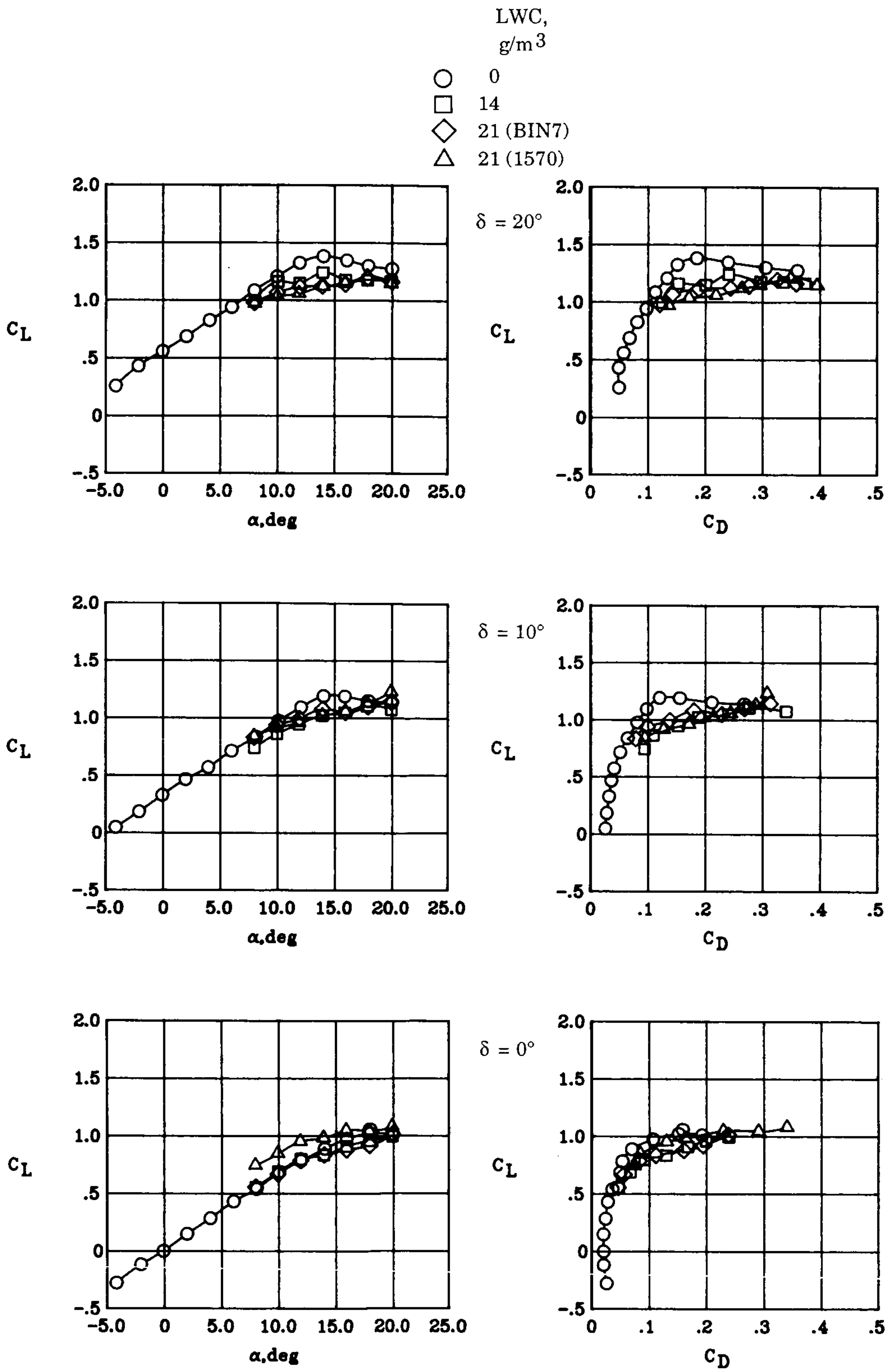

Figure 11. Effects of rain on steady-state force coefficients for $q = 10$ psf.

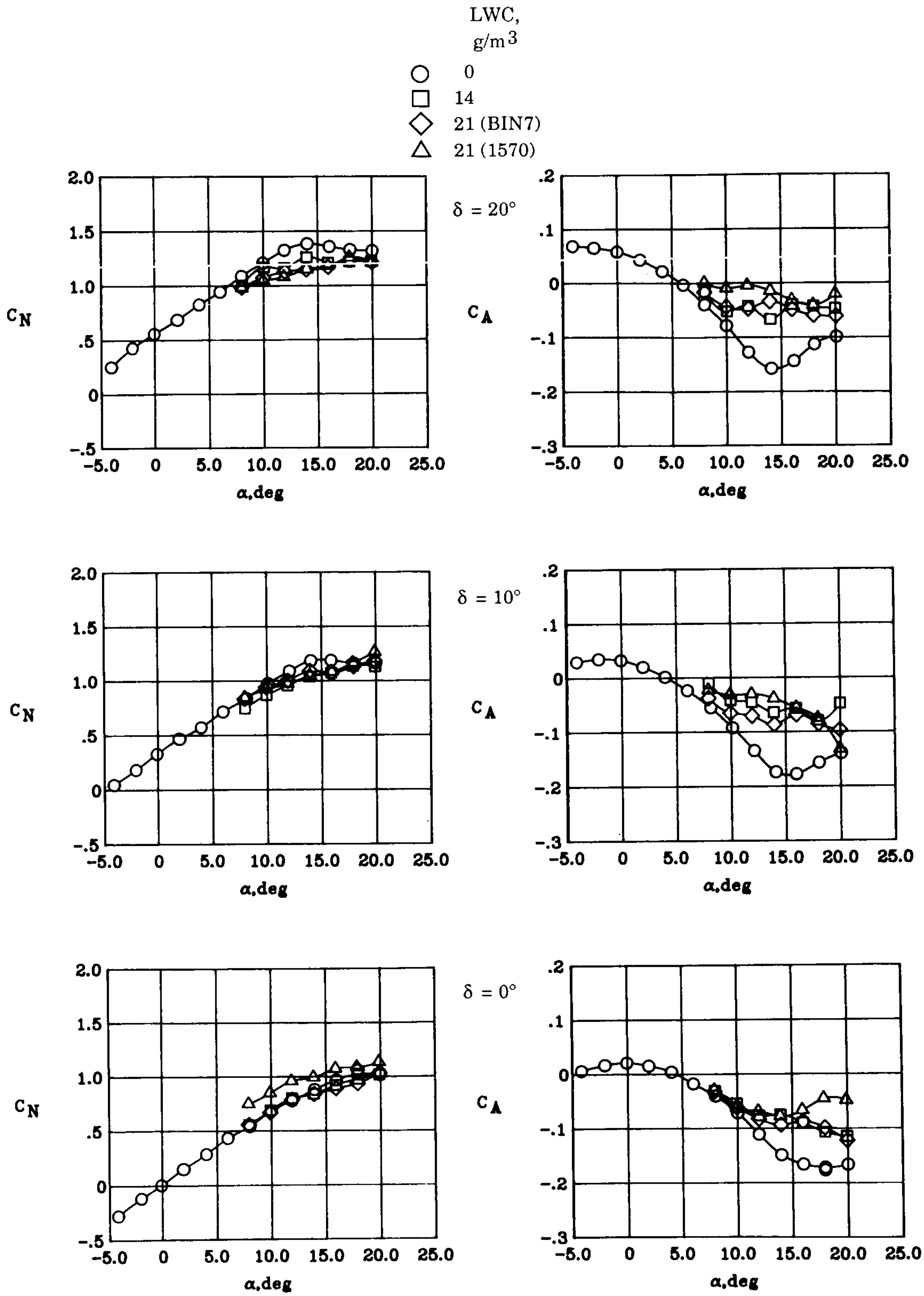

Figure 11. Concluded.

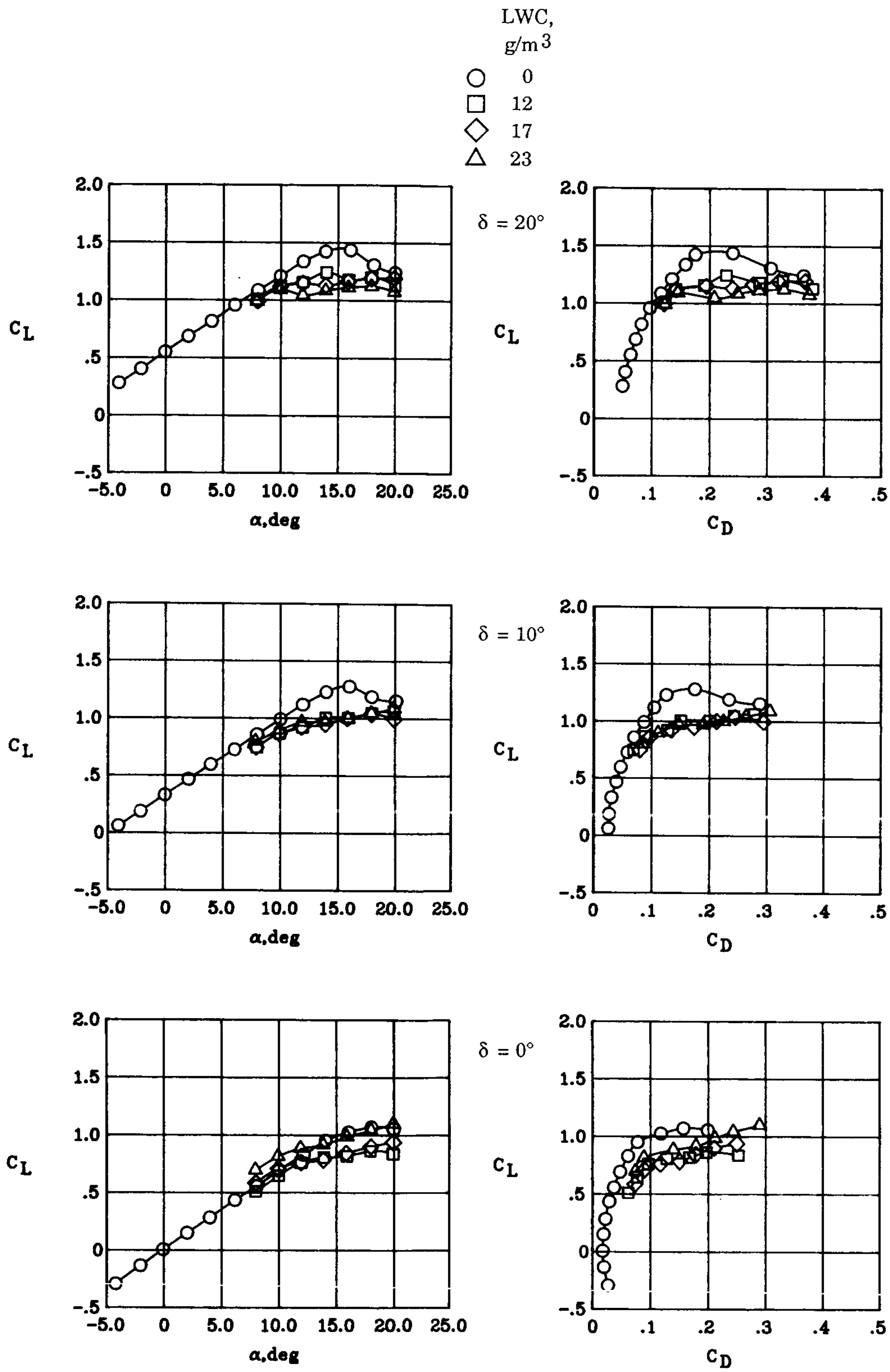

Figure 12. Effects of rain on steady-state force coefficients for $q = 30$ psf.

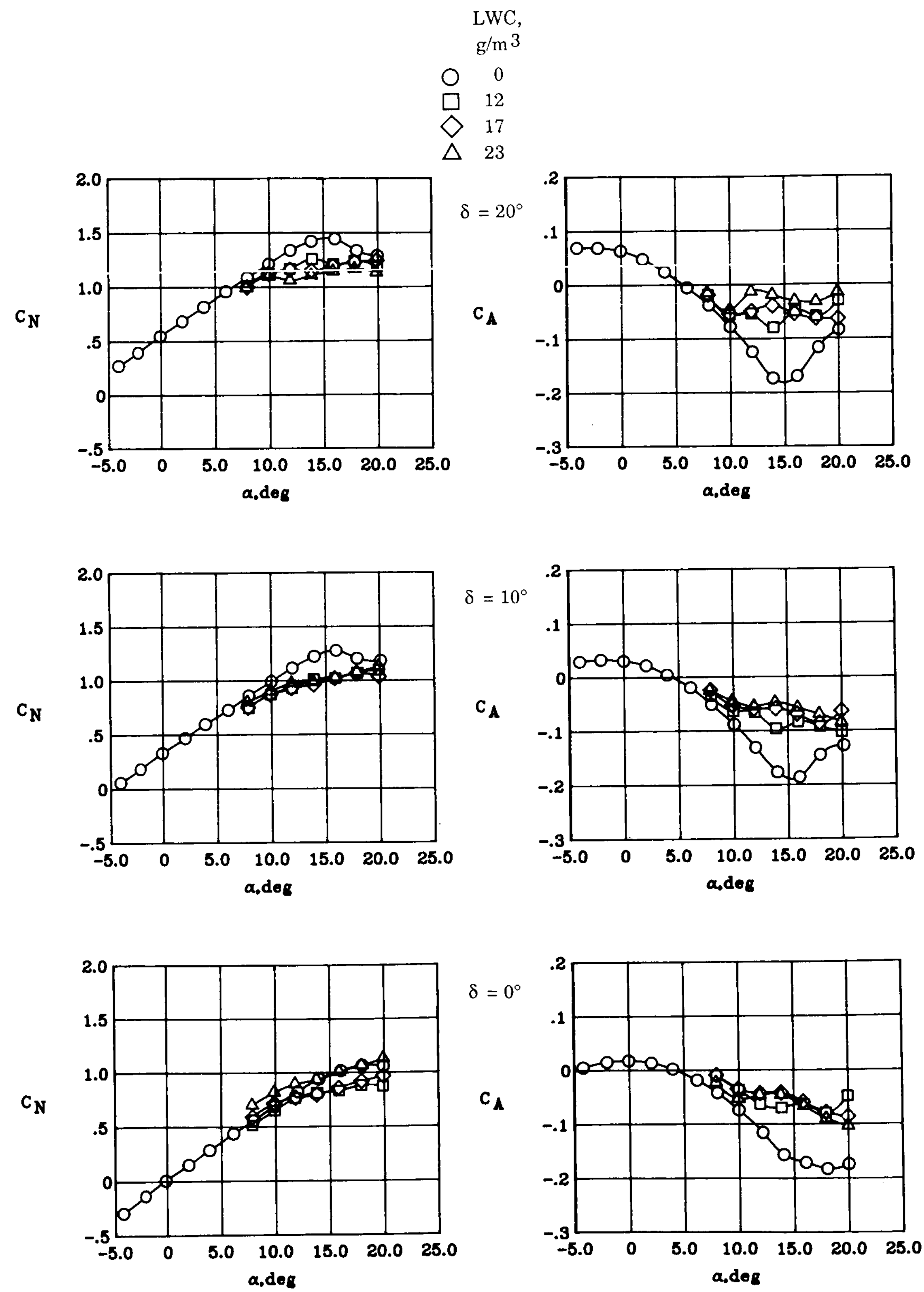

Figure 12. Concluded.

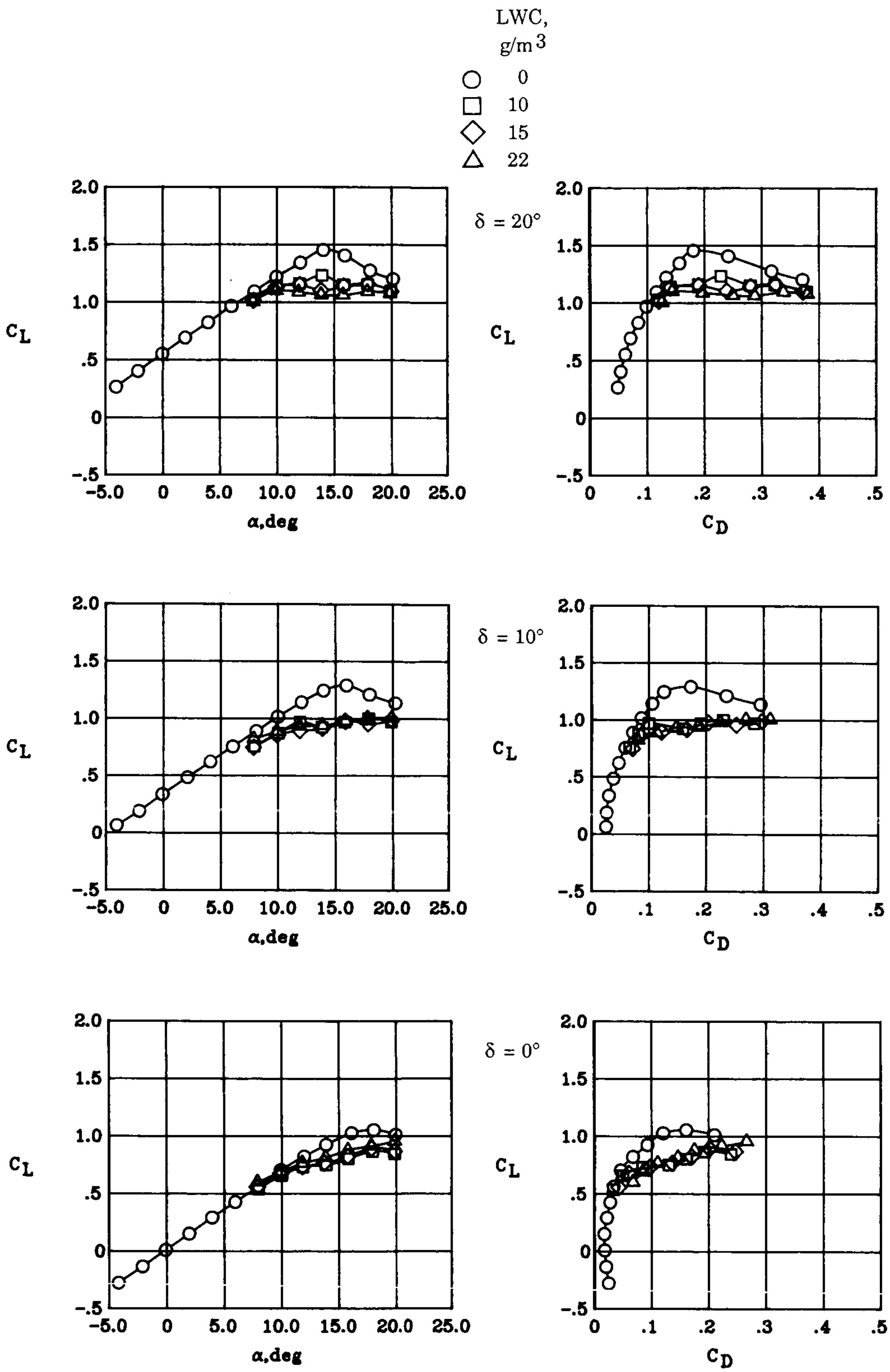

Figure 13. Effects of rain on steady-state force coefficients for $q = 50$ psf.

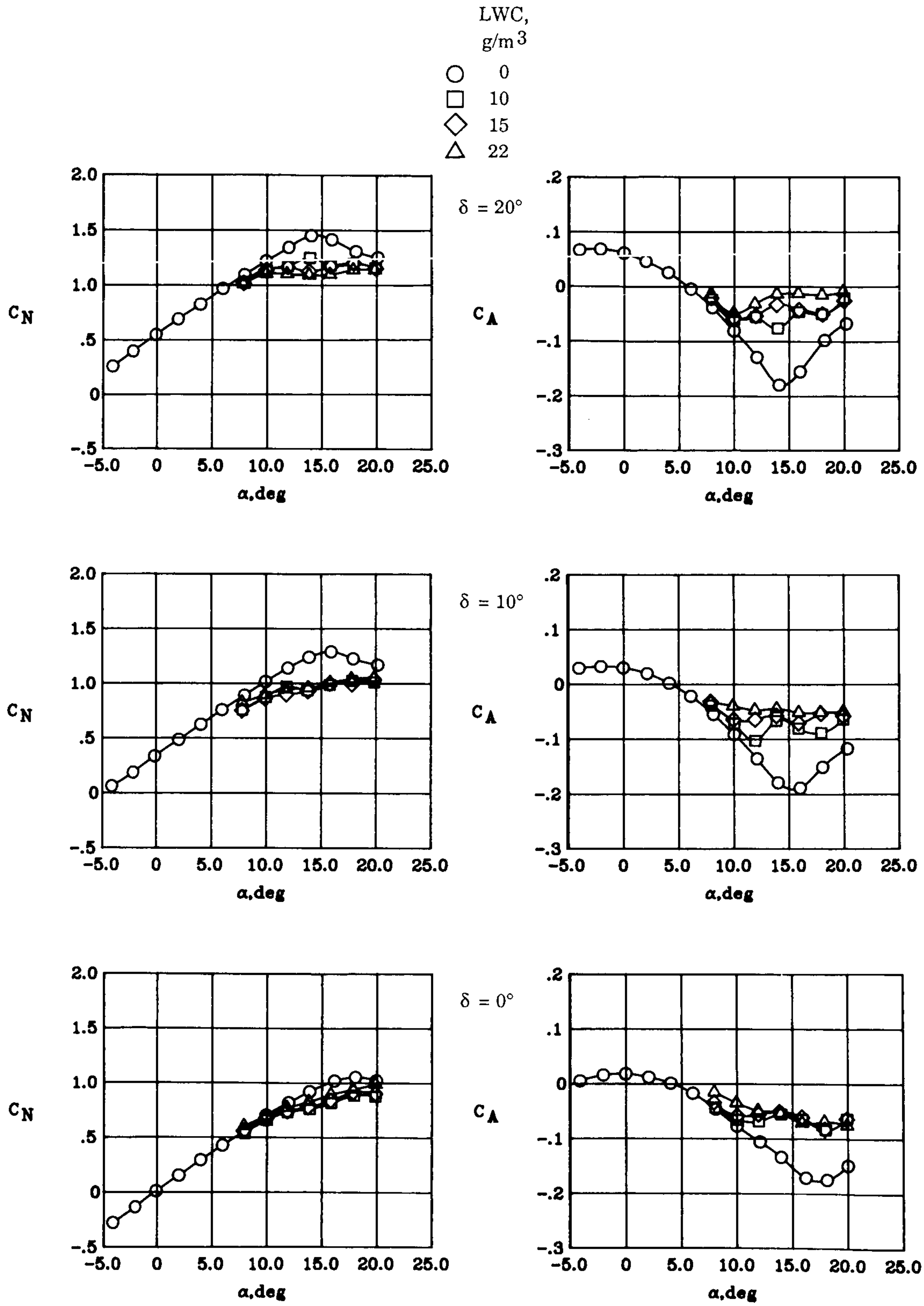

Figure 13. Concluded.

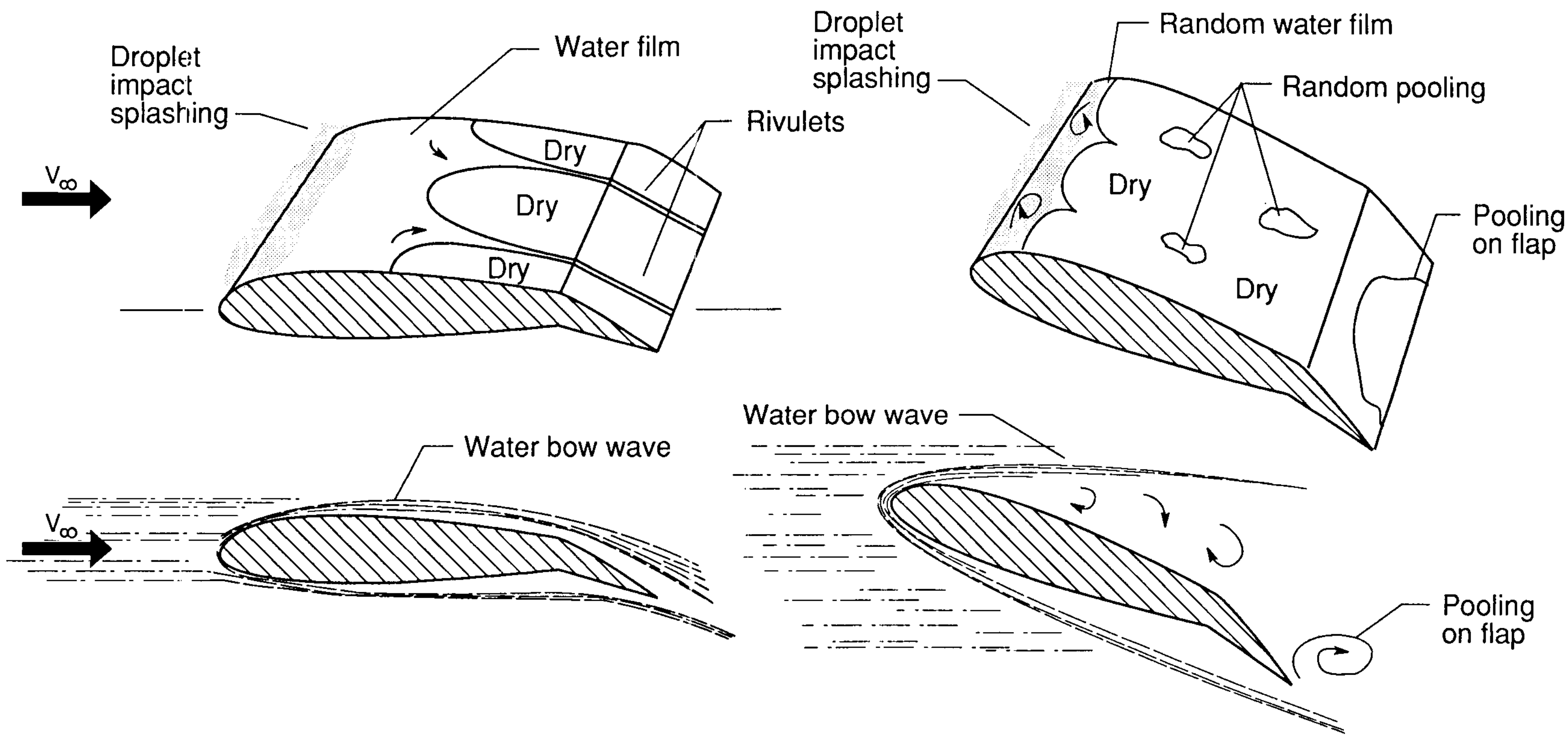

(a) Attached wing water flow.

(b) Stalled wing water flow.

Figure 14. Water flow characteristics about wing model.

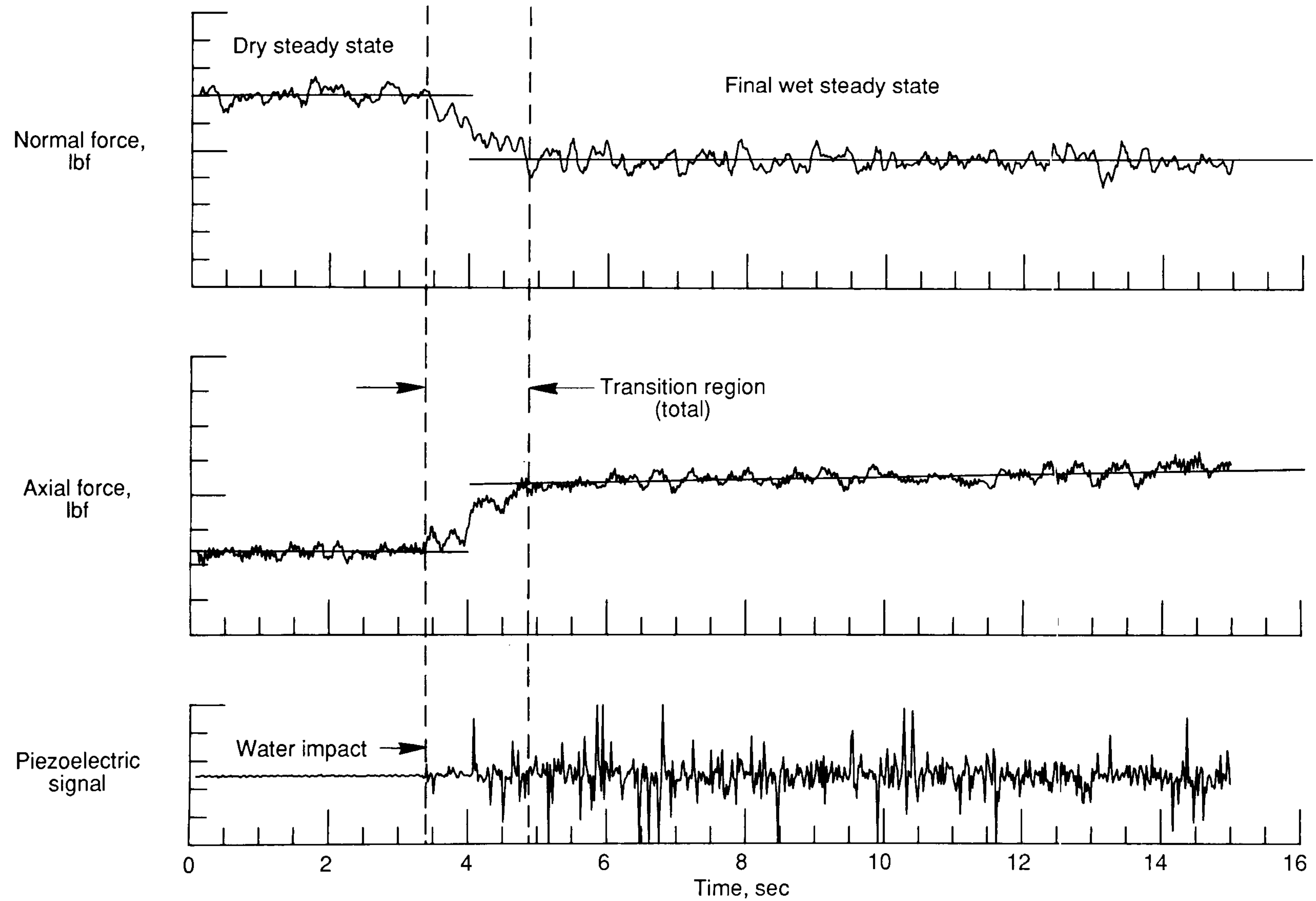

Figure 15. Dynamic force data for $q = 30$ psf. $\delta = 0°$; $\alpha = 14°$; LWC = 23 g/m^3.

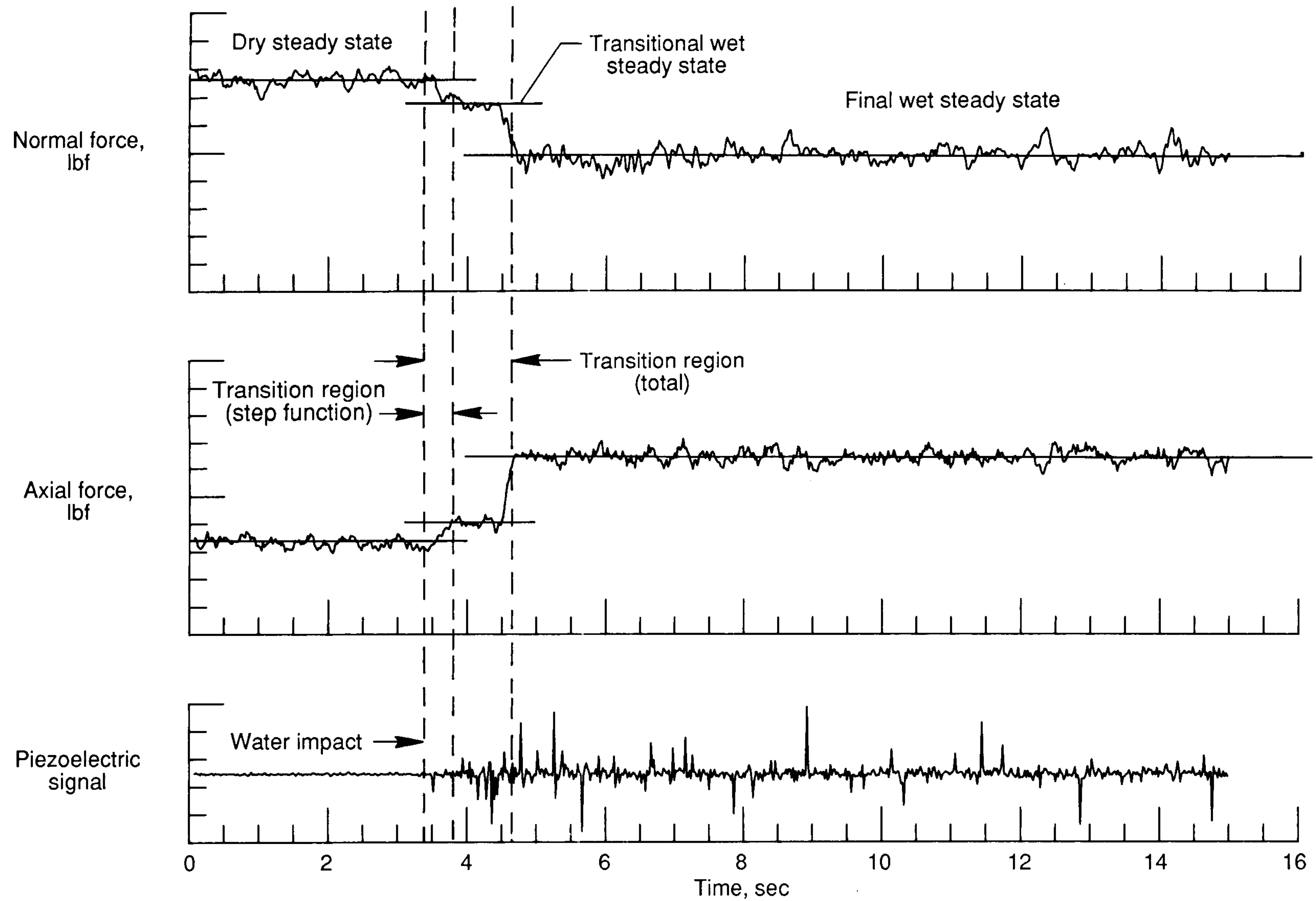

Figure 16. Dynamic force data for $q = 50$ psf. $\delta = 20°$; $\alpha = 12°$; LWC = 10 g/m^3.

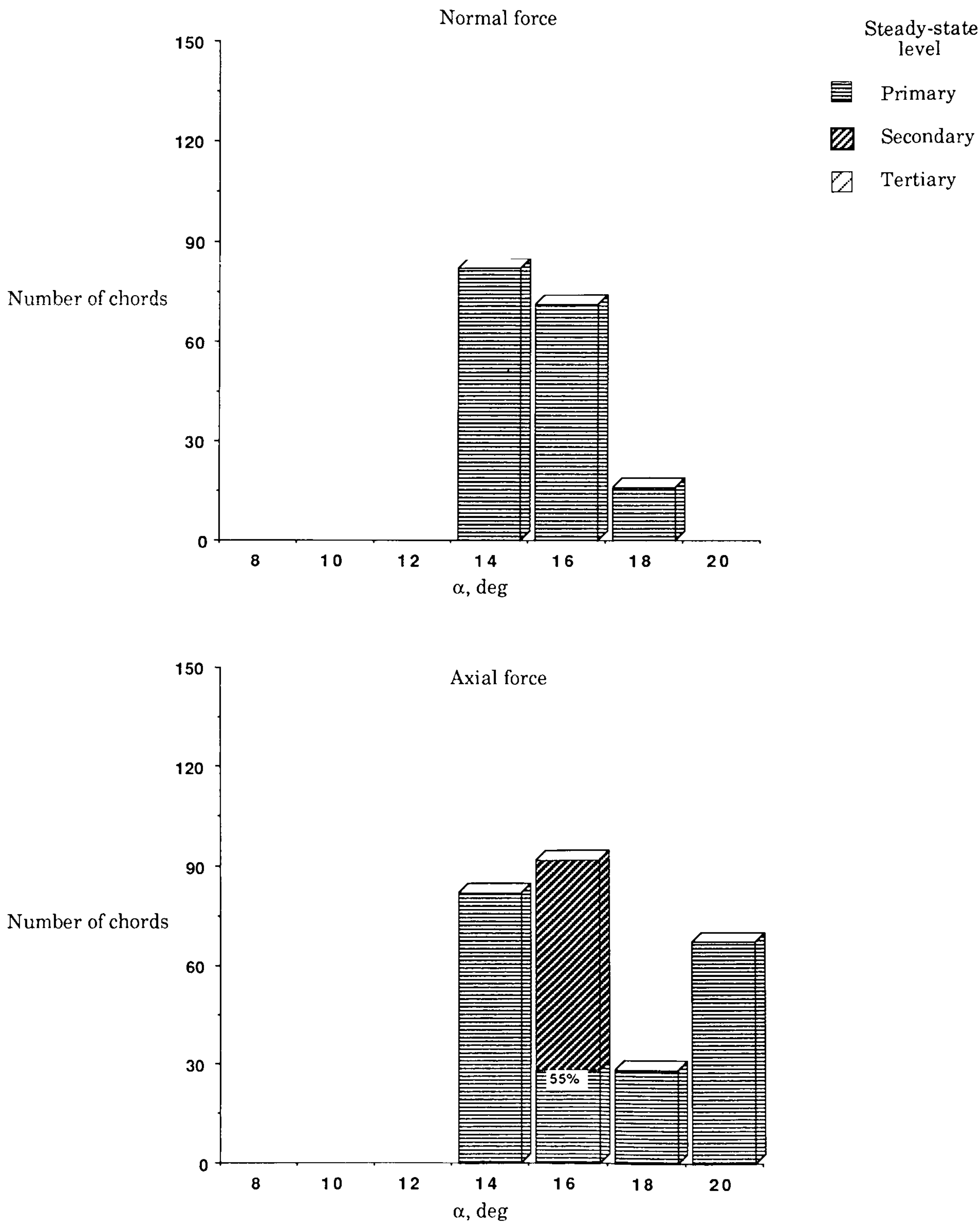

(a) $\delta = 0°$.

Figure 17. Dry to wet transition times for 1570 nozzles, $q = 10$ psf, and LWC = 21 g/m^3.

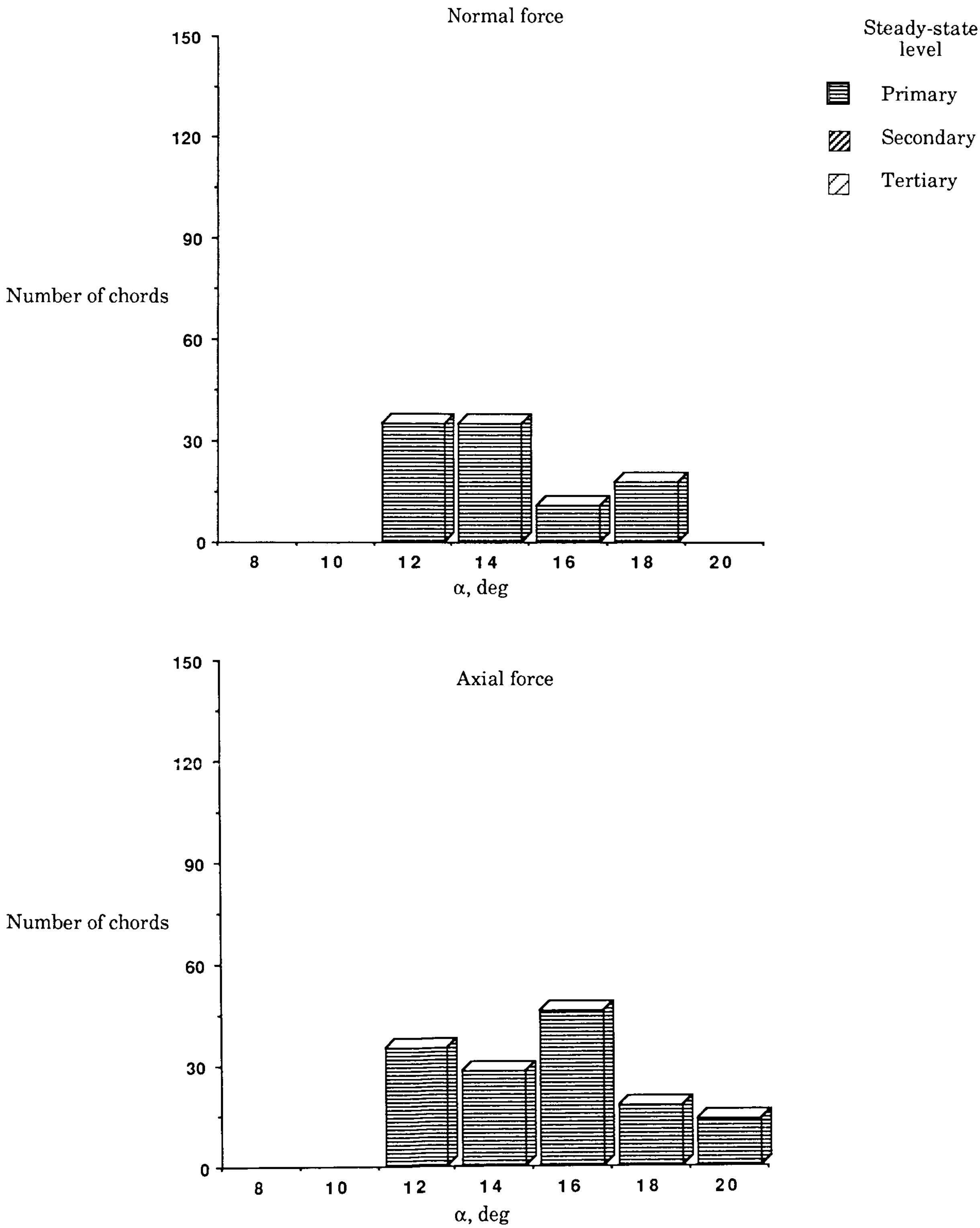

(b) $\delta = 10^{\circ}$.

Figure 17. Continued.

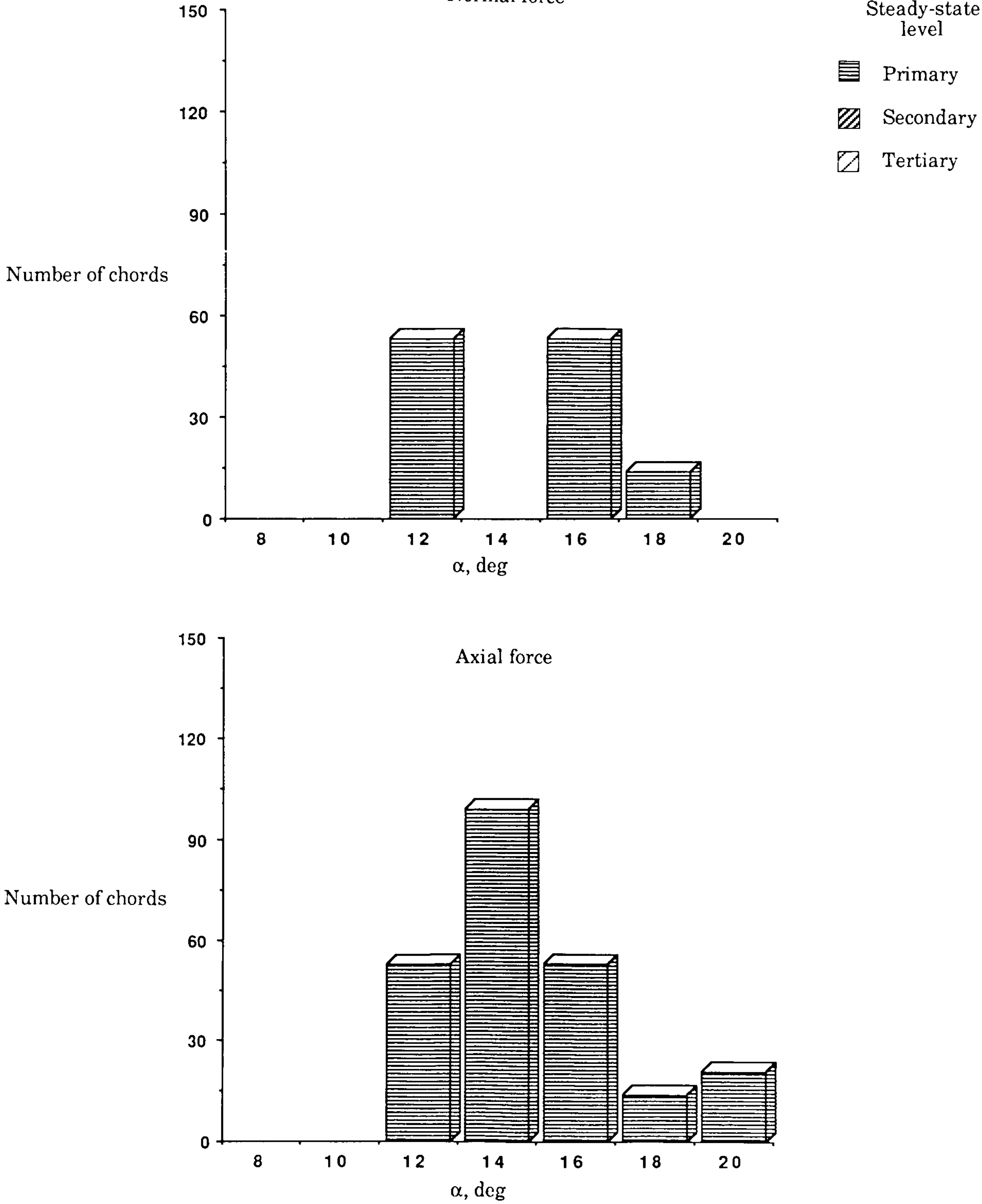

(c) $\delta = 20°$.

Figure 17. Concluded.

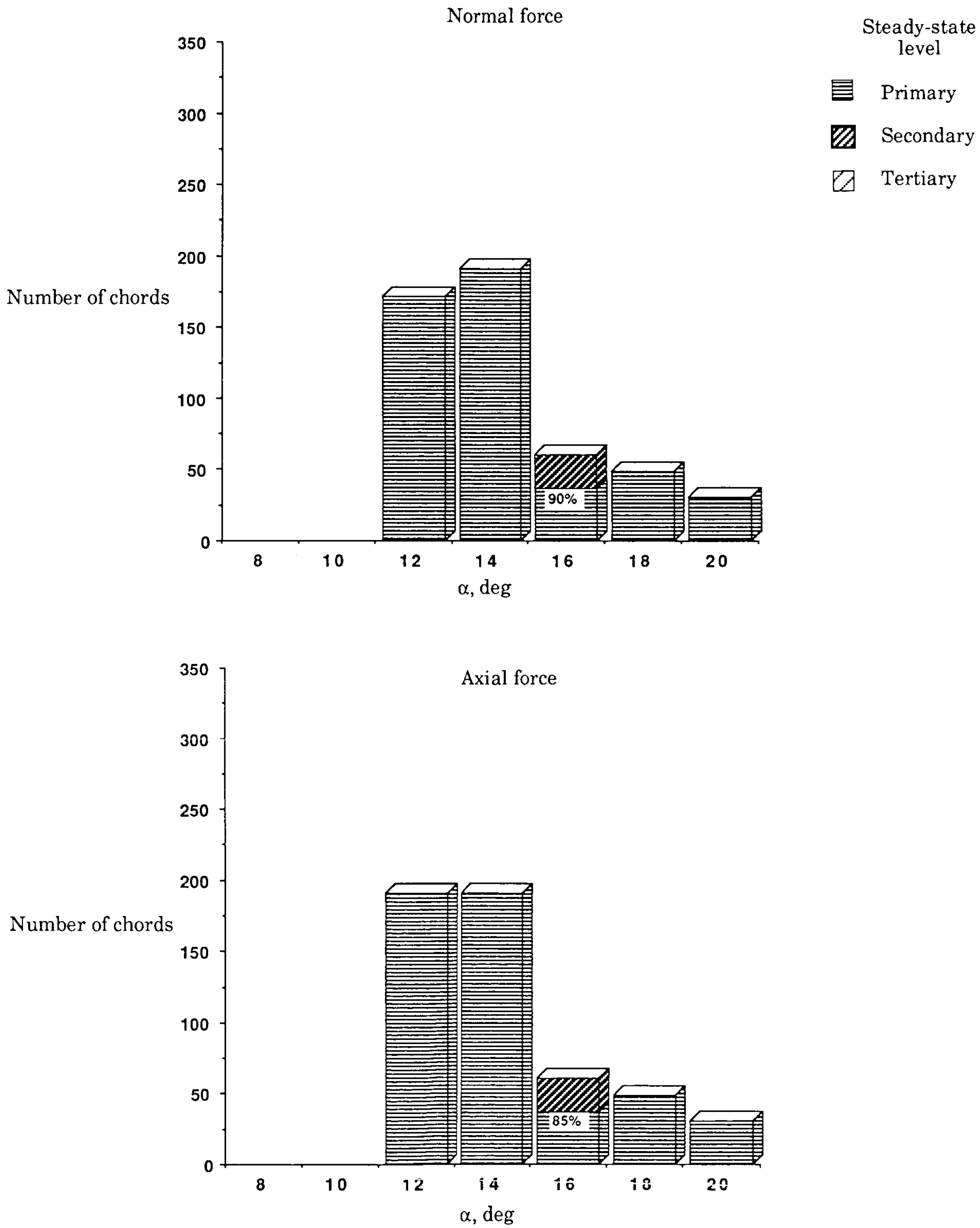

(a) $\delta = 0°$.

Figure 18. Dry to wet transition times for 1570 nozzles, $q = 30$ psf, and LWC = 23 g/m^3.

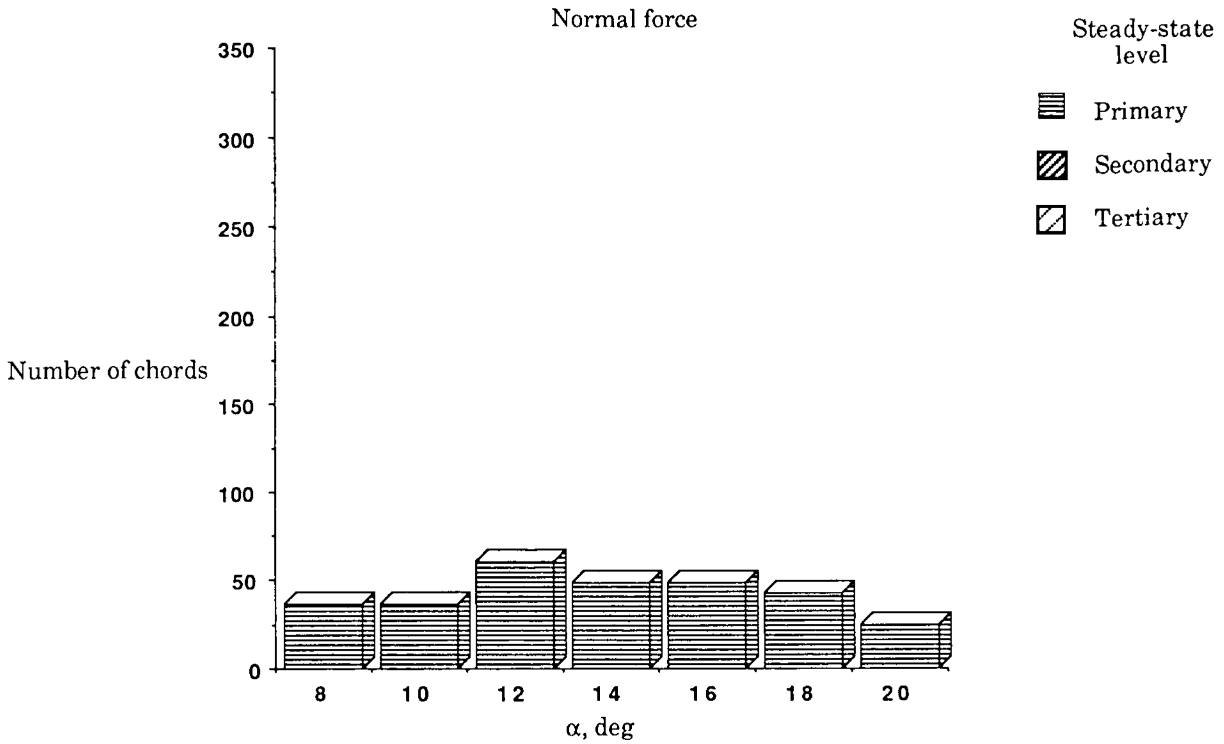

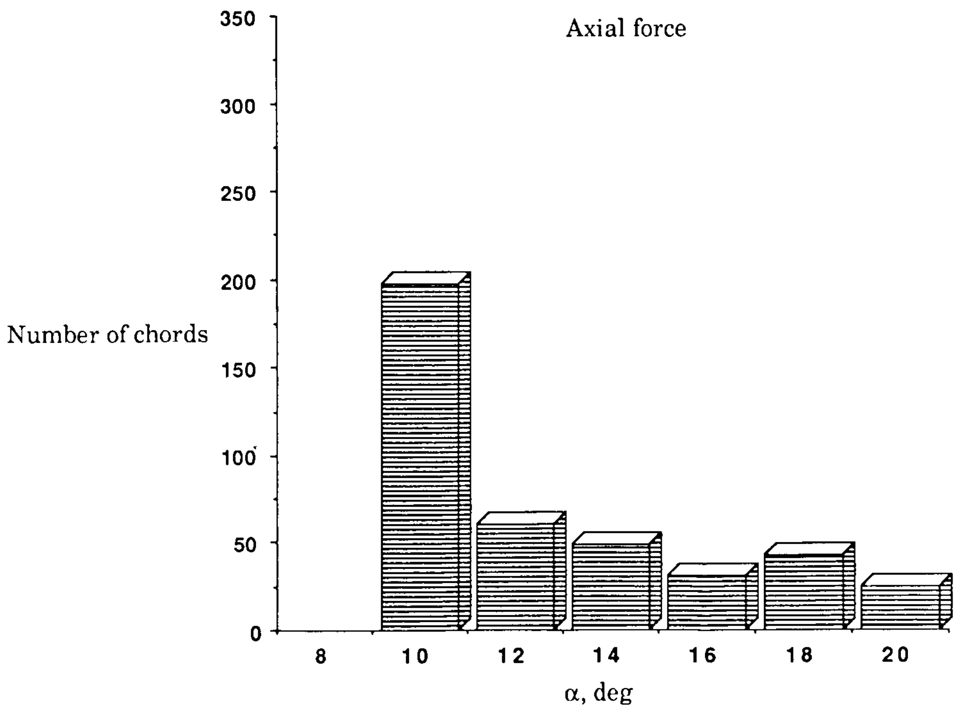

(b) $\delta = 10°$.

Figure 18. Continued.

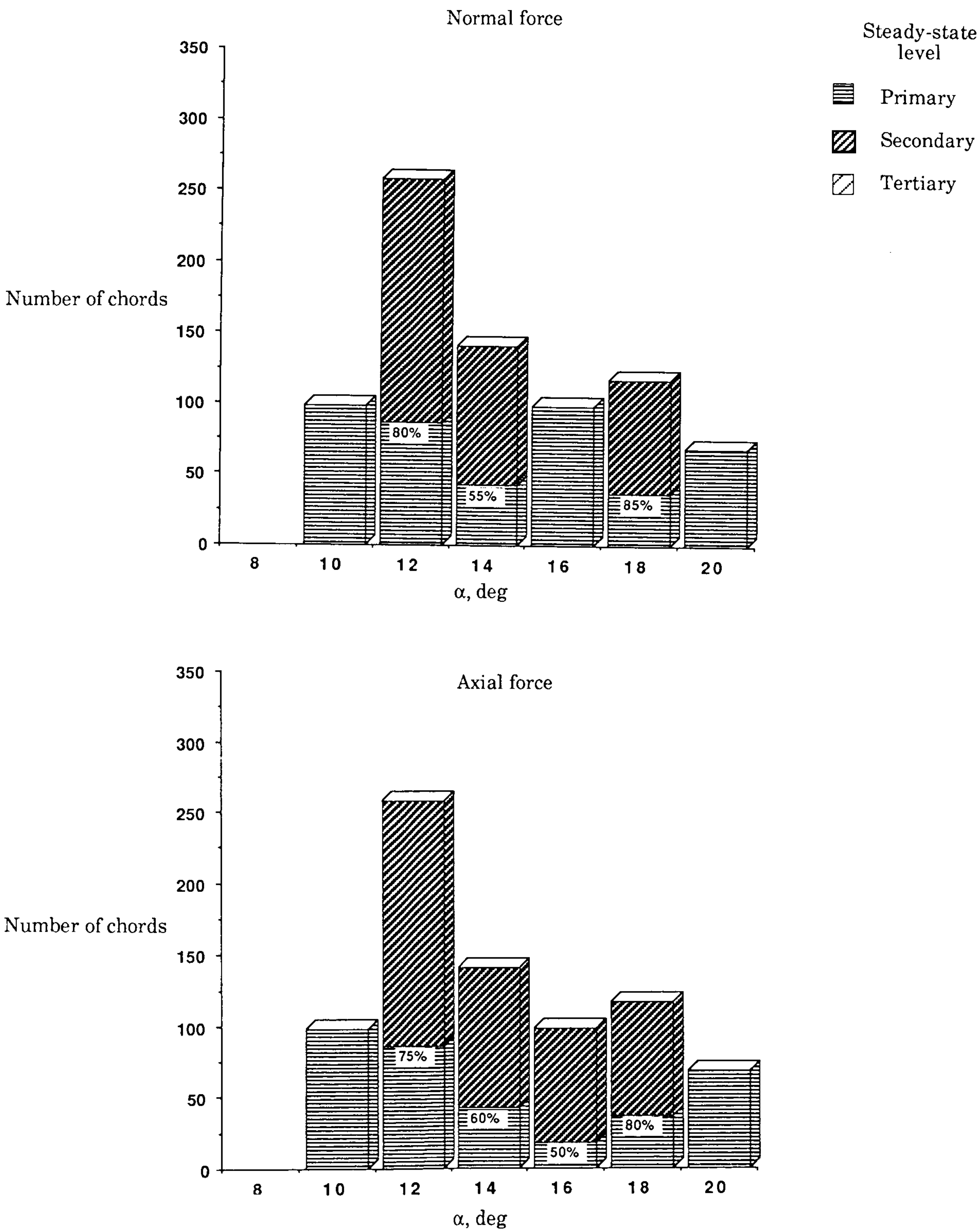

(c) $\delta = 20°$.

Figure 18. Concluded.

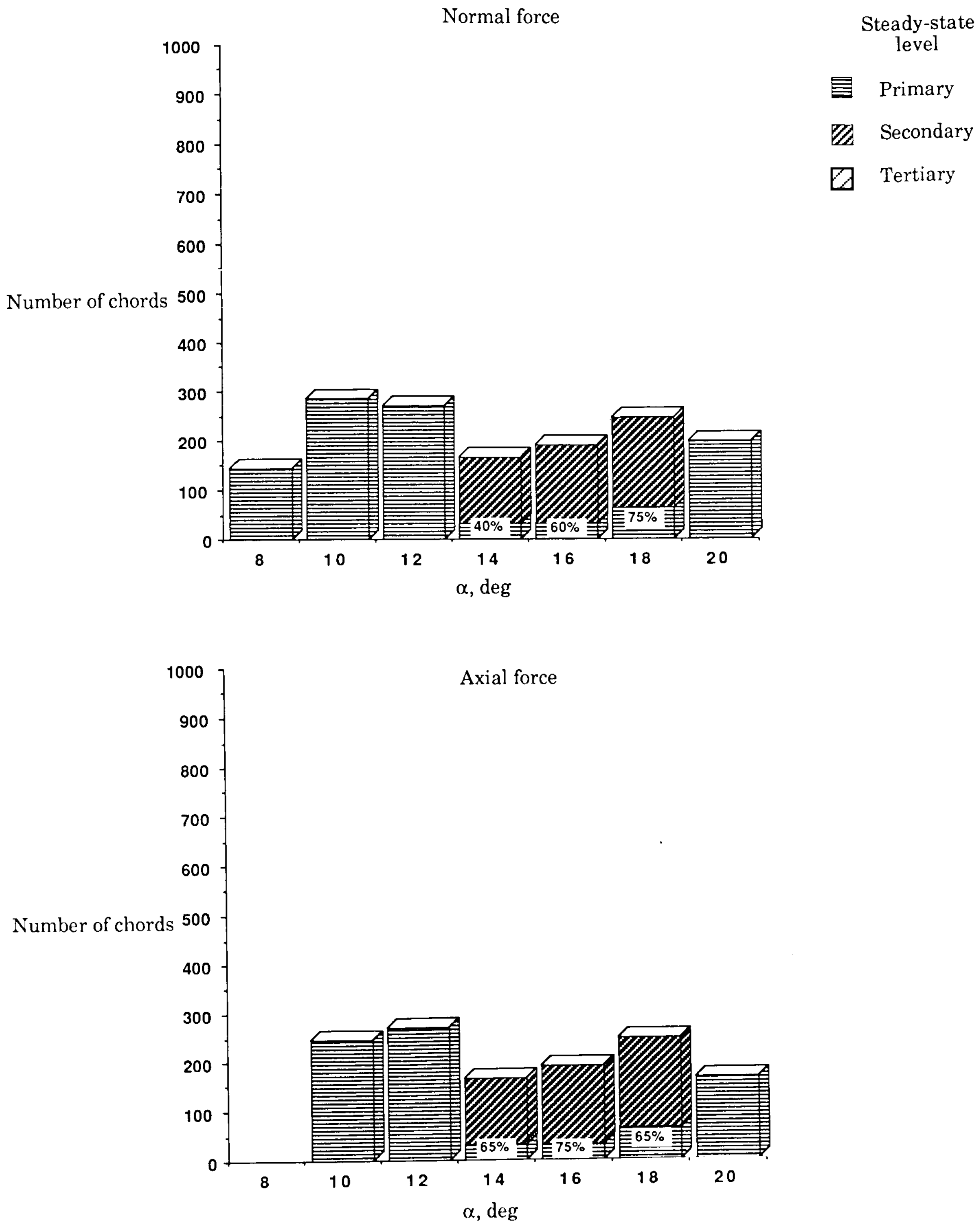

(a) $\delta = 0°$.

Figure 19. Dry to wet transition times for 1570 nozzles, q = 50 psf, and LWC = 22 g/m^3.

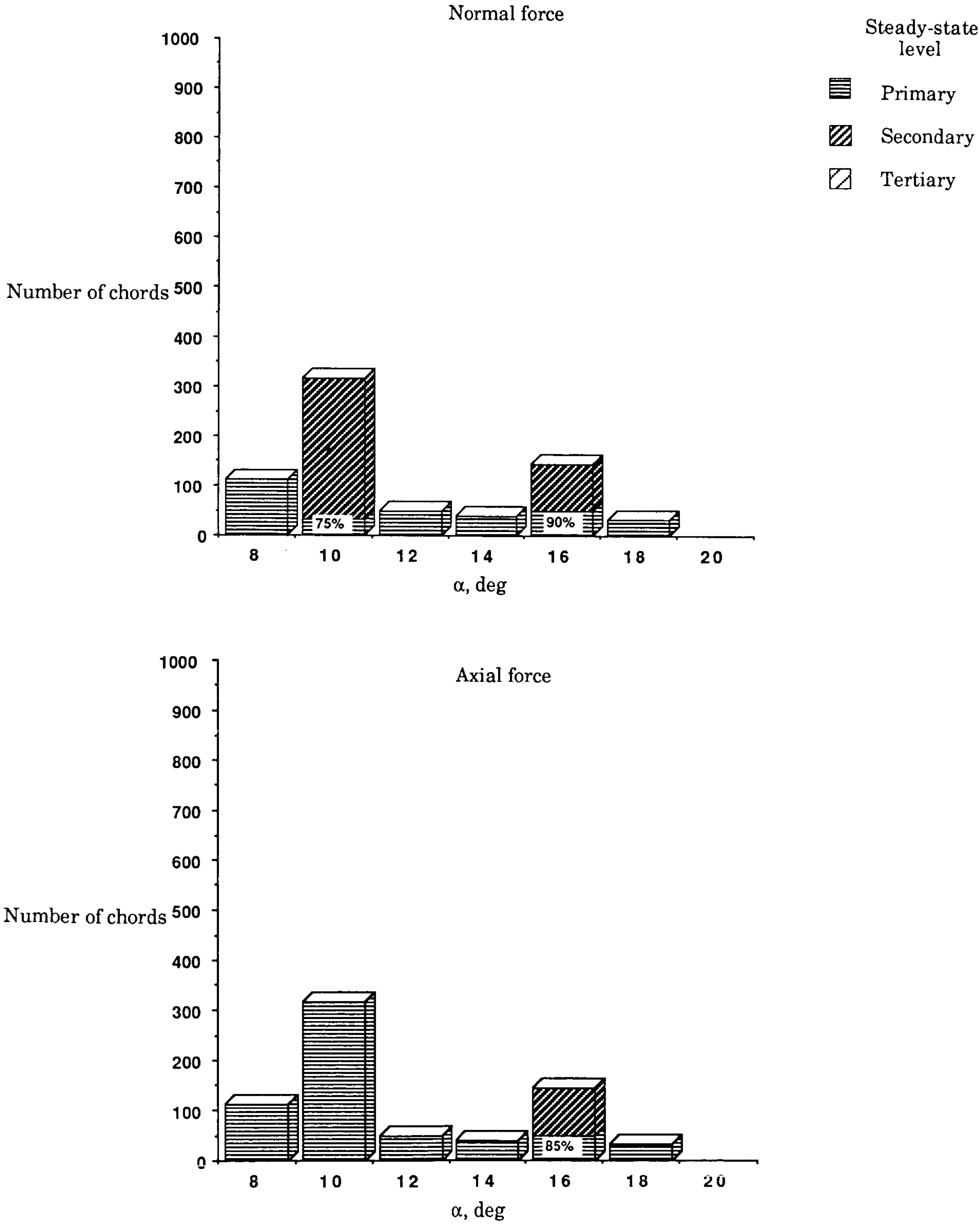

(b) $\delta = 10°$.

Figure 19. Continued.

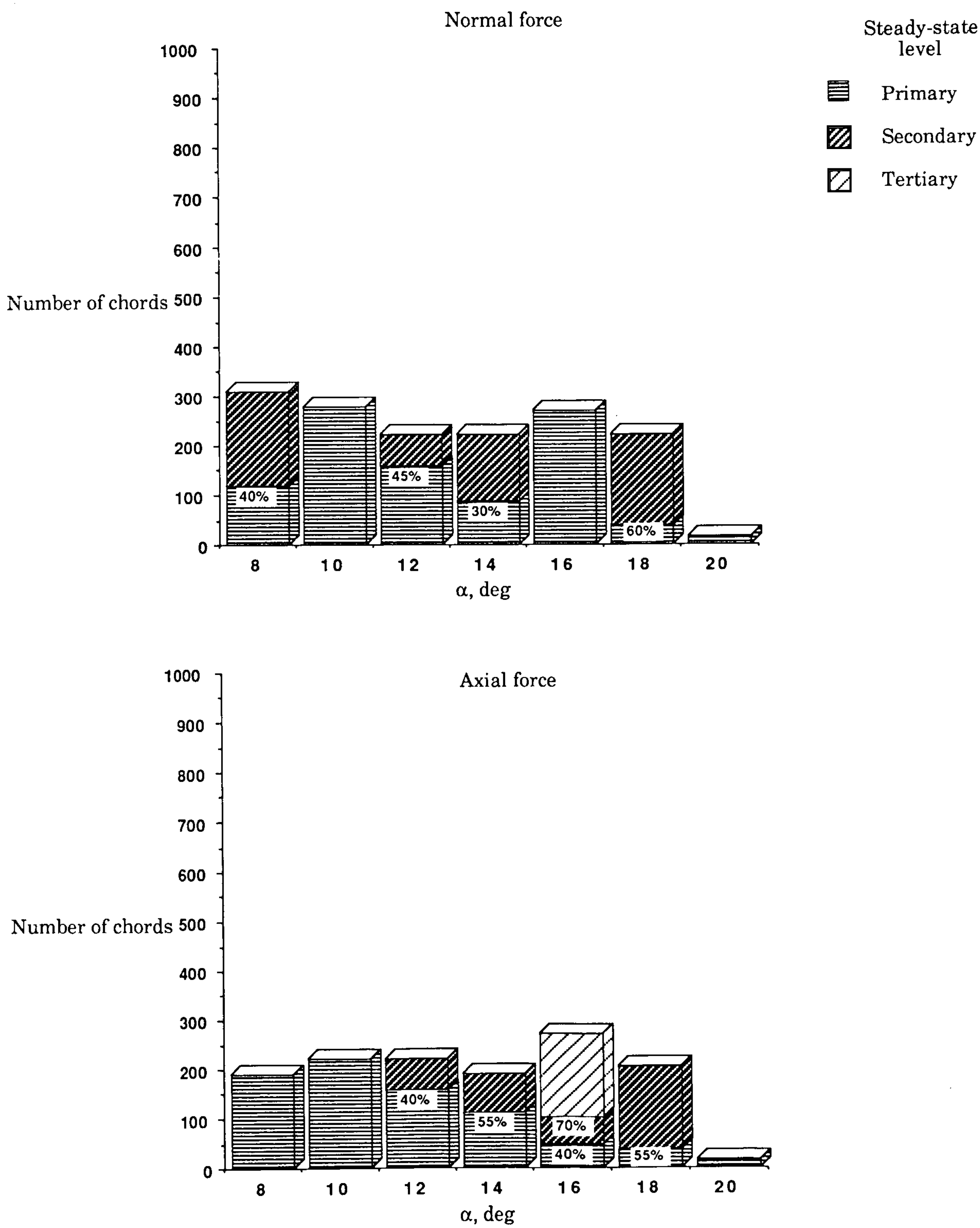

(c) $\delta = 20°$.

Figure 19. Concluded.

NASA
National Aeronautics and Space Administration

Report Documentation Page

1. Report No.	2. Government Accession No.	3. Recipient's Catalog No.
NASA TP-2932		

4. Title and Subtitle	5. Report Date
Steady-State and Transitional Aerodynamic Characteristics of a Wing in Simulated Heavy Rain	August 1989
	6. Performing Organization Code
7. Author(s) Bryan A. Campbell and Gaudy M. Bezos	8. Performing Organization Report No. L-16576
9. Performing Organization Name and Address NASA Langley Research Center Hampton, VA 23665-5225	10. Work Unit No. 505-68-01-02
	11. Contract or Grant No.
12. Sponsoring Agency Name and Address National Aeronautics and Space Administration Washington, DC 20546-0001	13. Type of Report and Period Covered Technical Paper
	14. Sponsoring Agency Code

15. Supplementary Notes

16. Abstract

An investigation was conducted to determine the steady-state and transitional effects of simulated heavy rain on the subsonic aerodynamic characteristics of a wing model in the Langley 14- by 22-Foot Subsonic Tunnel. The wing was comprised of an NACA 23015 airfoil with a chord of 1.29 ft and an aspect ratio of 6.10. Data were obtained while test variables of liquid water content, angle of attack, and trailing-edge flap angle were parametrically varied at dynamic pressures of 10, 30, and 50 psf (i.e., at Reynolds numbers of 0.76×10^6, 1.31×10^6, and 1.69×10^6). The experimental results showed reductions in lift and increases in drag for the wing in the simulated rain environment. Accompanying these reductions was a reduction of the stall angle of attack by approximately 4°. The transient aerodynamic performance during transition from dry to wet steady-state conditions varied between a linear and a nonlinear transition.

17. Key Words (Suggested by Authors(s))	18. Distribution Statement
NACA 23015 Static Heavy rain Liquid water content Dynamic	Unclassified—Unlimited Subject Category 02

19. Security Classif. (of this report)	20. Security Classif. (of this page)	21. No. of Pages	22. Price
Unclassified	Unclassified	93	A05

NASA FORM 1626 OCT 86

NASA-Langley, 1989

For sale by the National Technical Information Service, Springfield, Virginia 22161-2171